Evaluation of the energy-based runoff concept for a subalpine tundra hillslope

by

Qian Che

A thesis

presented to the University of Waterloo

in fulfillment of the

thesis requirement for the degree of

Master of Applied Science

in

Civil Engineering

Waterloo, Ontario, Canada, 2012

Author's Declaration

I hereby declare that I am the sole author of this thesis. This is a true copy of the thesis, including any required final revisions, as accepted by my examiners.

I understand that my thesis may be made electronically available to the public.

Abstract

A major challenge to cold regions hydrology and northern water resources management lies in predicting runoff dynamically in the context of warming-induced changes to the rates and patterns of ground thaw and drainage. Meeting this challenge requires new knowledge of the mechanisms and rates of ground thaw and their implications to water drainage and storage patterns and processes. The study carries out to evaluate the concept of energy-based runoff in the perspective of ground heat flux, soil thaw and liquid moisture content, tortuosity of snow-free area, preferential flow and discharge of the hillslope.

Based on field measurements, coupled energy and water flow is simulated in the Area of Interest (AOI) with a half-hour time interval by the distributed hydrological model, GEOtop. In the field, the saturated hydraulic conductivity varies exponentially between the superficial organic layer and the underlying mineral layer. In the simulation, the parameters of the soil physical properties are input by fourteen uneven layers below the ground surface. Starting from the initially frozen state, the process of soil thaw is simulated with dynamic variables such as soil liquid moisture and ice content, hydraulic conductivity, thermal conductivity and heat capacity. The simulated frost table depths are validated by 44-point measurements and the simulation of point soil temperature is also compared to data measured in an excavated soil pit.

As a result, the frost table topography is dominated by both the snow-free pattern and the energy fluxes on the ground surface. The rate and magnitude of runoff derived from snow drift and the ice content of frozen soil is greatly influenced by the frost table topography. According to the simulation, the frost table depth is closely regressed with the ground surface temperature by a power function. As soil thawing progresses, ground heat flux reduces gradually and the rate of soil thaw becomes small when the frost table descends. Along with the snow-free area expanding, the average soil moisture of the AOI increases prior to that time when the average frost table is less than 25 cm deep.

The snow-free patches expand heterogeneously in the AOI, which causes the spatial and temporal variation of hydraulic conductivity due to the non-uniform frost table depth. According to the simulation, the transit time of the flow through the AOI decreases to the shortest span on May 13 with the average frost table of 10 cm. Before this date, the time lag between snowmelt percolation and slope runoff is about 8-10 hours; while after this date, the time lag is no more than 5 hours. The pattern of the preferential flow in the AOI highly depends on the frost table topography. When the snow-free patches are widely scattered and the average frost table is between 0 and 10 cm, the preferential flow paths are inhibited. With soil thaw progresses, the preferential flow paths are prominent with the largest single contributing area occurring when the average frost table is between 10 cm to 15 cm. When the average frost table reaches 25 cm, the importance of preferential flow is not apparent, and matrix flow prevails.

Acknowledgements

In the whole study period, Dr. Bill Quinton and Dr. Ric Soulis have provided continued generosity and encouragement. I am very grateful for their patient and enlightened supervision to teach me the knowledge and to inspire my academic research, especially when I changed my status from PhD to Master's graduate in 2011, they maintained the same support and attention as previously on my study, which allowed me to complete the program.

I would like to thank Dr. Stefano Endrizzi, who has greatly helped me with GEOtop. He has achieved some additional functions and revised the model to meet the specific requirements for my research. Without his help, the thesis could not be accomplished. He was also kind to introduce me to the related dissertation with GEOtop.

I cherish the valuable experience in the Wolf Creek Research Basin, Whitehorse, Yukon Territory. In the field, I spent a wonderful time with Jessica Butcher, Dr. Cecile Menard and Shawn MacDonald. I also would like to thank Dr. Sean Carey and Dr. Michael Treberg for data support. Also thanks to Dr. Laura Chasmer and Clay Morgan for their help.

During the entire study period when I settled in the hydrology lab, Robin Thorne, Ashok Kumar Verma and Ibrahim Rashid, Tyler Williams and Tyler Veness have provided a comfortable environment.

I appreciate my wife, Mrs. Hui Fang Zhang, who has undertaken a lot for our family. I am sure my son, Jia Rui Che, is glad to see my thesis complete. His happiness in the new culture has relieved my tension much in the final time of writing this thesis.

I would like to thank my parents, Zongfu Che and Xiufang Ma, for their generous love.

Table of Contents

List of Figures

List of Tables

Chapter 1

Introduction

1.1 Research Problem

North-western Canada is one of the most rapidly warming regions on Earth [Johannessen *et al.*, 2004; Serreze, 2000]. There is mounting evidence that this warming is affecting the region's water resources. For example, the frequency of mid-winter melt events has increased, end-of-winter melt occurs earlier, and key hydrological and climatic variables, such as snowpack depth, river discharge, and seasonal precipitation, have deviated from long-term means. These changes have been accompanied by changes to seasonal ground thaw and drainage regimes in organic soils overlying permafrost. This introduces considerable uncertainty about the future availability of northern freshwater resources since the pattern and depth of ground thaw often controls water storage and drainage processes. A major challenge to cold regions hydrology and northern water resources management lies in predicting runoff dynamically in the context of warming-induced changes to the rates and patterns of ground thaw and drainage. Meeting this challenge requires new knowledge of the mechanisms and rates of ground thaw and their implications to water drainage and storage patterns and processes.

Since only a small fraction of permafrost basins in Canada are gauged, understanding the impact of climate warming and human disturbance on the runoff response of permafrost basins requires improved conceptualisation of hydrological processes. The predictive tools currently available to northern water managers are largely based on the variable source area concept [Hewlett, 1967] of runoff generation that assumes runoff to streams is supplied mainly by the overland-flow from topographically-controlled saturated source areas that expand and contract in response to soil moisture variations. However, this concept and the subsequent refinements that describe the associated runoff mechanisms [Beven, 1979; Bishop, 1991; Soulis, 2000; Spence, 2002; Weiler,

2004; Tromp-van Meerveld, 2006] do not explicitly account for permafrost, a feature that profoundly affects catchment hydrological response by confining flow and storage processes to the overlying active layer. They also do not account for the depth-variable transmission properties [Zhang, 2008], large water-holding capacity [Slaughter, 1979; Carey, 2001], and high frozen and unfrozen infiltration rates [Hinzman, 1993] of organic soils that far exceed snowmelt and rainfall input rates and therefore allow little or no runoff over the ground. The effects of the large and spatially-variable end-of-winter snow storage [Church, 1974; Woo, 1986] are also often neglected in the interaction between snow and its frozen substrate. A new unifying concept that explicitly accounts for these factors is needed to form the basis of improved runoff prediction tools for the vast regions of organic-covered permafrost.

1.2 Background

Based on field studies of a wide range of organic-covered permafrost terrains throughout the Canadian Arctic, including taiga, arctic and alpine tundra, and boreal forests and wetlands, a new energy-based runoff (EBR) framework was developed [Quinton, 2008] for delineating the runoff contributing areas in such environments. Since these environments support a similar suite of peat-forming species, there are strong similarities in the hydraulic [Carey, 2007; Quinton, 2008] and thermal [Hayashi, 2007] properties of their organic soils, which promotes the transferability of the new framework. The locations of runoff producing areas have been shown to persist from year to year (2003 to 2009) since the spatial patterns of snow accumulation, snowmelt, and active layer thaw are controlled largely by the spatial variation in aerodynamic and radiant energy. This established local characteristic, in turn, is controlled by surface topography, namely aspect and slope angle. While traditional theories of runoff generation may apply to flat, homogeneous tundra, any degree of topographic variation can introduce substantial variations in radiation and aerodynamic energy, which in turn affects snow accumulation and melt, active layer thaw, soil moisture, evapotranspiration, and, therefore, the volume and timing of runoff.

1.2.1 Hydraulic Properties

The saturated hydraulic conductivity (K_s) profiles of the organic soils overlying permafrost exhibit a uniformly high and low K_s in the upper and lower layers of the peat profile, respectively, separated by a transition zone in which K_s decreases by several orders of magnitude with depth. K_s is a continuous function of depth below the ground surface [Quinton, 2008], and this attribute is incorporated into the Cold Region Hydrologic Model (CRHM), MEC Simulator for Hydrology (MESH), GEOtop and other simulation models. The analysis of high-resolution three dimensional (3D) tomographic images combined with laboratory measurements of hydraulic conductivity on the same peat samples provided important insight into how moisture flow and redistribution processes vary with soil water pressure [Quinton 2009]. The analysis of 3D images also defined values for key thermal and hydraulic properties of peat, including some (e.g. shape factor) hitherto believed to be unmeasurable by direct means [Rezanezhad, 2009].

1.2.2 Thermal Properties

Given the depth-dependency of K_s, the frost-table topography not only defines the spatial pattern of ground thaw, but it also defines the spatial distributions of K_s and hydraulic gradients, and reveals preferential paths and local drainage directions [Quinton, 2008]. The ground thaw depth is strongly correlated with cumulative ground heat flux [Quinton, 2007], and thus the spatial pattern of thaw mirrors the pattern of snowcover removal [Waddington, 2008]. Since organic-covered permafrost terrains support a similar suite of peat-forming species, the hydraulic properties [Dornes, 2008; Wright, 2008] and thermal properties [Hayashi, 2007] of the soils in these terrains are similar, which adds to the transferability of the energy-based concept. The soil thaw rate over hillslopes can be accurately simulated from the areal depletion of the snowcover [Wright, 2008]. By simulating snowmelt and soil thaw spatially on a >25 000 m^2 hillslope at Granger Creek (located in the Wolf Creek Research Basin) using the TONE model, information unobtainable at the point and plot scales, such as the spatial and temporal patterns of flow-zone K_s, tortuosity of flow paths and slope-

integrated drainage rates were obtained [Quinton, 2009]. The transit times of major runoff paths and their seasonal variations were also defined [Wright, 2009].

A simple heat-conduction model was developed [Hayashi, 2007] to simulate the downward movement of the frost table with ground thaw. Simulations were compared with the heat flux measured simultaneously using the calorimetric, gradient, and flux-plate methods. The majority (>86%) of ground heat flux was used to melt the ice in the active layer, and soil temperature was shown to have a linear profile from the ground surface to the frost table when averaged over several days. Assuming a linear temperature profile, this new method calculates the daily rate of thaw from ground surface temperature and bulk thermal conductivity, where the latter is determined by soil water content. Simulated depths to the frost table during three thaw seasons (2003-2005) matched closely with the observed data for two contrasting ground-cover types with distinctly different thaw rates. This method can be easily incorporated into hydrological models. When coupled with a mass flow algorithm, it is a powerful tool for simulating hillslope drainage in organic-covered permafrost terrains and for evaluating the effects of topography and ground cover on the temporal and spatial variability of the frost table depth.

1.2.3 Coupled Thaw and Drainage Processes

The active layer is that portion of the soil above permafrost that thaws and freezes seasonally. The active layer is saturated or nearly saturated with ice and ~15% (volumetric) unfrozen water, at the onset of snowmelt runoff in the spring [Quinton, 2005]. The upper surface of the frozen, saturated soil is impermeable to infiltrating meltwater, and when the ground is thawing, this surface coincides closely with the zero-degree isotherm (*i.e.* frost table) [Quinton, 2009] and represents the lower boundary of the sub-surface flow zone (the thawed portion of the saturated soil that conducts runoff). Since the saturated, horizontal hydraulic conductivity, K_s, decreases by several orders of magnitude with depth [Quinton, 2008; Carey, 2005], the depth of the relatively impermeable frost table is critically important in controlling the rate of subsurface drainage from hillslopes. The accurate

estimation of this flux therefore requires the depth of thaw to be known so that an appropriate value of K_s can be assigned.

1.2.4 Multi-scale Thaw-drainage Response Modelling

At the slope scale, strong correlations have been demonstrated between the cumulative ground heat flux (or indices of the latter, such as cumulative ground surface temperature) and the depth of thaw [Quinton, 2005]. The spatial pattern of thaw therefore mirrors the pattern of snowcover removal as demonstrated in [Quinton, 2009]. This close coupling of soil thaw and drainage at the slope scale has led to a new conceptual understanding of drainage from organic-covered permafrost hillslopes that emphasises the importance of not only the frost table depth but also the frost table topography. Given the depth-dependency of K_s, the frost table topography also defines the K_s and hydraulic gradient spatial distributions. The frost table topography also reveals local subsurface drainage directions and patterns and the locations of preferential paths [Quinton, 2008]. A modification to the fill and spill hypothesis for organic-covered permafrost was proposed [Wright, 2009]. Feedback relationships between thaw and drainage also occur at smaller scales such as along preferential paths. Preferential flow leads to preferential thaw along the drainage channel resulting in a local thaw depression toward which subsurface water drains, producing a local area of elevated soil moisture content and, therefore, increased bulk thermal conductivity of the peat. More thermal energy is transferred downward from the ground surface, further deepening the thaw depression and further drawing local subsurface drainage from surrounding areas.

Simple Fill and Spill Hydrology (SFASH), a quasi-3D coupled heat and water transfer model simulates the feedback between thawing of the active layer and runoff [Wright, 2009]. This is a novel application of the fill-and-spill hypothesis for organic-covered permafrost since, unlike surface water impounded by bedrock, water stored in frost table topographic depressions can be released (i.e. ‘spilled’) due to melt-out of the impounding ground ice without precipitation forcing as the frost table topography evolves with soil thaw. Information unobtainable at the point and plot scales, such as the

spatial and temporal patterns of K_s, tortuosity of flow paths and slope-integrated drainage rates, was obtained using the TONE model. A high-resolution (LiDAR) digital elevation model (DEM) was combined with energy distribution maps to derive the spatial distribution of ground thaw energy. Ongoing research is focussed on modifying the spatially-distributed hydrological model GEOtop to test the proposed Energy-Based Runoff (EBR) framework for predicting slope and basin runoff at Granger Basin (alpine tundra).

1.3 Approach

The overall objective of this research project is to evaluate the energy-based concept of runoff generation for organic-covered permafrost hillslopes and drainage basins. This will be accomplished from complementary field observations, image analysis and numerical modelling.

1.3.1 Complementary Field and Modelling Studies

The snowmelt runoff period involves the overlapping processes of snowmelt and ground thaw that result in the complete removal of snow and complete thaw of the organic soil layer. Three stages of the snowmelt runoff period can be identified in the research basin. In the first stage, the ground is completely covered by snow. The cold content of the accumulated snow is compensated by the net positive energy input as the snow cover ripens and the physical properties of snow pack change, but no meltwater is observed to flow out. The snow pack becomes wetter, and the grain size of the ice crystal enlarges, especially close to the ground. In the second stage, snowmelt percolation fills up the organic layer due to the impermeable nature of frozen mineral soil, forming a perched saturated zone and initiating runoff. The stream flow begins to increase continuously with melting of snow cover. Soil thaw occurs in the snow free patches, but not below the remaining snow. The spatial and temporal variability of soil thaw may influence the water storage and drainage pattern. The peak of the spring freshet takes place weeks before the snow drift is completely melted. In the last stage, when the frost-table descends below the organic layer, the thermal condition of the hillslope

contributes less to the lateral flow. Water storage in the active layer sustains subsurface flow, while simultaneously recharged by snow drift melt water. Stream flow keeps a relatively high level for some time similar to the recession of a flood.

The coupling of heat and water flow complicates hydrological predictions. However, simulation of coupled heat-mass flow processes is necessary to improve the representation, accuracy and application of the hydrological model in cold regions. In different dimensions, the spatial and temporal features of the energy and water flow process are described by reasonable conceptualizations. The meso-scale hydrological models (~100 m) are based on the lumped Hydrological Response Unit (HRU), and therefore water flow is computed in intra- and inter-HRU and the energy flow is computed in intra-HRU. The micro-scale hydrological models (~10 m) are based on a DEM grid, and the energy and water flow process can be computed on both the intra- and inter-grids.

This study is focused on coupled energy and water flow in the seasonally-thawed (i.e. active) layer. The micro-scale hydrological model, GEOtop, will be applied to integrate energy and water simulation using conservation equations. In the model, parameters such as ice and liquid water content, and soil temperature are integrated in the calculation of hydraulic conductivity, thermal conductivity and heat capacity of the soil. As well, thermal algorithms have been developed in the model, including snow free patches followed by preferential thaw and freezing-point depression of the frozen soil. The adequacy of modelling is supported by field observations and aerial photographs which supply the initial conditions and validate the simulation.

1.4 Objectives

The field measurements and numerical Modelling focus on characterizing the spatial patterns of snowmelt, ground thaw and hillslope drainage, and understanding the processes controlling the feedbacks among them. The four objectives of this study are:

- **to evaluate the relative importance of thermal conduction and advection for seasonal ground thaw rates.** Both thermal conduction and advection contribute thaw energy to the active layer, yet their relative importance is not well understood.

- **to investigate how preferential thaw influences factors important to preferential flow.** Specifically the hydraulic conductivity of the thawed, saturated layer that conducts sub-surface runoff, and the depth-integrated soil moisture will be examined.

- **to evaluate the relative importance of the pattern of snow-cover removal and hillslope topography in controlling the location of preferential paths.** Preferential flow refers to paths that conduct a relatively high proportion of water compared to the average flow through the lower-most row of cells within the area of interest (AOI). The preferential flow is delineated based on the frost table topography.

- **to evaluate the influence of ground thaw on slope drainage.** This objective demonstrates variations in subsurface flow rates over the thaw season as the active layer in the AOI develops, and examines the causes.

Chapter 2

Study Site

The study was conducted at Granger Creek (60°32' N, 135°18' W), which is located within the Wolf Creek Research Basin, 15 km south of Whitehorse, Yukon Territory, Canada (Figure 2.1). The study area is within the Cordilleran climate region, and characterized by a large temperature range, low relative humidity and low precipitation. The average annual temperature is approximately -3 °C. The mean annual January and July temperatures at Whitehorse Airport (elevation 706 m a.s.l.) are -17.7°C and +14.1°C. An Arctic inversion develops during the winter months when air temperature increases with elevation. The mean annual precipitation is 267.4 mm, of which 122 mm falls as snow (1971-2000). However, the precipitation at Whitehorse Airport may underestimate basin precipitation by 25% to 35% [Pomeroy and Granger, 1999]. Granger Basin drains an area of approximately 8 km^2 that ranges in elevation from 1310 m to 2250 m (a.s.l.). The main river valley trends west to east at lower elevations, resulting in predominantly north- and south-facing slopes. Permafrost is found under much of the north-facing slopes and at higher elevations, whereas seasonal frost predominates on southerly exposures.

Throughout the basin, the ground surface is composed of a continuous cover of *Sphagnum* moss and various herbs, sedges, grasses, and lichens. Some woody vegetation is present, including willow (*Salix spp.*) shrubs and a few scattered white spruce (*Picea glauca*) trees. The channel and riparian zones are covered by 2 m to 3 m high willow and birch (*Beula nana*) shrubs, which extend up the slopes but decrease in density and height with elevation. In the mid-slope region, the shrubs are 0.5 m to 1 m high and scattered, and along the upper slope, only occasional patches of dwarf (<0.5 m) shrubs occur. A few scattered white spruce trees occur within the basin, which is above the treeline (Treeline is located roughly at 1300 m).

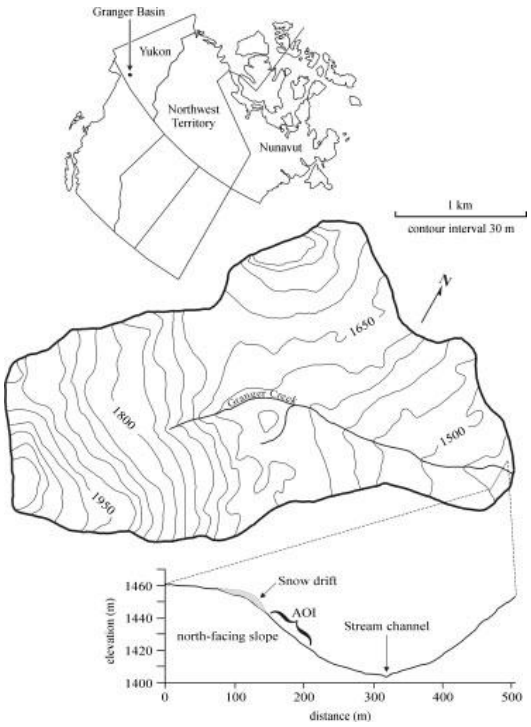

Figure 2.1 Area of Interest (AOI) in Granger basin located downslope of a late-lying snowdrift on the north-facing slope

The north-facing slope near the outlet of Granger Creek (Figure 2.1) is underlain by a 15 m to 20 m thick permafrost layer (Pomeroy and Granger, 1999). The length of the slope from its crest to the stream bank is approximately 150 m. Each year, a deep (>2 m) snow drift forms on the upper part of the slope and persists for 3 to 4 weeks after the disappearance of the surrounding snow cover.

The thickness of the organic soil decreases with distance upslope from ca. 0.4 m in the valley bottom to ca. 0.08 m near the crest. Approximately 31% (by weight) of the underlying mineral sediment is comprised of particles with a diameter of less than 2.00 mm [Quinton *et al.*, 2005]. The soil, described as a sandy loam, is composed of 57.8% sand (<2.00 mm, >0.053 mm), 33.8 silt (<0.053 mm, >0.002 mm), and 8.5% clay (<0.002 mm). The soil representative of the superficial sources is glacial till ranging in depth from 0.8 m to 2.8 m (commonly 2 m) and the depth to bedrock ranges

from 5 m to 30 m (Seguin *et al.* 1998). The average soil densities range from 1440 to 1900 kg/m^3 in dry conditions and 1750 to 2165 kg/m^3 in wet conditions.

Overland flow was not observed anywhere on the hillslope during the study, so hillslope runoff was assumed to be conveyed totally through the active layer. The maximum active layer thickness ranged from ca. 0.4 m at the slope crest to greater than 1 m near the slope base. At the time when the study slope ground surface becomes snow free, the relatively impermeable frost table is typically within 0.05 m of the surface. It then descends through the soil profile as the active layer thaws. The average saturated, horizontal hydraulic conductivity values of the organic soil were measured using tracer tests. These values decreased from ca. 40 m d^{-1} at 0.1 m below the ground surface to ca. 0.85 m d^{-1} at 0.3 m depth [Quinton and Gray, 2003].

Chapter 3

Field Methods

3.1 Field Measurement

3.1.1 Snow Transect Surveys

In each of the 2008 and 2009 melt seasons, the snow water equivalent (SWE) was surveyed from the crest to the foot of the north-facing slope. For forty-eight days from April 19 to June 4, 2008, and thirty-eight days from April 29 to June 4, 2009, the snow depth at five-meter intervals and snow density where the snow depth was less than 1.5 m were measured with a snow scale and tube along three transects A, C and F (Figure 3.1). Transects A, C and F contain 28, 29 and 32 points, respectively.

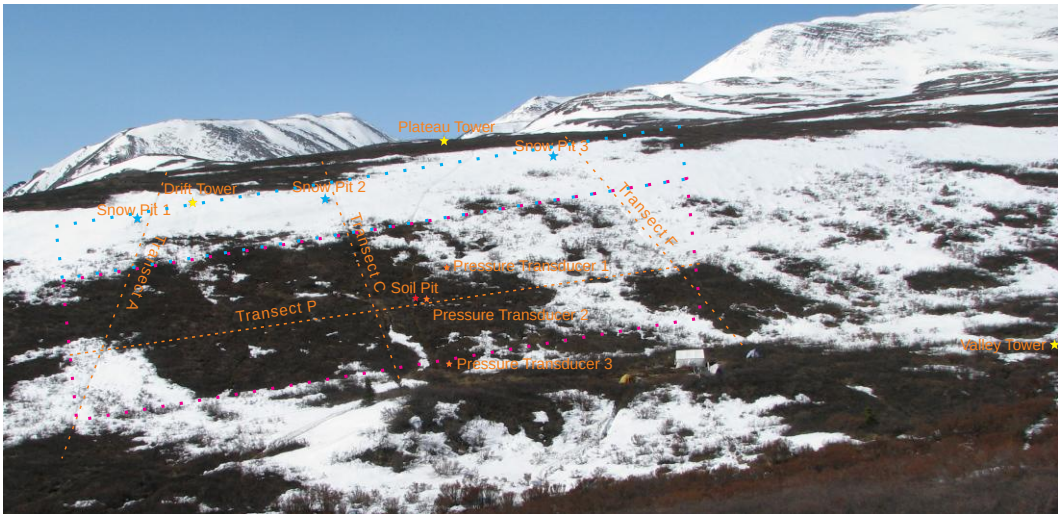

Figure 3.1 Schematic of location of all measurements on north-facing slope

According to the snow transect surveys, a snow drift accumulates on the upper north-facing slope in winter, where the snow depth is between 1 m to 2 m. The snow depth on the top plateau is shallowest, which ranges from 0 cm to 50 cm. The snow cover on the lower north-facing slope is in the range of

50 cm and 1 m. The drift persists for several weeks after the snow cover on the south-facing slope and valley has already disappeared.

When the snow free soil appeared on the measurement point, the frost table (FT) was surveyed instead of the snow depth along the three transects. Additionally, on May 18, 2009, the frost table was measured along a new transect - Transect P, which contains seven points. The ground thaw depth was measured using a graduated steel bar that was inserted through the thawed layer to the depth of refusal. Therefore, the transect surveys embody the information on decreasing SWE and increasing frost table on the measured points.

3.1.2 Snow Pits

Three snow pits were dug in the deepest areas of the snow drift, which are indicated by the blue stars in Figure 3.1. Each day, the depths of the pits were measured, and every three days, the physical properties of each pit − snow grain size, density, temperature, and hardness − were measured manually in several layers along the snow profile. Further in 2009, a snow lysimeter was installed in each of the pits; and the meltwater volumes of the three lysimeters were counted at 15-minute intervals using a tipping bucket and CR200 data logger (Figure 3.2). Additionally, in snow pit #2, time-domain reflectometer (TDR) sensors were inserted laterally at six depths of the snow wall to measure the liquid moisture fluctuation. The program of CR200 data logger for tipping bucket and TDR is provided in Appendix A.

Figure 3.2 lysimeter and tipping bucket in snow pit #1

3.1.3 Photographs

For the duration of the field measurement period, the north-facing slope was photographed daily using a Cannon PowerShot S5 IS camera. The photographs were taken from a fixed position of the south-facing slope at approximately about 10am each day and the camera settings were kept the same for all photographs. The main factors that influenced the quality of the images was atmospheric conditions. In total, 39 useful images were obtained from April 20 to June 4, 2008. Similarly, 35 valid images were acquired from April 27 to June 4, 2009. After georeferencing, the resolution of the photographs corresponded to a pixel size of 0.1 m × 0.1 m.

Using the photographs, the area of interest (AOI) is indicated by the dotted red line in Figure 3.1, which has an area of 10740 m^2 (179 m × 60 m). The snow drift above the AOI is shown by the dotted blue line, which has an area of 6265 m^2 (179 m × 35 m). Snow transects measurements in the snow drift area and the AOI are applied to interpolate the snow cover distribution.

3.1.4 Soil Pit

The soil pit was located approximately in the center of the AOI, which is indicated by the red star in Figure 3.1. At this point on the north-facing slope, the upper 0.15 m was composed of living and

lightly decomposed fibric peat overlying a lower 0.19 m thick layer of sylvic peat containing dark woody material and the remains of mosses, lichens, and rootlets. The lowest 0.06 m was composed of mineral sediment. Volumetric soil moisture sensors (Campbell CS615, accuracy ±3%) were installed in the pit face at 0.02, 0.05, 0.10, 0.20, 0.30 and 0.40 m below ground surface, and soil temperature sensors (Campbell 107B, accuracy ±0.2 °C) were installed in the pit face at 0.02, 0.05, 0.075, 0.10, 0.15, 0.20, 0.25, 0.30, 0.35 and 0.40 m below ground surface. The measurements were made every minute, averaged and recorded on a Campbell Scientific CR10X data logger every half hour.

3.1.5 Water Pressure Transducers

Three water pressure transducers (Global Water WL16) were installed in 2009 beside Transect C to measure the variation of the water table. Their locations are plotted by the yellow stars in Figure 3.1. The water level measurements were recorded every fifteen minutes. Water pressure transducers 1, 2 and 3 measurements were initiated on May 7, April 30, and May 2. The water levels for transducers 1, 2 and 3 varied from -18.9 cm to -6.6 cm (minus represents the distance below ground surface), -9.62 cm to 6.22 cm (plus represents the distance above ground surface) and -6.59 cm to 1.37 cm, respectively.

3.1.6 Meteorological Towers

Meteorological instruments on the valley tower (Figure 3.1) were used to measure the air temperature, relative humidity (at heights of 2.47 m and 3.50 m), wind speed (at heights of 2.79 m and 3.84 m), snow depth (at heights of 0.75 m and 1.74 m), precipitation (on ground), soil temperature (at soil depths of 0.05 m and 0.10 m), soil heat flux (1.5 cm deep in soil), incoming short-wave radiation (at height of 2.22 m), outgoing short-wave radiation (at height of 2.77 m), and net radiation (at height of 2.47 m) at half-hourly intervals.

The meteorological data is important to study the energy and water process on the hillslope and the radiation varies greatly in the different micro-terrains. In the study, the radiation data are applied from

the meteorological tower on the plateau. The plateau tower measured the half-hourly outgoing shortwave radiation, incoming shortwave radiation, outgoing longwave radiation, incoming longwave radiation, wind speed and direction (at heights of 3.05 m and 1.79 m), air temperature, humidity and snow cover depth.

3.2 Analytical Method

3.2.1 Snow Cover Map

Daily variation of snow cover extent in the AOI is clearly indicated by comparisons of consecutive day images. All images were registered with ground control points using known coordinates and the common tie-points following the method of Quinton *et al.* (2009). The control points and tie-points are the apparent features in the photograph that remained in the same position throughout the time period of image acquisition. These points were distributed strategically on only the north-facing slope but not over the foreground or background areas of the images because the scale of the objects could vary drastically (Figure 3.3). For example, a small movement in the camera's field of view (FOV) can significantly shift the position of the mountains from one image to another.

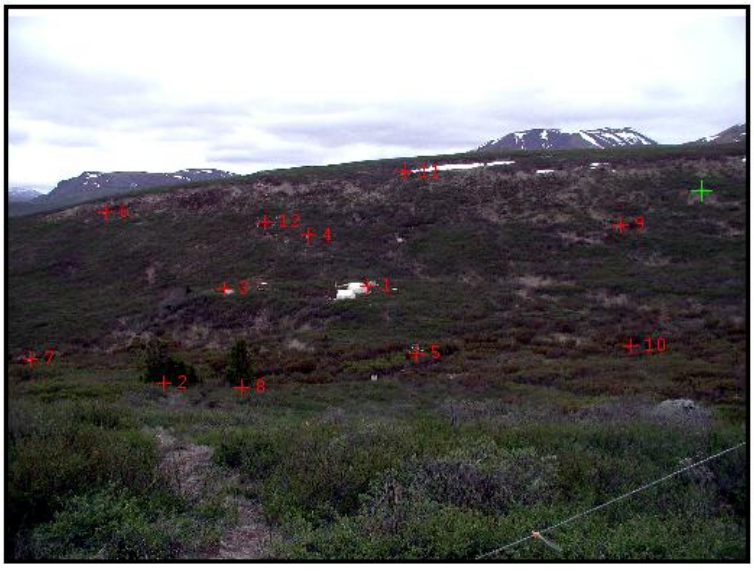

Figure 3.3 Tie-point Collection over the AOI

Snow was differentiated from all other cover using the method in Jenks (1967). This method minimizes each class's average deviation from the class mean but maximizes each class's deviation from the means of the other groups. In other words, the method reduces the variance within classes and maximizes the variance between classes. The procedure of the method is as following:

> "The method requires an iterative process. That is, calculations must be repeated using different breaks in the dataset to determine which set of breaks has the smallest in-class variance. The process is started by dividing the ordered data into groups. Initial group divisions can be arbitrary. There are four steps that must be repeated:

1. Calculate the sum of squared deviations between classes (SDBC).
2. Calculate the sum of squared deviations from the array mean (SDAM).
3. Subtract the SDBC from the SDAM (SDAM-SDBC). This equals the sum of the squared deviations from the class means.
4. After inspecting each of the SDBC, a decision is made to move one unit from the class with the largest SDBC toward the class with the lowest SDBC. "

New class deviations were then calculated, and the process was repeated until the sum of the within class deviations reached a minimal value.

After classification, the snow-cover maps (0.1 m × 0.1 m) are produced. Because the snow-cover map and the digital elevation model (DEM) are both inputs for GEOtop, they must have the equal cell size in the model. Therefore, the cells of the snow-cover maps are merged to 1 m × 1 m. Using the daily snow cover maps, the Julian day when the surface becomes snow free for each 1 m x 1 m cell was determined to tell the model the starting time of soil thaw (Figure 3.4).

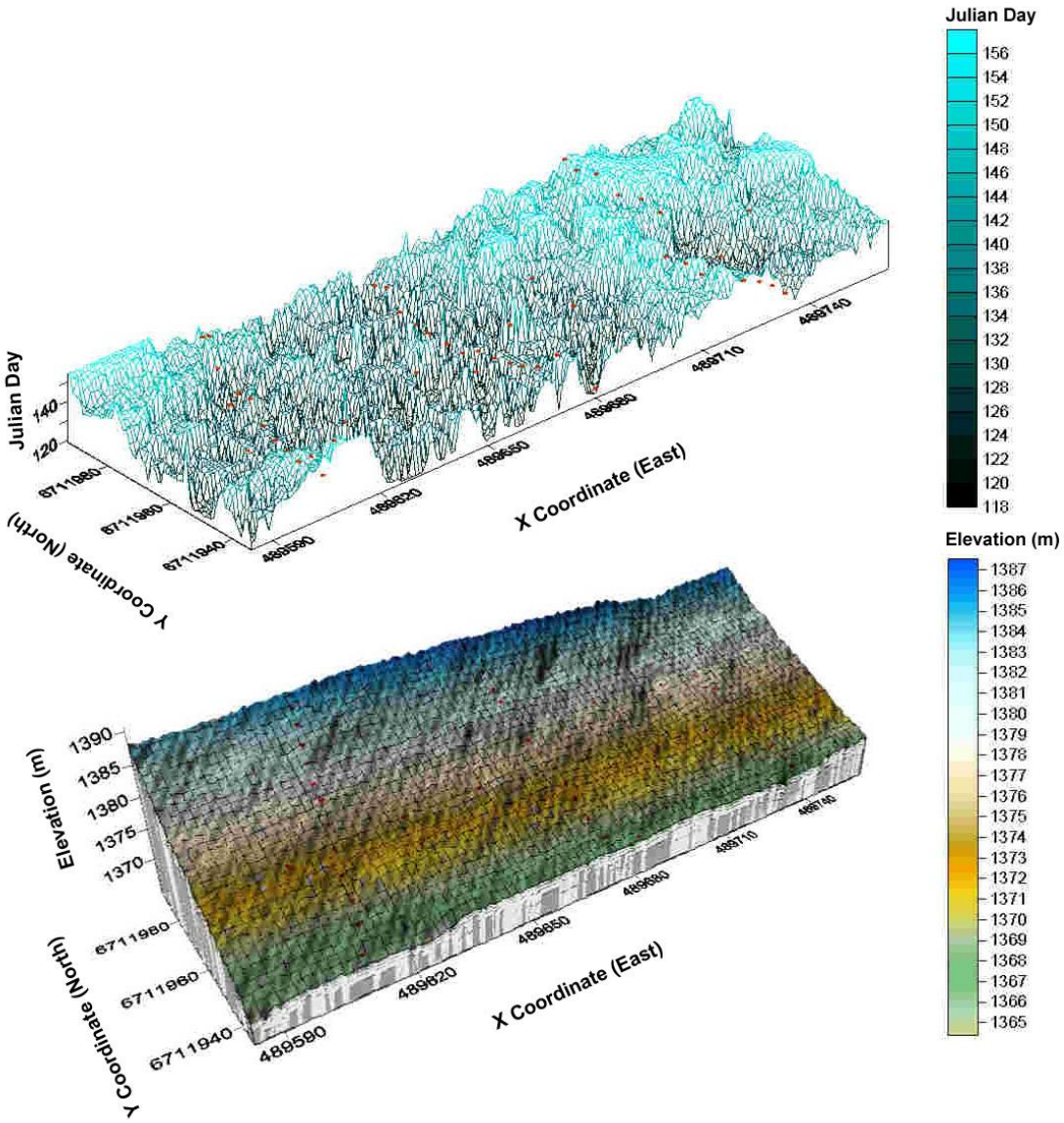

Figure 3.4 A:Julian day of snow free patch and transect survey points; B:DEM of AOI and transect survey points

Using the snow cover maps, the amounts of snow free cells are calculated for each day and consequently a snow- depletion curve is produced (Figure 3.5). According to the curve, the snow-cover area is available for every day. The total snow melt percolation is calculated by the multiplication of the snow-cover area and the unit snow melt percolation. The unit snow melt percolation is derived by the lysimeter measurement. The snow melt percolation flow into the AOI as the lateral flow, which is an input of GEOtop.

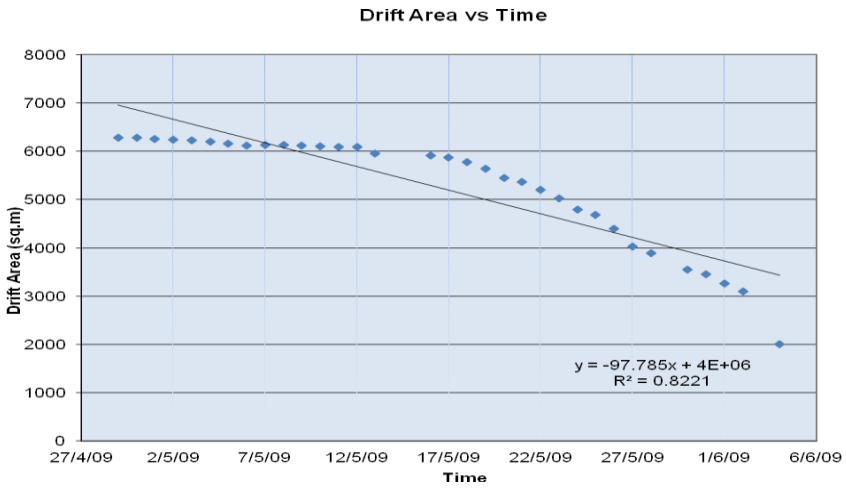

Figure 3.5 Snow depletion curve of the snow drift

3.2.2 Tortuosity Analysis

The preferential flow path can be estimated with the soil thaw map. According to Darcy's law, the rate of flow is equal to the hydraulic conductivity multiplied by the derivative of the water potential. If the soil is frozen, the soil hydraulic conductivity of this cell is significantly lower than that for a thawed cell. Therefore, the water flow can only take place on the thawed cells. The preferential flow path can be estimated by the tortuosity of the snow free patches.

The distance travelled by the particle through its meandering course around snow was quantified through a measure of tortuosity for each time period. The dimensionless tortuosity index, T_x, is calculated using Equation 3.1:

$$T_x = \sum (L_F / L_S) / N \qquad [3.1]$$

where, L_F is the flow length (m), L_s is the length of the straight line between the starting and final cells (m), and N is number of preferential flow paths [Quinton, 1997]. The flow length, L_F, was determined by summing the number of cells encountered during the particle tracking run. As described by Quinton (1997) the particle tracking procedure assumes that all other hill slope features (slope gradient, media properties) are equal.

The particle tracking distance was immediately terminated if the first cell in the run was snow, resulting in an L_F equal to 0. Obstruction to flow was calculated as a ratio between the numbers of terminated runs to the number of successful runs. A value of 0 signifies that flow is completely impeded by snow while a value of 1 indicates that there is no impedance to flow over the entire hill slope from the uppermost row of pixels on the AOI.

Chapter 4

Modelling Methods

GEOtop is a comprehensive, physically-based hydrological model, which solves the energy and water conservation equations on the discretized cells. These cells can directly use the digital elevation model (DEM) of a watershed or catchment. Otherwise, the digital elevation model (DEM) can be merged to the sparse cells when the simulating area is large. The model accommodates complex topography and, besides the water balance, integrates all the terms in the surface energy balance equation [Rigon et al., 2006]. For the individual cell, the water flow through the cell can be divided to one or more components as overland flow, unsaturated and saturated subsurface flow, and channel flow. Due to the recent study in the cold regions hydrology, the distinct modules of snow and frozen soil are developed in GEOtop [Endrizzi *et al.*, 2009; Dall'Amico *et al.*, 2010].

An important feature of the model is that GEOtop applies the numerical computation based on the network of the cells to simulate the hydrological processes. The model is readily accessible to high resolution raster data. Therefore, the spatial characteristics of the energy and water balance can be studied by including the micro-terrain meteorology (e.g. sky view factor, surface temperature) and land surface information (e.g. snow cover). To interpret the model simulation, it is critical to understand the numerical solution of the energy and water equations applied in GEOtop.

4.1 Energy Equation

In GEOtop, the basis is simply known that energy is conserved, which cannot be lost or gained. In the control volume, the variation of internal energy only depends on the heat exchange through the border if there is no source/sink as is supposed. Therefore, if the heat flow into the unit volume (e.g. 1 m × 1 m × 1 m) is taken as positive, then the energy conservation equation can be written as

$$\frac{\partial U(X,t)}{\partial t} - \nabla \cdot u(X,t) = 0 \qquad [4.1]$$

where U is internal energy (J), X is the position, t is time (s), u is the heat exchange through the volume (J m^{-2} s^{-1}).

The internal energy may be considered as the combination of the soil particles U_{sp}, ice U_i and liquid water U_w within the soil void (Equation 4.2):

$$U = U_{sp} + U_i + U_w \quad [4.2]$$

The internal energy of the material is a function of its composition and phase at certain temperature. To treat the internal energy as a simple expression, the soil temperature is expressed in Kelvin. Hence, the internal energy of the soil particle components can easily be determined as follows:

$$\begin{cases} U_{sp} = C_{sp} \cdot \rho_{sp} \cdot (1-\phi) \cdot T \\ U_i = C_i \cdot \rho_i \cdot \theta_i \cdot T \\ U_w = \rho_w \cdot \theta_w \cdot (L_f + C_w \cdot T) \end{cases} \quad [4.3]$$

where C_{sp}, C_i and C_w are the specific heat capacity of soil particles, ice and water (J kg^{-1} K^{-1}), $\emptyset$ the porosity of the soil, T the temperature of the soil (K), ρ_{sp}, ρ_w and ρ_i the densities of soil particles, water and ice (kg m^{-3}), θ_w and θ_i the fraction of water and ice in the control volume, and L_f the latent heat of fusion (J kg^{-1}). Using Equation 4.3, Equation 4.2 becomes:

$$U = C_T \cdot T + \rho_w \cdot L_f \cdot \theta_w \quad [4.4]$$

where

$$C_T = C_{sp} \cdot \rho_{sp} \cdot (1-\phi) + C_i \cdot \rho_i \cdot \theta_i + C_w \cdot \rho_w \cdot \theta_w \quad [4.5]$$

The ice and water content, and temperature in the above expression of the internal energy are the only variables depending on time. The derivative of the internal energy (U) with respect to time is then expressed as follows:

$$\frac{\partial U}{\partial t} = C_T \cdot \frac{\partial T}{\partial t} + \left(C_i \cdot \rho_i \cdot \frac{\partial \theta_i}{\partial t} + C_w \cdot \rho_w \cdot \frac{\partial \theta_w}{\partial t} \right) \cdot T + \rho_w \cdot L_f \cdot \frac{\partial \theta_w}{\partial t} \quad [4.6]$$

In GEOtop, the water flow and water phase change are dealt with separately. During phase change, no water flux is considered in the control unit volume. Then there is an additional equation:

$$\rho_i \cdot \frac{\partial \theta_i}{\partial t} = -\rho_w \cdot \frac{\partial \theta_w}{\partial t} \quad [4.7]$$

which allows simplifying Equation 4.6 as:

$$\frac{\partial U}{\partial t} = C_T \cdot \frac{\partial T}{\partial t} + \rho_w \cdot [(C_w - C_i) \cdot T + L_f] \cdot \frac{\partial \theta_w}{\partial t} \quad [4.8]$$

Through the derivative chain rule, the water content derivative can be written as

$$\frac{\partial \theta_w}{\partial t} = \frac{\partial \theta_w}{\partial \psi} \cdot \frac{\partial \psi}{\partial T} \cdot \frac{\partial T}{\partial t} \quad [4.9]$$

On the right hand side of Equation 4.9, the first derivative is the slope of the soil water retention curve. The second is the slope of the Clausius-Clapeyron equation.

Substituting Equation 4.9 into Equation 4.8, one obtains

$$\frac{\partial U}{\partial t} = \left\{ C_T + \rho_w \cdot [(C_w - C_i) \cdot T + L_f] \cdot \frac{\partial \theta_w}{\partial \psi} \cdot \frac{\partial \psi}{\partial T} \right\} \cdot \frac{\partial T}{\partial t} = C_a \cdot \frac{\partial T}{\partial t} \quad [4.10]$$

where C_a (J m^{-3} K^{-1}) is the so-called apparent heat capacity [Williams and Smith, 1989]. By Equation 4.10, the internal energy variation with time is determined by multiplying the apparent heat capacity by the derivative of temperature.

The value of apparent heat capacity may be interpreted as the quantity of heat required to raise the temperature of a unit volume of soil by 1 K while a phase change between liquid water and ice is occurring. Generally, the heat capacity applies to materials when the pressure is constant. Fortunately, the pressure range in the atmosphere is small enough that the effect of the pressure on soil heat capacity does not matter. For the thermal calculation, the air is considered to be incompressible and the atmospheric pressure is considered to be 101.325 kPa.

For the energy exchange through the volume of soil, the second quantity in the conservation equation (Equation 4.1), takes place mainly as heat conduction and convection. If the control volume is at the ground surface, the energy fluxes include total radiation, sensible and latent heat transfer, and ground

heat flux. The ground surface is treated as the top boundary condition of the model. By contrast, in the subsurface, the energy exchange through the volume is assumed to be the combination of the conducted heat by the temperature gradient, G, and convective heat by water flow, J.

$$u(X,t) = G(X,t) + J(X,t) \quad [4.11]$$

where u(X,t) the total heat exchange (J m^{-2} s^{-1}), G(X,t) is the conducted heat (J m^{-2} s^{-1}), J(X,t) is the convective heat (J m^{-2} s^{-1}). According to Fourier law, the heat conduction can be written as Equation 4.12:

$$G = -\lambda \cdot \frac{\partial T}{\partial X} \quad [4.12]$$

where λ is the thermal conductivity (W m^{-1} K^{-1}). The heat convection can be defined as follows:

$$J = \rho_w \cdot q \cdot (C_w \cdot T + L_f) \quad [4.13]$$

where q (m s^{-1}) is the water flux across the control volume, C_w the specific heat capacity of soil particles (J kg^{-1} K^{-1}), ρ_w the density of water (kg m^{-3}), L_f the latent heat of fusion (J kg^{-1}), and T the temperature of water (K).

Then the energy conservation equation becomes:

$$C_a \cdot \frac{\partial T}{\partial t} - \nabla \cdot (-\lambda \cdot \nabla T + \rho_w \cdot q \cdot (C_w \cdot T + L_f)) = 0 \quad [4.14]$$

By Equation 4.14, the energy equation is solved taking into account the heat conduction and convection. The heat convection depends on both water flow and temperature. The water flow is deduced using the water balance equation. In the computation, the energy and water balance equations are solved separately. In each time loop, the energy balance is computed in the first half time, and water equation is solved in the second half.

4.2 Water Equation

With the same control volume used for the energy equation, the water balance equation can also be set up according to the conservation law. The time variation of total water content in the volume is equal to the water flow through the interfaces (e.g. 6 × 1 m × 1 m) of the unit volume. The water flow into the volume is taken as positive, and the equation is as below:

$$\frac{\partial \Theta(X,t)}{\partial t} - \nabla \cdot q(X,t) = 0 \qquad [4.15]$$

where Θ is the total water content of the unit volume (dimensionless), X is the position, t is time (s), and q is the water flow through the volume (m s^{-1}).

The total water content is the sum of the liquid θ_w and solid θ_i water content with their respective densities.

$$\Theta := \theta_w + \frac{\rho_i}{\rho_w} \cdot \theta_i \qquad [4.16]$$

The derivative of the total water content is:

$$\frac{\partial \Theta}{\partial t} = \frac{\partial \theta_w}{\partial t} + \frac{\rho_i}{\rho_w} \cdot \frac{\partial \theta_i}{\partial t} \qquad [4.17]$$

To simplify Equation 4.17, it is assumed that two processes (phase change and water flow) are separated in time, i.e. in the first dt/2, only phase change takes place, and in the second dt/2, only water flow occurs. During the second dt/2, $\partial\theta_i/\partial t=0$, and therefore Equation 4.17 becomes:

$$\frac{\partial \Theta}{\partial t} = \frac{\partial \theta_w}{\partial t} \qquad [4.18]$$

Since the water content is supposed to have a biunique relation with the water pressure head ψ (m), the water retention curve, Equation 4.18 can be written by applying the derivative chain rule

$$\frac{\partial \theta_w}{\partial t} = \frac{\partial \theta_w}{\partial \psi} \cdot \frac{\partial \psi}{\partial t} = C_h \cdot \frac{\partial \psi}{\partial t} \quad [4.19]$$

where C_h (m^{-1}) is the specific moisture capacity function.

The second item of Equation 4.15, water flow through the volume q, can be calculated according to Darcy's law:

$$q = K_s \cdot K_r \cdot \nabla(\psi + Z) = K_s \cdot K_r \cdot \frac{\partial(\psi + Z)}{\partial X} \quad [4.20]$$

where K_s is the saturated hydraulic conductivity ($m\ s^{-1}$), K_r is the relative conductivity, ψ is the water pressure head (m) and Z is the elevation head over a reference (m). Consequently, substituting Equations 4.18, 4.19 and 4.20 into Equation 4.15, the water conservation equation becomes as below:

$$\frac{\partial \theta_w}{\partial t} - \nabla \cdot (K_s \cdot K_r \cdot \nabla(\psi + Z)) = 0 \quad [4.21]$$

Or

$$C_h \cdot \frac{\partial \psi}{\partial t} - \nabla \cdot (K_s \cdot K_r \cdot \nabla(\psi + Z)) = 0 \quad [4.22]$$

The Equations 4.21 and 4.22 are the mixed variables (ψ and θ) form, and single variable (ψ) form of the water conservation equation, respectively. Further, according to Celia (1990), the numerical solution of the mixed form has the better performance in convergence.

4.3 Discretization

Actually, both energy and water conservation equations, Equations 4.1 and 4.15 can be expressed as the common partial differential equation, which is the diffusion equation as follows:

$$\frac{\partial \xi}{\partial t} - \nabla \cdot \gamma = 0 \quad [4.23]$$

Within Equation 4.23, the second item can be divided as follow:

$$\gamma = f + u = -k \cdot \nabla \eta + u \quad [4.24]$$

Generally, the variables ξ, k and u are the functions of η and spatial position, thus they can be written in following the mathematical formalism:

$$\xi = \xi(\eta, X) \quad [4.25]$$

$$k = k(\eta, X) \quad [4.26]$$

$$u = u(\eta, X) \quad [4.27]$$

The comparison between the energy and water conservation equations can be easily outlined in Table 4.1.

Table 4.1 Comparison of the heat and mass conservation equations as nonlinear diffusion equations

	Heat	Mass
η	T [K]	ψ [m]
ξ	$U = C_T \cdot T + \rho_w \cdot L_f \cdot \theta_w$ [J]	$\Theta := \theta_w + \frac{\rho_i}{\rho_w} \cdot \theta_i$ [-]
f	$-\lambda \cdot \frac{\partial T}{\partial X}$ $[\frac{W}{m^2}]$	$K_s \cdot K_r \cdot \frac{\partial \psi}{\partial X}$ $[\frac{m}{s}]$
u	$\rho_w \cdot q \cdot (C_w \cdot T + L_f)$ $[\frac{W}{m^2}]$	$K_s \cdot K_r \cdot \frac{\partial Z}{\partial X}$ $[\frac{m}{s}]$
γ	$f + u = -\lambda \cdot \frac{\partial T}{\partial X} + \rho_w \cdot q \cdot (C_w \cdot T + L_f)$ $[\frac{W}{m^2}]$	$f + u = K_s \cdot K_r \cdot \left(\frac{\partial \psi}{\partial X} + \frac{\partial Z}{\partial X} \right) [\frac{m}{s}]$
$\frac{\partial \xi}{\partial \eta}$	C_a $[\frac{J}{m^3 \cdot K}]$	C_h $[\frac{1}{m}]$

To simplify the numerical solution of the diffusion equation, the following discrete description is specified for the mixed form of water conservation equation. For instance, the cell (i,j,k) as indicated in Figure 4.1, the Equation 4.21 is discretized as follows:

$$\frac{\partial \xi_{i,j,k}}{\partial t}+\frac{q_{i+\frac{1}{2},j,k}-q_{i-\frac{1}{2},j,k}}{\Delta x_i}+\frac{q_{i,j+\frac{1}{2},k}-q_{i,j-\frac{1}{2},k}}{\Delta y_j}+\frac{q_{i,j,k+\frac{1}{2}}-q_{i,j,k-\frac{1}{2}}}{\Delta z_k}=0 \quad [4.28]$$

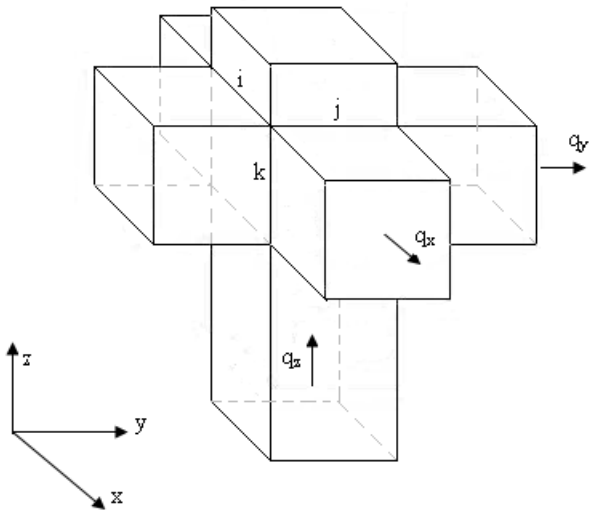

Figure 4.1 Schematic map of cell (i,j,k)

Where $q_{i+\frac{1}{2},j,k}$, $q_{i-\frac{1}{2},j,k}$, $q_{i,j+\frac{1}{2},k}$, $q_{i,j-\frac{1}{2},k}$, $q_{i,j,k+\frac{1}{2}}$, and $q_{i+\frac{1}{2},j,k-\frac{1}{2}}$ are the fluxes through the interfaces between the i-th and i+1-th cells, between i-1-th and i-th cells, between j-th and j+1-th cells, between j-1-th and j-th cells, between k-th and k+1-th cells, and between k-1-th and k-th cells, respectively. The expression $\xi_{i,j,k}$ is the averaged total water content of the cell (i,j,k). The fluxes are calculated as:

$$q_{i+\frac{1}{2},j,k}=-k_{i+\frac{1}{2},j,k}\cdot\frac{\eta_{i+1,j,k}-\eta_{i,j,k}}{x_{i+1}-x_i} \quad [4.29]$$

$$q_{i-\frac{1}{2},j,k}=-k_{i-\frac{1}{2},j,k}\cdot\frac{\eta_{i,j,k}-\eta_{i-1,j,k}}{x_i-x_{i-1}} \quad [4.30]$$

$$q_{i,j+\frac{1}{2},k}=-k_{i,j+\frac{1}{2},k}\cdot\frac{\eta_{i,j+1,k}-\eta_{i,j,k}}{y_{j+1}-y_j} \quad [4.31]$$

$$q_{i,j-\frac{1}{2},k} = -k_{i,j-\frac{1}{2},k} \cdot \frac{\eta_{i,j,k} - \eta_{i,j-1,k}}{y_j - y_{j-1}} \quad [4.32]$$

$$q_{i,j,k+\frac{1}{2}} = -k_{i,j,k+\frac{1}{2}} \cdot \frac{\eta_{i,j,k+1} - \eta_{i,j,k}}{z_{k+1} - z_k} + u_{k+\frac{1}{2}} \quad [4.33]$$

$$q_{i,j,k-\frac{1}{2}} = -k_{i,j,k-\frac{1}{2}} \cdot \frac{\eta_{i,j,k} - \eta_{i,j,k-1}}{z_k - z_{k-1}} + u_{k-\frac{1}{2}} \quad [4.34]$$

The hydraulic conductivities $k_{i+\frac{1}{2},j,k}$, $k_{i-\frac{1}{2},j,k}$, $k_{i,j+\frac{1}{2},k}$, $k_{i,j-\frac{1}{2},k}$, $k_{i,j,k+\frac{1}{2}}$, $k_{i,j,k-\frac{1}{2}}$ are estimated with a suitable mean (arithmetic, geometric or harmonic) between the values of k at the nodes i+1 and i, i-1 and i, j+1 and j, j-1 and j, k+1 and k, and k-1 and k. The water pressure head, η, is estimated at the center of the cell. Integrate Equation 4.28 as follows:

$$\frac{1}{\Delta t} \cdot \int_{t_n}^{t_{n+1}} \frac{\partial \xi_{i,j,k}}{\partial t} \cdot dt + \frac{1}{\Delta t} \cdot \int_{t_n}^{t_{n+1}} \left(\frac{q_{i+\frac{1}{2},j,k} - q_{i-\frac{1}{2},j,k}}{\Delta x_i} + \frac{q_{i,j+\frac{1}{2},k} - q_{i,j-\frac{1}{2},k}}{\Delta y_j} + \frac{q_{i,j,k+\frac{1}{2}} - q_{i,j,k-\frac{1}{2}}}{\Delta z_k} \right) \cdot dt = 0 \quad [4.35]$$

where the items can be calculated as:

$$\frac{1}{\Delta t} \cdot \int_{t_n}^{t_{n+1}} q_{i+\frac{1}{2},j,k} \cdot dt = q_{i+\frac{1}{2},j,k}^{n+\frac{1}{2}} \approx (1-\omega) \cdot q_{i+\frac{1}{2},j,k}^{n} + \omega \cdot q_{i+\frac{1}{2},j,k}^{n+1} \quad [4.36]$$

$$\frac{1}{\Delta t} \cdot \int_{t_n}^{t_{n+1}} q_{i-\frac{1}{2},j,k} \cdot dt = q_{i-\frac{1}{2},j,k}^{n+\frac{1}{2}} \approx (1-\omega) \cdot q_{i-\frac{1}{2},j,k}^{n} + \omega \cdot q_{i-\frac{1}{2},j,k}^{n+1} \quad [4.37]$$

$$\frac{1}{\Delta t} \cdot \int_{t_n}^{t_{n+1}} q_{i,j+\frac{1}{2},k} \cdot dt = q_{i,j+\frac{1}{2},k}^{n+\frac{1}{2}} \approx (1-\omega) \cdot q_{i,j+\frac{1}{2},k}^{n} + \omega \cdot q_{i,j+\frac{1}{2},k}^{n+1} \quad [4.38]$$

$$\frac{1}{\Delta t} \cdot \int_{t_n}^{t_{n+1}} q_{i-\frac{1}{2},j,k} \cdot dt = q_{i,j-\frac{1}{2},k}^{n+\frac{1}{2}} \approx (1-\omega) \cdot q_{i,j-\frac{1}{2},k}^{n} + \omega \cdot q_{i,j-\frac{1}{2},k}^{n+1} \quad [4.39]$$

$$\frac{1}{\Delta t}\cdot\int_{t_n}^{t_{n+1}} q_{i,j,k+\frac{1}{2}}\cdot dt = q_{i,j,k+\frac{1}{2}}^{n+\frac{1}{2}} \approx (1-\omega)\cdot q_{i,j,k+\frac{1}{2}}^{n} + \omega\cdot q_{i,j,k+\frac{1}{2}}^{n+1} \qquad [4.40]$$

$$\frac{1}{\Delta t}\cdot\int_{t_n}^{t_{n+1}} q_{i,j,k-\frac{1}{2}}\cdot dt = q_{i,j,k-\frac{1}{2}}^{n+\frac{1}{2}} \approx (1-\omega)\cdot q_{i,j,k-\frac{1}{2}}^{n} + \omega\cdot q_{i,j,k-\frac{1}{2}}^{n+1} \qquad [4.41]$$

Where $q_{i+\frac{1}{2},j,k}^{n+\frac{1}{2}}$, $q_{i-\frac{1}{2},j,k}^{n+\frac{1}{2}}$, $q_{i,j+\frac{1}{2},k}^{n+\frac{1}{2}}$, $q_{i,j-\frac{1}{2},k}^{n+\frac{1}{2}}$, $q_{i,j,k+\frac{1}{2}}^{n+\frac{1}{2}}$, and $q_{i,j,k-\frac{1}{2}}^{n+\frac{1}{2}}$ are the averaged fluxes in the time interval Δt, $q_{i+\frac{1}{2},j,k}^{n}$, $q_{i-\frac{1}{2},j,k}^{n}$, $q_{i,j+\frac{1}{2},k}^{n}$, $q_{i,j-\frac{1}{2},k}^{n}$, $q_{i,j,k+\frac{1}{2}}^{n}$, and $q_{i,j,k-\frac{1}{2}}^{n}$ are the instantaneous values of the fluxes at the instant t^n, $q_{i+\frac{1}{2},j,k}^{n+1}$, $q_{i-\frac{1}{2},j,k}^{n+1}$, $q_{i,j+\frac{1}{2},k}^{n+1}$, $q_{i,j-\frac{1}{2},k}^{n+1}$, $q_{i,j,k+\frac{1}{2}}^{n+1}$, and $q_{i,j,k-\frac{1}{2}}^{n+1}$ are the fluxes at the instant t^{n+1}. The parameter ω ranges between 0 and 1 and is defined in function of the numerical scheme (ω =0, Euler-explicit Method, ω =0.5 Crank-Nichoson Method, ω =1 Euler-implicit Method). Plug Equations 4.36 to 4.41 into Equation 4.35. Then Equation 4.42 is derived:

$$\frac{\xi_{i,j,k}^{n+1}-\xi_{i,j,k}^{n}}{\Delta t} = \left(-\omega\cdot\frac{q_{i+\frac{1}{2},j,k}^{n+1}-q_{i-\frac{1}{2},j,k}^{n+1}}{\Delta x_i} - (1-\omega)\cdot\frac{q_{i+\frac{1}{2},j,k}^{n}-q_{i-\frac{1}{2}.j.k}^{n}}{\Delta x_i}\right) +$$
$$\left(-\omega\cdot\frac{q_{i,j+\frac{1}{2},k}^{n+1}-q_{i,j-\frac{1}{2},k}^{n+1}}{\Delta y_j} - (1-\omega)\cdot\frac{q_{i,j+\frac{1}{2},k}^{n}-q_{i.j-\frac{1}{2},k}^{n}}{\Delta y_j}\right) + \qquad [4.42]$$
$$\left(-\omega\cdot\frac{q_{i,j,k+\frac{1}{2}}^{n+1}-q_{i,j,k-\frac{1}{2}}^{n+1}}{\Delta z_k} - (1-\omega)\cdot\frac{q_{i,j,k+\frac{1}{2}}^{n}-q_{i.j.k-\frac{1}{2}}^{n}}{\Delta z_k}\right)$$

Rearrange Equation 4.42 to the follows:

$$\frac{\omega}{\Delta x_i}\left(k^{n+1}_{i+\frac{1}{2},j,k}\cdot\frac{\eta^{n+1}_{i+1,j,k}-\eta^{n+1}_{i,j,k}}{x_{i+1}-x_i}-k^{n+1}_{i-\frac{1}{2},j,k}\cdot\frac{\eta^{n+1}_{i,j,k}-\eta^{n+1}_{i-1,j,k}}{x_i-x_{i-1}}\right)+$$
$$\frac{\omega}{\Delta y_j}\left(k^{n+1}_{i,j+\frac{1}{2},k}\cdot\frac{\eta^{n+1}_{i,j+1,k}-\eta^{n+1}_{i,j,k}}{y_{j+1}-y_j}-k^{n+1}_{i,j-\frac{1}{2},k}\cdot\frac{\eta^{n+1}_{i,j,k}-\eta^{n+1}_{i,j-1,k}}{y_j-y_{j-1}}\right)+$$
$$\frac{\omega}{\Delta z_k}\left(k^{n+1}_{i,j,k+\frac{1}{2}}\cdot\frac{\eta^{n+1}_{i,j,k+1}-\eta^{n+1}_{i,j,k}}{z_{k+1}-z_k}-u^{n+1}_{k+\frac{1}{2}}-k^{n+1}_{i,j,k-\frac{1}{2}}\cdot\frac{\eta^{n+1}_{i,j,k}-\eta^{n+1}_{i,j,k-1}}{z_k-z_{k-1}}+u^{n+1}_{k-\frac{1}{2}}\right)=$$
$$\frac{\xi^{n+1}_{i,j,k}-\xi^{n}_{i,j,k}}{\Delta t}+(1-\omega)\cdot\frac{q^n_{i+\frac{1}{2},j,k}-q^n_{i+\frac{1}{2}.j.k}}{\Delta x_i}+(1-\omega)\cdot\frac{q^n_{i,j+\frac{1}{2},k}-q^n_{i.j+\frac{1}{2},k}}{\Delta y_j}+(1-\omega)\cdot\frac{q^n_{i,j,k+\frac{1}{2}}-q^n_{i.j.k+\frac{1}{2}}}{\Delta z_k}$$

[4.43]

To solve the above discrete water equation, the initial and boundary conditions are required. The initial condition involves the values (water pressure head, hydraulic conductivity, elevation head) when t=0. The boundary condition can be given as flux (Neumann condition) or as fixed value (Dirichlet condition). The flux condition is written as:

$$\begin{aligned}
&q=-k\cdot\nabla\eta+u=q_{c_o}(t,\eta) \quad x=0\\
&q=-k\cdot\nabla\eta+u=q_{c_n}(t,\eta) \quad x=c\\
&q=-k\cdot\nabla\eta+u=q_{r_o}(t,\eta) \quad y=0\\
&q=-k\cdot\nabla\eta+u=q_{r_n}(t,\eta) \quad y=r\\
&q=-k\cdot\nabla\eta+u=q_{l_o}(t,\eta) \quad z=0\\
&q=-k\cdot\nabla\eta+u=q_{l_n}(t,\eta) \quad z=l
\end{aligned}$$

[4.44]

It is assumed that the domain contains from 1 to c columns in x direction, from 1 to r rows in y direction, and from 1 to l layers in z direction. When applying Neumann condition in Equation 4.44, there are six boundary conditions: back, front, left, right, top and bottom.

Back

$$\frac{\xi^{n+1}_{1,j,k}-\xi^{n}_{1,j,k}}{\Delta t}=\left(-\omega\cdot\frac{q^{n+1}_{1,j,k}-q^{n+1}_{c_o,j,k}}{\Delta x_1}-(1-\omega)\cdot\frac{q^n_{1,j,k}-q^n_{c_o.j.k}}{\Delta x_1}\right)$$

[4.45]

Front

$$\frac{\xi_{c,j,k}^{n+1}-\xi_{c,j,k}^{n}}{\Delta t}=\left(-\omega\cdot\frac{q_{c_n,j,k}^{n+1}-q_{c,j,k}^{n+1}}{\Delta x_c}-(1-\omega)\cdot\frac{q_{c_n,j,k}^{n}-q_{c.j.k}^{n}}{\Delta x_c}\right) \quad [4.46]$$

Left

$$\frac{\xi_{i,1,k}^{n+1}-\xi_{i,1,k}^{n}}{\Delta t}=\left(-\omega\cdot\frac{q_{i,1,k}^{n+1}-q_{i,r_o,k}^{n+1}}{\Delta y_1}-(1-\omega)\cdot\frac{q_{i,1,k}^{n}-q_{i,r_o,k}^{n}}{\Delta y_1}\right) \quad [4.47]$$

Right

$$\frac{\xi_{i,r,k}^{n+1}-\xi_{i,r,k}^{n}}{\Delta t}=\left(-\omega\cdot\frac{q_{i,r_n,k}^{n+1}-q_{i,r,k}^{n+1}}{\Delta y_r}-(1-\omega)\cdot\frac{q_{i,r_n,k}^{n}-q_{i,r,k}^{n}}{\Delta y_r}\right) \quad [4.48]$$

Top

$$\frac{\xi_{i,j,1}^{n+1}-\xi_{i,j,1}^{n}}{\Delta t}=\left(-\omega\cdot\frac{q_{i,j,1}^{n+1}-q_{i,j,l_o}^{n+1}}{\Delta z_1}-(1-\omega)\cdot\frac{q_{i,j,1}^{n}-q_{i,j,l_o}^{n}}{\Delta z_1}\right) \quad [4.49]$$

Bottom

$$\frac{\xi_{i,j,}^{n+1}-\xi_{i,j,l}^{n}}{\Delta t}=\left(-\omega\cdot\frac{q_{i,j,l_n}^{n+1}-q_{i,j,l}^{n+1}}{\Delta z_l}-(1-\omega)\cdot\frac{q_{i,j,l_n}^{n}-q_{i.j.l}^{n}}{\Delta z_l}\right) \quad [4.50]$$

Until now, the water balance equation has been discretized into Equation 4.43 among the domain, and Equations 4.45 to 4.50 on the boundary.

4.4 Iterative Scheme

When the water conservation equation is converted to the algebraic nonlinear equations, the following work is to solve the nonlinear equations solved with the appropriate iterative method. One common

way is to use the fixed point iteration which is a method of computing fixed points of iterated functions. Specifically, given η=g(η), the fixed value problem, where x=g(x) is the solution, and given a point, $\eta_{0,}$ in the domain of g, the succession $\eta^{m+1}=g(\eta^{m})$, m=0,1,2…, gives rise to the fixed point iteration on the real number with real values in η that are expected to converge to the solution x. This succession is also called Picard iteration and converges if $|f'(x_k)|<1$ k=0, 1, 2…, m-1 [Gambolati, 1994].

Write Equation 4.43 as the iterated form:

$$\frac{\omega}{\Delta x_i}\left(k^{n+1,m}_{i+\frac{1}{2},j,k}\frac{\eta^{n+1,m+1}_{i+1,j,k}-\eta^{n+1,m+1}_{i,j,k}}{x_{i+1}-x_i}-k^{n+1,m}_{i-\frac{1}{2},j,k}\cdot\frac{\eta^{n+1,m+1}_{i,j,k}-\eta^{n+1,m+1}_{i-1,j,k}}{x_i-x_{i-1}}\right)+$$
$$\frac{\omega}{\Delta y_j}\left(k^{n+1,m}_{i,j+\frac{1}{2},k}\cdot\frac{\eta^{n+1,m+1}_{i,j+1,k}-\eta^{n+1,m+1}_{i,j,k}}{y_{j+1}-y_j}-k^{n+1,m}_{i,j-\frac{1}{2},k}\cdot\frac{\eta^{n+1,m+1}_{i,j,k}-\eta^{n+1,m+1}_{i,j-1,k}}{y_j-y_{j-1}}\right)+$$
$$\frac{\omega}{\Delta z_k}\left(k^{n+1,m}_{i,j,k+\frac{1}{2}}\cdot\frac{\eta^{n+1,m+1}_{i,j,k+1}-\eta^{n+1,m+1}_{i,j,k}}{z_{k+1}-z_k}-u^{n+1,m}_{k+\frac{1}{2}}-k^{n+1,m}_{i,j,k-\frac{1}{2}}\cdot\frac{\eta^{n+1,m+1}_{i,j,k}-\eta^{n+1,m+1}_{i,j,k-1}}{z_k-z_{k-1}}+u^{n+1,m}_{k-\frac{1}{2}}\right)=$$
$$\frac{\xi^{n+1,m+1}_{i,j,k}-\xi^{n}_{i,j,k}}{\Delta t}+(1-\omega)\cdot\frac{q^{n}_{i+\frac{1}{2},j,k}-q^{n}_{i+\frac{1}{2}.j.k}}{\Delta x_i}+(1-\omega)\cdot\frac{q^{n}_{i,j+\frac{1}{2},k}-q^{n}_{i.j+\frac{1}{2}.k}}{\Delta y_j}+(1-\omega)\cdot\frac{q^{n}_{i,j,k+\frac{1}{2}}-q^{n}_{i.j.k+\frac{1}{2}}}{\Delta z_k}$$

[4.51]

where the unknowns are $\eta^{n+1,m+1}$ and $\xi^{n+1,m+1}$ in the left and right hand side, respectively. The quantity $\xi^{n+1,m+1}_{i,j,k}$ is calculated with a first-order Taylor series:

$$\xi^{n+1,m+1}_{i,j,k}\approx\xi^{n+1,m}_{i,j,k}+C^{n+1,m}_{i,j,k}(\eta^{n+1,m+1}_{i,j,k}-\eta^{n+1,m}_{i,j,k}) \quad [4.52]$$

$$C^{n+1,m}_{i,j,k}=\left.\frac{\partial\xi}{\partial\eta}\right|_{\eta^{n+1,m}} \quad [4.53]$$

Where $C^{n+1,m}_{i,j,k}$ is the capacity function evaluated for the cell (i,j,k) at the instant t^{n+1}. Replace Equation 4.52 into Equation 4.51, and the result is:

$$a \cdot \eta_{i+1,j,k}^{n+1,m+1} + b \cdot \eta_{i-1,j,k}^{n+1,m+1} + c \cdot \eta_{i,j,k}^{n+1,m+1} + d \cdot \eta_{i,j+1,k}^{n+1,m+1} + e \cdot \eta_{i,j-1,k}^{n+1,m+1} + f \cdot \eta_{i,j,k+1}^{n+1,m+1} + g \cdot \eta_{i,j,k-1}^{n+1,m+1} = RHS$$

[4.54]

where the coefficients a, b, c, d, e, f, g, and RHS are defined as:

$$a = \frac{\omega \cdot k_{i+\frac{1}{2},j,k}^{n+1,m}}{\Delta x_i \cdot (x_{i+1} - x_i)}$$

[4.55]

$$b = \frac{\omega \cdot k_{i-\frac{1}{2},j,k}^{n+1,m}}{\Delta x_i \cdot (x_i - x_{i-1})}$$

[4.56]

$$c = -\frac{\omega \cdot k_{i+\frac{1}{2},j,k}^{n+1,m}}{\Delta x_i \cdot (x_{i+1} - x_i)} - \frac{\omega \cdot k_{i-\frac{1}{2},j,k}^{n+1,m}}{\Delta x_i \cdot (x_i - x_{i-1})} - \frac{\omega \cdot k_{i,j+\frac{1}{2},k}^{n+1,m}}{\Delta y_j \cdot (y_{j+1} - y_j)} - \frac{\omega \cdot k_{i,j-\frac{1}{2},k}^{n+1,m}}{\Delta y_j \cdot (y_j - y_{j-1})}$$
$$- \frac{\omega \cdot k_{i,j,k+\frac{1}{2}}^{n+1,m}}{\Delta z_k \cdot (z_{k+1} - z_k)} - \frac{\omega \cdot k_{i,j,k-\frac{1}{2}}^{n+1,m}}{\Delta z_k \cdot (z_{k+1} - z_k)} - \frac{C_{i,j,k}^{n+1,m}}{\Delta t}$$

[4.57]

$$d = \frac{\omega \cdot k_{i,j+\frac{1}{2},k}^{n+1,m}}{\Delta y_j \cdot (y_{j+1} - y_j)}$$

[4.58]

$$e = \frac{\omega \cdot k_{i,j-\frac{1}{2},k}^{n+1,m}}{\Delta y_j \cdot (y_j - y_{j-1})}$$

[4.59]

$$f = \frac{\omega \cdot k_{i,j,k+\frac{1}{2}}^{n+1,m}}{\Delta z_k \cdot (z_{k+1} - z_k)}$$

[4.60]

$$g = \frac{\omega \cdot k_{i,j,k-\frac{1}{2}}^{n+1,m}}{\Delta z_k \cdot (z_{k+1} - z_k)}$$

[4.61]

$$RHS = \frac{\xi_{i,j,k}^{n+1,m} - \xi_{i,j,k}^{n} - C_{i,j,k}^{n+1,m} \cdot \eta_{i,j,k}^{n+1,m}}{\Delta t} + (1-\omega) \cdot \left(\frac{q^{n}_{i+\frac{1}{2},j,k} - q^{n}_{i+\frac{1}{2},j,k}}{\Delta x_i} + \frac{q^{n}_{i,j+\frac{1}{2},k} - q^{n}_{i,j+\frac{1}{2},k}}{\Delta y_j} + \frac{q^{n}_{i,j,k+\frac{1}{2}} - q^{n}_{i,j,k+\frac{1}{2}}}{\Delta z_k} \right)$$

$$+ \frac{\omega}{\Delta z_k} \cdot \left(u^{n+1,m}_{k+\frac{1}{2}} - u^{n+1,m}_{k-\frac{1}{2}} \right)$$

[4.62]

The finite-difference Equation 4.54 for the water conservation equation is written in a traditional form explicating the unknown η^{n+1}. The solution of the matrix can then be obtained through linear solvers, such as BICGSTAB used in GEOtop. Understanding the numerical scheme of GEOtop, it is beneficial to manage the parameters applied in the model, which is described in the next chapter.

Chapter 5

Soil Parameterisation

5.1 Soil Water Parameterization

Soil is the composition of mineral and void that is filled by water, air or ice. The soil moisture can vary considerably between the residual water content (completely dry, θ_r) and saturated water content (effective porosity, θ_s). Prominently, the soil water is dynamic in the porous medium. The soil water content varies depending on the water potential differences in the soil medium and the water potential is closely related to the soil moisture saturation. Further, the soil composition (e.g., fine and coarse material, organic content, etc.) dictates the water potential when a soil reaches its point of saturation. Moreover, the rate of water flow is determined by the gradient of the water potential, soil permeability and water viscosity.

Besides the water potential, the hydraulic conductivity is an important parameter in the process of water movement, which combines the function of soil permeability and water viscosity. For the present study, the hydraulic conductivity varies by up to two orders of magnitude in the Wolf Creek basin (Table 5.1). Therefore, the parameterisation of soil moisture characteristic must be considered attentively to represent precisely the quantitative relation between water content, water potential, and hydraulic conductivity, which is the key point to study soil moisture dynamics.

Table 5.1 Wolf Creek north-facing slope soil properties. K_s is saturated hydraulic conductivity and θ_{sc} is specific retention (Carey, 2000)

	Upper Organic	Lower Organic	Mineral Soil
Bulk density (kg m^{-3})	55±20	90±20	1340±180
Porosity (%)	92±4	84±10	52±7
K_s (m s^{-1})	$7±4\times10^{-3}$	$2.5±2\times10^{-4}$	$5±7\times10^{-9}$
θ_{sr}	0.44±0.09	0.49±0.08	0.42±0.05

5.1.1 Water Potential

Water potential is the potential energy of water per unit volume relative to a pure water reference. Soil water flows from areas of higher to areas of lower water potential. The potential energy of a body or a system is the energy (N m or J) related to the position of the body or the arrangement of the particles of the system. Therefore, the water potential (Ψ) entails the same unit as that of pressure (J m^{-3} or Pa). To deduce the total water potential, several components related to the water pressure are involved (Equation 5.1):

$$\Psi = \Psi_z + \Psi_p + \Psi_s + \Psi_a \qquad [5.1]$$

where:

Ψ_z is the gravitational potential (Pa),
Ψ_p is the pressure potential (Pa),
Ψ_s is the solute potential (Pa),
Ψ_a is the air pressure potential (Pa)

Nevertheless, in practical application, the total water potential is found simply by considering just the gravitational pressure ($\Psi_z=\rho\cdot g\cdot Z$) and the capillary pressure ($\Psi_p=\rho\cdot g\cdot \psi$) while the other items are neglected.

It is hard to describe the relationship between water potential and soil saturation in a mathematic equation for soil types. However, the quantities of the water potentials are defined at several specific points of the water content. For instance, the pressure at the free water surface in saturated soil is equal to the atmospheric pressure (101.325 kPa or approximately 1 bar), which is regarded as the pressure reference. Therefore, the water potential at the water table is normally defined as 0 kPa. Further, the water potential of the unsaturated soil is negative and so treated as a suction pressure in the model. The field capacity (also called specific retention, θ_{fc}) is the ratio of the volume of water which the soil, after being saturated, retains against the pull of gravity to the volume of the soil. In the application, the water potential used for the field capacity is -33kPa. The permanent wilting point (θ_{wp}), the minimal point of soil moisture required for plants not to wilt, is generally considered to be the soil water potential of −1500 kPa. The residual water content, that is, the minimum level of moisture in the soil that can be attained in natural field conditions, is practically assumed to be -3100 kPa.

Water content is considerably variable among different soil types. For instance, in the study area, the volumetric saturated moisture content may be as high as 92% in the organic soil layer but only up to 52% in the mineral layer (Table 5-1). Therefore, the effective saturation, S, is usually used instead of the actual water content to depict the relationship between soil water content and water potential. The effective saturation (dimensionless) is the normalized water content described in Equation 5.2. The effective saturation value varies in the range of 0 and 1.

$$S = \frac{\theta - \theta_r}{\theta_s - \theta_r} \qquad [5.2]$$

where

θ is the volumetric water content (m^3/m^3),
θ_r is the residual water content (m^3/m^3),
θ_s is the saturated water content (m^3/m^3), which is equivalent to porosity (ϕ).

5.1.2 Hydraulic Conductivity

According to Darcy's law, the soil water discharge, Q (m^3 s^{-1}), is equal to the product of the permeability of the medium, κ (m^2), the cross-sectional area to flow, A (m^2), and the pressure drop, ΔΨ (Pa), all divided by the viscosity, μ (Pa s), and the length over which the pressure drop occurs, Δx (m). The equation is described as below:

$$Q = -A \cdot \frac{\kappa}{\mu} \cdot \frac{\Delta \Psi}{\Delta x} \qquad [5.3]$$

The hydraulic conductivity (L T^{-1}) is the ratio of Darcy's velocity to the hydraulic head, h= ψ+z (m), gradient by the length over which the water head drop occurs, Δx (m). The equation is described as below:

$$\frac{Q}{A} = -K \cdot \frac{\Delta h}{\Delta x} \qquad [5.4]$$

Therefore, the relationship between the permeability and the hydraulic conductivity is

$$\kappa = K \cdot \frac{\mu}{\rho g} \qquad [5.5]$$

where:

κ is the permeability (m^2)
K is the hydraulic conductivity ($m \cdot s^{-1}$)
μ is the dynamic viscosity ($kg \cdot m^{-1} \cdot s^{-1}$)
ρ is the density of the fluid ($kg \cdot m^{-3}$)
g is the acceleration due to gravity ($m \cdot s^{-2}$).

Permeability is a property of the porous material while hydraulic conductivity is related to the properties of water and the porous material. Based on Hagen–Poiseuille equation for viscous flow in a pipe, permeability can be expressed as:

$$\kappa = c \cdot d^2 \qquad [5.6]$$

where:

κ is the intrinsic permeability (m^2);
c is a dimensionless constant that is related to the configuration of the flow-paths;
d is the average, or effective pore diameter (m).

According to Equation 5.5, Hydraulic conductivity is determined by the intrinsic permeability of the material and the viscosity of water. For the saturated soil, the hydraulic conductivity value is estimated by the parameters in the Equation 5.5 and 5.6.

5.1.3 Soil Moisture Characteristic Model

When the soil is saturated, the hydraulic conductivity can be calculated by soil permeability and water viscosity using Equation 5.5. Similarly, the water potential is also relatively easy to compute, which is only comprised of the gravity pressure. However, when the soil is unsaturated, the effective saturation must be included in the hydraulic conductivity and water potential models. The relative hydraulic conductivity, i.e., the ratio of the unsaturated conductivity to the saturated conductivity ($K_r=K/K_s$), is also used in the models.

The Brooks-Corey (1964) and Van-Genuchten (1980) soil moisture characteristic models are widely applied for their effectiveness (Table 5.2). The Brooks-Corey model involves the air entry pressure head (ψ_{ae}), which is the pressure required to force air through the soil pores in a saturated medium. Further, in the model, the effective saturation and relative hydraulic conductivity are both defined by the ratio of water pressure head to the air entry pressure head. Therefore, the left and right sides of the equations in Brooks-Corey model are both dimensionless. By comparison, in the Van-Genuchten

model, the right side of the equations is water pressure head, while the left sides are effective saturation and relative hydraulic conductivity that are both dimensionless without the unit. Therefore, The Van-Genuchten model is an empirical model, which represents the quantitative relationship of these parameters based on experiment results. In GEOtop, both the Brooks-Corey and Van-Genuchten soil moisture characteristic models are available for the simulation. For the purpose of this study, the Van-Genuchten model is adopted because of its better performance.

Table 5.2 Soil moisture characteristic models of Brooks-Corey and Van-Genuchten

<table>
<tr><th>model</th><th colspan="2">hydraulic functions</th><th>Legend</th></tr>
<tr><td rowspan="2">Brooks-Corey</td><td>$\psi<\psi_{ae}$</td><td>$S=\left(\frac{\psi}{\psi_{ae}}\right)^{-\lambda}\quad k_r=\left(\frac{\psi}{\psi_{ae}}\right)^{-2-3\lambda}$</td><td rowspan="2">$\lambda$: pore size distribution index
ψ_{ae}: air entry pressure head</td></tr>
<tr><td>$\psi>=\psi_{ae}$</td><td>$S=1\quad k_r=1$</td></tr>
<tr><td rowspan="2">Van-Genuchten</td><td>$\psi<0$</td><td>$S=\frac{1}{[1+(\alpha\psi)^n]^m}$
$k_r=\frac{\{1-(\alpha\psi)^{n-1}[1+(\alpha\psi)^n]^{-m}\}^2}{[1+(\alpha\psi)^n]^{m/2}}$</td><td rowspan="2">$\alpha$ and n: empirical parameters
$m=1-\frac{1}{n}$</td></tr>
<tr><td>$\psi>0$</td><td>$S=1\quad k_r=1$</td></tr>
</table>

5.2 Soil Thermal Parameterisation

In cold regions, the active layer which alternates between the frozen and the unfrozen condition is overlain by permafrost. The hydrological processes are generally confined in the active layer. To simulate the active layer, the soil thermal properties must be represented precisely for determining ground thawing and freezing depths. In the study site, the variation of thermal properties is prominent along the soil depth (Table 5.3), especially the heat capacity. Further, due to the ice and water phase transformation, the thermal conductivity and heat capacity of the soil are not stable near the different state of the soil freezing and thaw.

Table 5.3 Volumetric composition of soils with depth and the thermal properties of the components (Quinton, 2005)

Type	Depth (m)	Porosity φ	Density (kg m^{-3})	Specific heat (J kg^{-1} K^{-1})	Heat capacity (J m^{-3} K^{-1})	Thermal cond. (W m^{-1} K^{-1})
Organic soil	0.05-0.15	0.96	41.1	1920	78912	0.21
Organic soil	0.15-0.25	0.90	75.2	1920	144384	0.21
Organic soil	0.25-0.35	0.87	91.4	1920	175392	0.21
Mineral soil	0.35-0.45	0.43	1300	890	1157000	2.5
air	-	-	1.2	1010	1212	0.025
ice	-	-	920	2120	195040	2.24
water	-	-	1000	4185	418500	0.57

Among the available approach to parameterising soil thermal properties, Johansen's parameterization and quadratic parallel parameterization are described as below, and the latter is applied in the current command loop of GEOtop. Both these parameterizations involve the individual thermal properties of soil particles, air, ice and water with their own individual mixing approach.

5.2.1 Johansen's Soil Thermal Model

The method developed by Johansen (1975) is applicable to unfrozen or frozen soils. The equation expresses the thermal conductivity of an unsaturated soil as a function of its thermal conductivity in the dry and the saturated states at the same dry density. This is done by introducing a normalized thermal conductivity, the Kerstern number, K_e, given by:

$$K_e = \frac{\lambda - \lambda_{dry}}{\lambda_{sat} - \lambda_{dry}} \qquad [5.5]$$

where λ, λ_{dry}, and λ_{sat} are the thermal conductivities (W m^{-1} K^{-1}) at an intermediate degree of saturation, dry and saturated state, K_e is dimensionless. The empirical equation for λ_{dry} is as follows:

$$\lambda_{dry} = \frac{0.135\gamma_d + 64.7}{2700 - 0.947\gamma_d} \pm 20\% \quad [5.6]$$

where γ_d is the dry density (kg m^{-3}), assumed to be 2700 kg m^{-3}. To calculate the thermal conductivity of saturated frozen soil, Johansen proposed the use of a geometric mean equation based on the thermal conductivity of the components and their respective volume fractions.

$$\lambda_{sat} = \lambda_s^{1-\phi} \cdot \lambda_i^{\phi-\theta} \cdot \lambda_w^{\theta} \quad [5.7]$$

where λ_s, λ_i, and λ_w are the thermal conductivities (W m^{-1} K^{-1}) of soil particle, ice, and water, ϕ is the porosity and θ is the fractional volume of the unfrozen water.

On the basis of Kerstern's data, Johansen found that for any type of frozen soil, the Kerstern number is equal to the effective saturation, $K_e = S$ (with a variation less than 0.1). The thermal conductivity of an unsaturated frozen soil may then be calculated from Equation 5.8:

$$\lambda = (\lambda_{sat} - \lambda_{dry}) \cdot K_e + \lambda_{dry} \quad [5.8]$$

Obviously Johansen's method is a technique for interpolating between the dry and the saturated values of the thermal conductivity on the basis of the degree of soil saturation.

5.2.2 Quadratic Parallel Model

Generally, the behavior of multiphase media is complex, so the approach used to determine any bulk physical properties is derived from experiments. Johansen's equation describes the thermal conductivity according to geometrical law. The other mixing law is also available to determine the

soil thermal properties as the quadratic parallel methods [Cosenza, 2003]. The quadratic parallel model is applied in GEOtop, and the equation is as follow:

$$\lambda = \left(\sum_{i=1}^{n} x_i \sqrt{\lambda_i} \right)^2 \qquad [5.9]$$

where x_i (dimensionless) and λ_i (W m^{-1} K^{-1}) are the fraction and thermal conductivity of the i-th phase component.

In GEOtop, the volumetric heat capacity of frozen soil is calculated by the mixing law.

$$C = \sum_{i=1}^{n} x_i C_i \qquad [5.10]$$

where x_i (dimensionless) and C_i (J m^{-3} K^{-1}) are the fraction and heat capacity of the i-th phase component.

5.3 Unfrozen Water Content of Frozen Soil

The unfrozen water appears to play an important role on the physical properties of unfrozen and frozen soil. In the unfrozen condition, the soil moisture characteristic model does not require soil temperature. By contrast, in the frozen condition, the soil liquid moisture pressure and temperature are not independent so temperature is required. Their relation can be defined using the state equation. The state equation describes the relationship between water pressure and temperature in frozen soils. According to the 'freezing=drying' assumption, when the ice pressure is neglected, the generalized Clapeyron equation becomes:

$$\rho_w L_f \frac{dT}{T} = dp \qquad [5.11]$$

where p (Pa) is the liquid moisture pressure, T is the temperature of the soil (K), ρ_w is the density of water (kg m^{-3}), and L_f is the latent heat of fusion (J kg^{-1}). Equation 5.11 states that the variation of water pressure during phase change is dependent on water temperature.

In the special condition when the water pressure is equal to the atmospheric pressure, p_a, the water temperature is the melting temperature (T_m). Between frozen and melting status, integrate Equation 5.11 and the result is as follows:

$$\int_{T_m}^{T} \rho_w L_f \frac{dT}{T} = \int_{p_a}^{p} dp \qquad [5.12]$$

The left side of Equation 5.12 may be approximated as:

$$\int_{T_m}^{T} \rho_w L_f \frac{dT}{T} = \rho_w L_f \ln\left(\frac{T}{T_m}\right) \approx \rho_w L_f \frac{T - T_m}{T_m} \qquad [5.13]$$

Usually, the atmospheric pressure is set to zero (p_a=0). Combining Equations 5.12 and 5.13, Equation 5.14 is obtained:

$$\rho_w L_f \frac{T - T_m}{T_m} = \int_0^p dp = p \qquad [5.14]$$

Considering that p<0 and $p = \Psi$, the liquid water potential, Ψ, is subjected to freezing conditions:

$$\Psi = \frac{\rho_w L_f}{T_m}(T - T_m) \qquad [5.15]$$

When soil is saturated and water pressure is equal to the atmospheric pressure, the melting point T_m is 273.15 K. If the soil is unsaturated, the surface tension at the water-air interface decreases the water melting temperature to a value $T^* < T_m$. If we choose the soil status as water pressure (Ψ_0<0), the value of T*, is found by integrating Equation 5.12 in temperature from T_m to the unknown T*.

$$\int_{T_m}^{T^*} \rho_w L_f \frac{dT}{T} = \int_0^{\Psi_0} dp \qquad [5.16]$$

The solution of Equation 5.16 provides the lower melting temperature T* at unsaturated conditions:

$$T^* = T_m + \frac{T_m}{\rho_w L_f} \Psi_0 \qquad [5.17]$$

Therefore, in unsaturated condition, the melting temperature T* decrease depends on the water pressure. When T>=T*, the soil is unfrozen whereas when T<T*, the soil is under freezing conditions.

In a frozen condition, the liquid moisture pressure p depends on the intensity of the freezing condition provided by T, which may be found by integrating Equation 5.12 in pressure from $\Psi_0=p_0$ to $\Psi=p$ and in temperature from T* to T, as follows:

$$\int_{T^*}^{T} \rho_w L_f \frac{dT}{T} = \int_{\Psi_0}^{\Psi} dp \qquad [5.18]$$

Consequently, the solution of integration is:

$$\psi = \psi_0 + \frac{\rho_w L_f}{T^*}(T - T^*) \qquad [5.19]$$

Equation 5.19 is valid for T<T*. In fact, when T>=T*, the liquid water pressure is equal to the Ψ_0. If the soil is saturated, $\Psi_0=0$. Thus the formulation of the liquid water pressure, Ψ, under freezing conditions, for both saturated and unsaturated soils is:

$$\begin{cases} \psi = \psi_0 + \frac{\rho_w L_f}{T^*}(T - T^*) & if \quad T < T^* \\ \psi = \psi_0 & if \quad T \geq T^* \end{cases} \qquad [5.20]$$

which can be summarized using the Heaviside function H (), whose value is zero for the negative argument and unity for the positive argument, as:

$$\Psi = \Psi_0 + \frac{\rho_w L_f}{T^*}(T - T^*) \cdot H(T^* - T) \qquad [5.21]$$

Consequently, because the Van Genuchten equation is applied in the model, the equation to describe the thermodynamically allowed liquid water content at subfreezing temperatures is determined as follows:

$$\psi = \frac{1}{\alpha} \cdot \left[S^{-\frac{1}{m}} - 1 \right]^{\frac{1}{n}} = \frac{\Psi}{\rho_w \cdot g} = \frac{\Psi_0}{\rho_w \cdot g} + \frac{L_f}{g \cdot T^*} \cdot (T - T^*) \cdot H(T^* - T) \qquad [5.22]$$

Or $$\frac{\Psi_0}{\rho_w \cdot g} + \frac{L_f}{g \cdot T^*} \cdot (T - T^*) \cdot H(T^* - T) = \frac{1}{\alpha} \cdot \left[S^{-\frac{1}{m}} - 1 \right]^{\frac{1}{n}} \qquad [5.23]$$

Therefore, Equation 5.21 is used to determine the liquid water content at sub-zero temperatures and is usually called “freezing-point depression equation.”

Chapter 6

Validation of GEOtop for Active Layer Thaw

GEOtop calculates the energy and mass balance in the area of interest (AOI) through a 3D solver for the Richards equation and a 1D solver for the energy equation in order to obtain the converged solution. The converged solution is obtained only when the balance of coupled energy and water flow is closed by the iterative scheme in all the discrete cells. However, validating the model is necessary to ascertain how representative of the true conditions in the AOI the variables used in the model are. The credibility of simulation performance applying these appropriate variables will be determined by the comparison of the field measurements. Thus the research objectives can be addressed using the validated results.

The simulation of active layer thaw plays a central role in the coupled energy and water computation because the process of soil thaw is determined by both the energy conducted through the soil surface and the soil thermal properties. The effectiveness of simulating the active layer thaw is critically dependent to the land surface energy fluxes on subalpine terrain in the cold regions. Further, the soil thaw is highly influenced by the water content. In the process, the dynamics of soil moisture includes ice phase changes resulting from the temperature rise and liquid water flow resulting from the water potential variability. The soil thaw indexes, frost table depth and point soil temperature, are used to validate the model.

6.1 Model Variables

The variables used in the model are categorized into three types: initial variables (initial temperature, t, and total water pressure, p); soil property variables (saturated hydraulic conductivity, K_s, unfrozen moisture content, θ_u, saturated moisture content, θ_s, solid particle thermal conductivity, λ, and solid particle heat capacity, c); and water retention curve variables (empirical parameters α and n). The total water pressure is the sum of liquid water pressure and ice water equivalent pressure (the water pressure when the ice is regarded as the water in the same quantity). Ideally, the variables of the first two types

have the physical definition, which values are determined by the site or the laboratory experiments. The variables in the expression of Van Genuchten are estimated according to the relationship between water pressure and water content measured in the experiment. The initial temperature is determined by the soil pit data in 2009. Other variables are used considering previous research at the study site (Table 5-1 and Table 5-2).

Another prominent feature of the variables is the spatially heterogeneity of the soil properties, especially in the vertical direction. For instance, the soil porosity and saturated hydraulic conductivity decrease abruptly with depth. Further, the thermal conductivity and heat capacity, relative to the upper organic soil layer, are an order of magnitude higher in the underlying mineral layer. The variables for different soil layer are at maximum close to the field observations. The validation was conducted with the variables shown in Table 6.1.

Table 6.1 Variables of the model

Depth mm	k_s m d^{-1}	Total water pressure mm	Initial soil temperature C	α	n	θ_u	θ_s	λ W m^{-1} K^{-1}	c J m^{-3} K^{-1}
10	128.0	-50	-2.5	0.03	1.8	0.2	0.94	0.2	80000
25	72.3	-50	-2.5	0.03	1.8	0.2	0.94	0.2	80000
35	38.9	-50	-2.5	0.03	1.8	0.2	0.94	0.2	80000
45	24.0	-50	-2.5	0.03	1.8	0.2	0.94	0.2	180000
50	17.0	-50	-2.5	0.03	1.8	0.2	0.94	0.2	180000
80	12.8	100	-2.5	0.03	1.8	0.2	0.92	0.2	180000
100	10.2	100	-2.5	0.03	1.8	0.2	0.92	0.2	180000
120	8.7	100	-2.5	0.03	1.8	0.2	0.92	0.2	180000
150	7.7	100	-2.5	0.03	1.8	0.2	0.92	0.2	180000
250	6.9	100	-2.5	0.03	1.8	0.2	0.85	0.2	360000
350	6.3	100	-2.5	0.03	1.8	0.2	0.85	0.2	360000
450	6.0	100	-2.5	0.03	1.8	0.15	0.5	2.5	1100000
500	5.7	100	-2.5	0.03	1.8	0.15	0.5	2.5	1100000
1000	5.5	100	-2.5	0.03	1.8	0.15	0.5	2.5	1100000

6.2 Frost Table Depth

To validate the active layer thaw modelling, the simulated frost table depth on the cell (1 m × 1 m), on which the energy and water conservation equations are calculated, is compared to the point field measurements. There are 44 measured points in the AOI along four snow survey transects. When the snow-free area increases, more point measurements are available to assess the simulation. Due to the different spatial representations, the measured and simulated frost table depths do not match very well in the shallow thaw depth area (Figure 6.1). When the frost table is shallow on a measured point, this means that the snow cover lasts for long time on this point while the surrounding area is possibly snow free. Therefore, it is hard for the model to correctly determine the starting time of soil thaw.

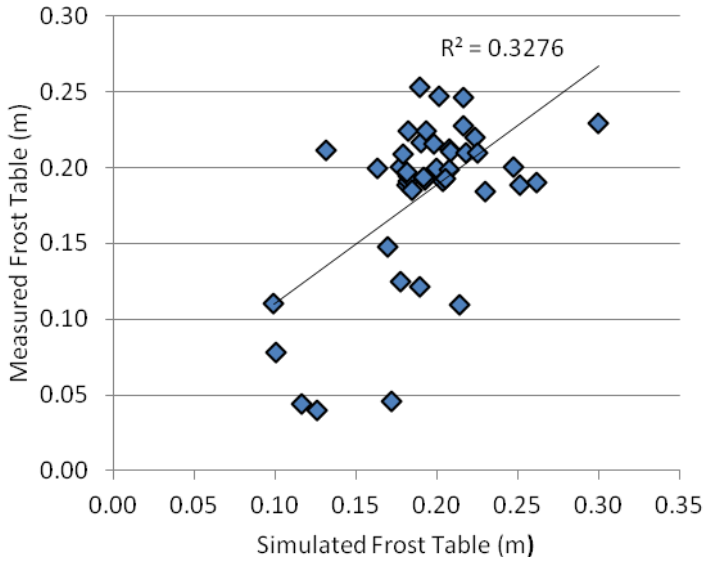

Figure 6.1 Comparison of measured and simulated frost table depth average for the last week of study between May 29 and June 4, 2009

In addition to point comparisons, the frequency distributions, calculated on weekly basis, of measured thaw depths are computed and compared with the correspondent distributions resulting from simulations (Figure 6.2). On May 6, 2009, the AOI was 72% snow covered, with only twenty-two points snow-free and therefore available for frost table depth measurement. As thaw progressed, more points became snow-free, which increased the sample size and improved the statistical quality.

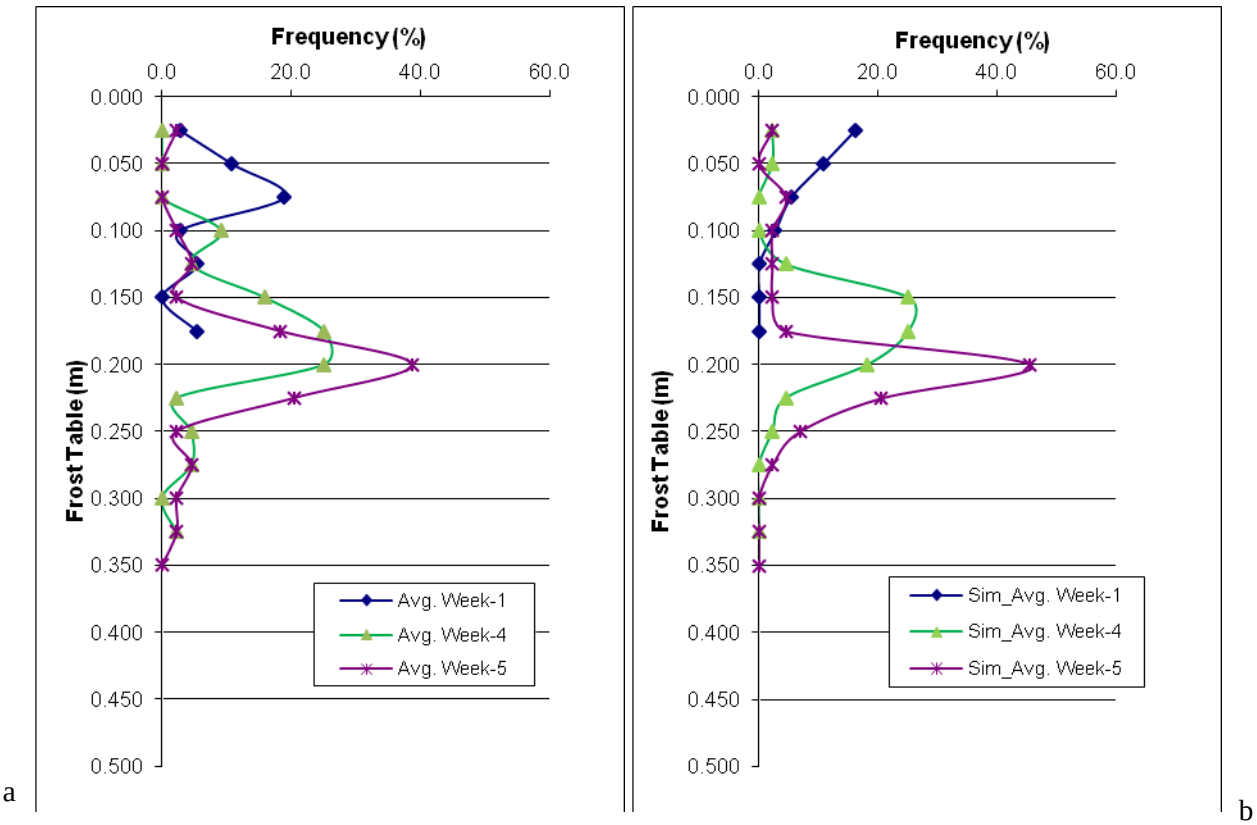

a b

Figure 6.2 A: Measured (A) and Simulated (b) frost table depth frequency distribution

In the first week (April 29 to May 5), the measured frost table depth was between 0 to 17.5 cm, and the simulated depth varied from 0 to 10 cm. The peak of the distribution is 20% with the depth of 7.5 cm in measurement and 17% with the depth of 2.5 cm in simulation. By the fourth week (May 20 to May 26), 40% of the measured frost table depths were between 17.5 and 20 cm while 40% of the simulated frost table depths were between 15 cm and 17.5 cm (Figure 6.2b). In the fifth week, the frequency peaks occurred at 20 cm with the possibility of 40% for measurement (Figure 6.2a) and 45.5% for simulation (Figure 6.2b). The amplitude of both the measured and simulated frequency distribution curve rises from week 1 to week 5, which suggests that frost table depth variation decreases with time.

6.2.1 Non-parametric Statistical Hypothesis Test

The measured (Figure 6.2a) and simulated (Figure 6.2b) frequency distribution curves get gradually closer with time. However, the agreement must be quantified. Since the measured and simulated frost table depths are two independent samples, the Mann-Whitney U test is applied to assess whether one of two samples tends to have larger values than the other. The test involves the calculation of the U-statistic, whose distribution is normal when the sample size is above 20. The procedure of the Mann-Whitney U test is as follows [Lehmann, 1975]:

1. Rank the measured and simulated frost table depths from lowest to highest in a single series. Where the values are the same and share the same rank, take an average of the rank values.
2. Add up the ranks for the measurements. The sum of ranks in simulation follows by calculation, since the sum of all the ranks equals $N(N + 1)/2$ where N is the total number of measurements and simulation.
3. U is determined using Equation 6.1 or 6.2:

$$U_1 = R_1 - \frac{n_1(n_1+1)}{2} \qquad [6.1]$$

$$U_2 = R_2 - \frac{n_2(n_2+1)}{2} \qquad [6.2]$$

where R_1 and n_1 are the sum of the ranks and the sample size for the measured depths, R_2 and n_2 are the sum of the ranks and the sample size for the simulated depths. The statistic, U is the smaller value of U_1 and U_2.

4. U is normally distributed. In that case, the standardized value z is defined using Equation 6.3:

$$z = \frac{U - m_U}{\sigma_U} \qquad [6.3]$$

$$m_U = \frac{n_1 n_2}{2} \qquad [6.4]$$

$$\sigma_U = \sqrt{\frac{n_1 n_2 (n_1 + n_2 + 1)}{12}} \qquad [6.5]$$

where m_U and σ_U are the mean and standard deviation of the statistic U. If the z value does not equal or exceed the critical z value of 1.96 (p <= .05 critical z value for a two-tailed test), then it is assumed that the null hypothesis cannot be rejected and that there is no difference between the measured and simulated values. After the above procedure, the value z is shown in Table 6.2.

Table 6.2 Value of z for the measured and simulated frost table depths

	Week 1	Week 2	Week 3	Week 4	Week 5
z	-2.43	-3.91	-3.16	-1.62	-0.35

The absolute value of z is less than 1.96 in the last two weeks, which indicates that the samples of the simulated and measured frost table depths have no significant difference. For the fourth and fifth week, the hypothesis that the simulated and measured frost table depths comes from the sole population is accepted at the significance of 0.95.

6.3 Soil Temperature

Ten temperature sensors were installed in the soil pit located near the centre of the AOI (Figure 3.1). According to the temperature data, the soil temperature rise was divided into three stages: below freezing point, zero-curtain, and above freezing point (Figure 6.3).

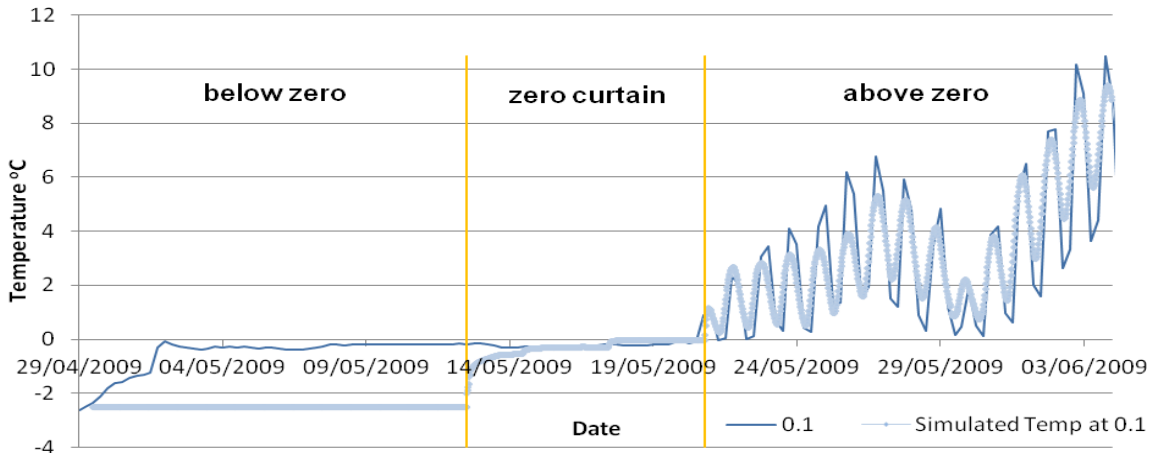

Figure 6.3 Simulated and measured soil temperature at depth of 0.1 m in the soil pit located near the centre of the AOI

When the soil temperature was below the freezing point, the soil temperature rose without ice/water phase change. By contrast, when the soil temperature was in the zero-curtain, the rate of warming was off-set by the latent heat of fusion (334 J g^{-1}) consumed to convert ice into liquid water. When soil temperature was above zero, phase change was limited to the evaporation from the upper layer. When the air temperature was above zero for a large part of the day, the soil temperature increased more rapidly since less energy was required to warm the soil due to the relatively low volumetric heat capacity of the simultaneously increasing air constituent.

For the present study, the measured and simulated soil temperatures are different when the soil is below freezing point (Figure 6.3), which is possibly due to the snow-covered condition around the soil pit. In the model, snow cover is assumed to limit the heat conduction between the soil surface and atmosphere above. Therefore, the simulated soil temperature keeps the negative value before the surface is snow free. However the observed soil temperature increases to zero degree while snow was still present on the ground. In the zero-curtain stage, the measured and simulated temperature is over zero degree on May 20. After that day, the simulated soil temperature corresponds well with the observed value.

For the above zero stage, the Nash–Sutcliffe coefficient is used to assess the modelling performance. The coefficient is defined as:

$$E = 1 - \sum_{i=1}^{n} (T_o^i - T_S^i)^2 / \sum_{i=1}^{n} (T_o^i - \overline{T_o}) \quad [6.6]$$

where T_o^i is the i-th observed soil temperature, T_s^i is the i-th simulated temperature, $\overline{T_o}$ is the average of the observed soil temperature, and n is the number of observed soil temperature. When the temperature is within the zero curtain, the Nash–Sutcliffe coefficient is not applicable for the temperature is not changed. When the temperature is above 0 ^{o}C, the coefficient of the measured and simulated temperature is 0.75.

6.4 Chapter Summary

The 1m × 1 m cell is used in GEOtop for the AOI. In addition, previously measured hydraulic conductivity, heat capacity and thermal conductivity values for the study site are the basis of the corresponding optimized parameters in the model. The model outputs are compared to the measured frost table depth and soil temperature. Through the validation, the numerical performance of the algorithm and the suitability of the spatial-temporal discretisation are examined in the idealized condition where the differences between the measurements and simulations (which are influenced by uncertainties in the atmospheric forcing, uncertainties in the soil and land surface properties, errors or error compensations due to processes not represented by the model) are minimized.

In particular, the dynamics of the active layer is captured with high accuracy, which is of crucial importance in the prospect of simulations involving both the energy and water processes. The modelled active layer thickness is underestimated except for the fifth week when compared to the data, and it is likely that the representation of organic matter in the model would further reduce the model bias. Additionally, the comparison of soil temperatures simulated by the model with the measurements highlights the specific signature of the latent heat effects associated with soil thaw. The representation of

the organic horizon with specific thermal and hydrological characteristics, is confirmed to be a pre-requisite for a realistic modelling of the soil thermal dynamics in the AOI.

Chapter 7

Results and Discussion

7.1 Point Energy Fluxes and Soil Thaw

7.1.1 Energy Fluxes

The surface energy fluxes are computed on the top layer of the model to simulate the components of the energy balance. The energy to lower the frost table is supplied by the ground heat flux. The results of energy fluxes are computed with the assumption that both the snow and the soil albedo remain constant during melting and thawing, and that the small-scale variations in wind direction and speed, and atmospheric temperature and air humidity can be ignored. The assumption is likely justified because the area of interest (AOI) is relatively small area and the angle of the hill slope is generally constant.

The simulated surface energy components of net shortwave Q^*_{SWnet} and longwave Q^*_{LWnet} radiation, sensible heat Q_h, latent heat Q_{le}, and ground heat Q_g consist of the surface energetics in the process of soil thaw. Hence, the equation is described as follows:

$$Q_g = Q^*_{SWnet} + Q^*_{LWnet} - Q_h - Q_{le} \qquad [7.1]$$

where Q_g is the ground heat flux (W m^{-2}), Q^*_{SWnet} is the net shortwave radiation (W m^{-2}), Q^*_{LWnet} is the net longwave radiation (W m^{-2}), Q_h is the sensible heat flux (W m^{-2}), and Q_{le} is the latent heat flux (W m^{-2}). The results of the energy balance for a snow free cell are displayed in Figure 7.1.

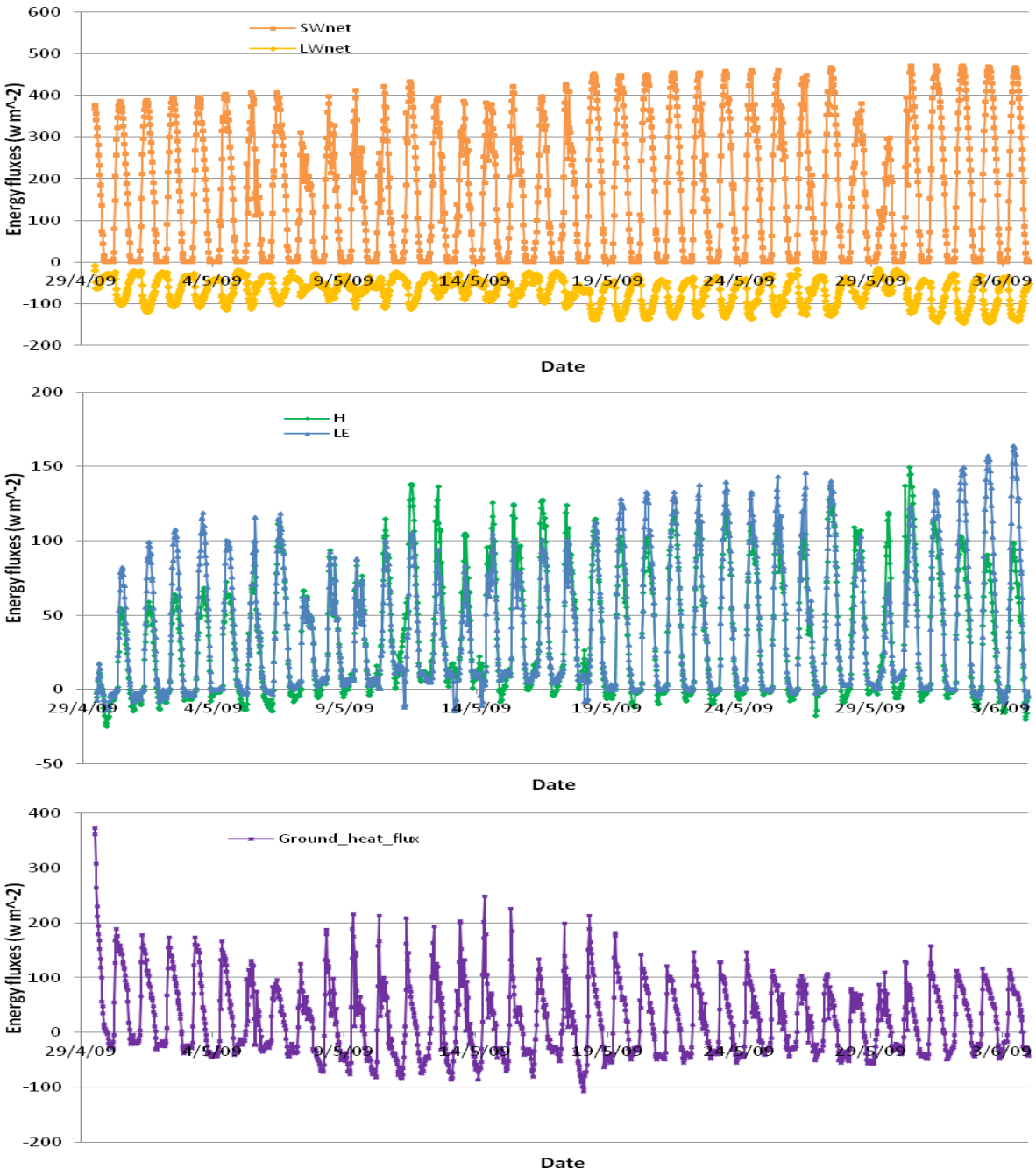

Figure 7.1 Simulated energy fluxes on a single cell in the study period. (a) net shortwave radiation and longwave radiation; (b) sensible and latent heat fluxes; (c) ground heat flux

According to the calculation, the positive energy input is contributed to soil thaw by the net shortwave radiation while the net longwave radiation, sensible heat, and latent heat diffuse the energy from the ground surface. Therefore, because of the diurnal fluctuation of the net shortwave radiation, the ground

heat flux is positive during the day and negative at night, which causes a daily cycle of thawing and refreezing.

According to the energy fluxes simulation (Figure 7.1), the instantaneous net shortwave radiation exceeds 400 W m^{-2} for the clear skies (May 5 to 6, 9 to 11, 15, 17 to 27 and 30 to June 3, 2009), but it is under 300 W m^{-2} when the rainfall occurs on May 29, 2009. The cloudy skies and the snow fall result in the highest shortwave radiation during the day between 300 and 400 W m^{-2}. The daily net shortwave radiation varies from 120 to 210 W m^{-2} (Figure 7.2).

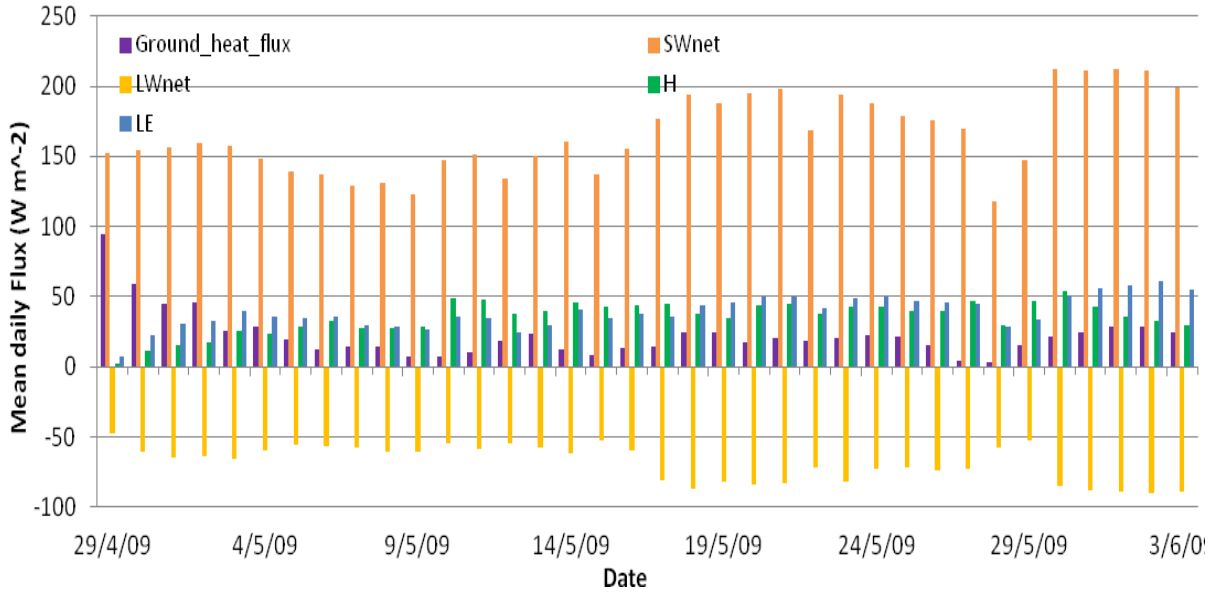

Figure 7.2 Mean daily fluxes of energy terms (net shortwave and longwave radiation, ground heat, sensible and latent heat)

Compared with the shortwave radiation, the maximum of instantaneous ground heat flux is over 200 W m^{-2} on April 29, May 9 to 11, 13 to 15 and 18, and the minimum value is less than -100 W m^{-2} at 2:30 am on May 18. The ground heat flux reaches a peak between 6:30 to 9:30 am and decreases to the bottom in late evening or early morning (Figure 7.1).

According to the daily energy fluxes (Figure 7.2), the magnitude of ground heat flux is higher in the first four days between April 29 and May 2. On the first four consecutive days, the average daily ground heat

flux mounts to 94.7, 59.3, 44.7, and 45.5 W m^{-2}, respectively. The mean ground heat flux is 5.3 MJ m^{-2} d^{-1} for these four days and 1.9 MJ m^{-2} d^{-1} for the whole study period. For instance, on April 29, the ground heat flux is 8.12 MJ m^{-2} d^{-1} (94 W m^{-2}), which comprises ninety percent of the net radiation. The sensible heat and latent heat fluxes are, respectively, 1.97 and 7.70 W m^{-2}, or 0.17 and 0.66 MJ m^{-2} d^{-1}. On May 3 when the frost table is 0.1 cm below the ground surface, the ground heat flux is inhibited while the increasing fraction of the energy is consumed by the sensible and latent heat transfer. As thawing progresses, both the amplitude and the mean of the ground heat flux decrease (Figure 7.1 and 7.2).

During the entire simulation period, the cumulative net shortwave and longwave radiation, ground heat, sensible heat and latent heat fluxes are, respectively, 515, -213, 70, 110 and 122 MJ m^{-2}, i.e. 14.3, -5.9, 1.9, 3.1 and 3.4 MJ m^{-2} d^{-1} (Figure 7.3). Further, the percentages of ground heat flux, net longwave radiation, sensible and latent heat on the net shortwave radiation are, respectively, 13%, 42%, 21% and 24%. Compared to the sensible and latent heat transfer, the cumulative ground heat flux increases considerably in the first phase (before May 14), and increases at a reduced rate in the remaining time.

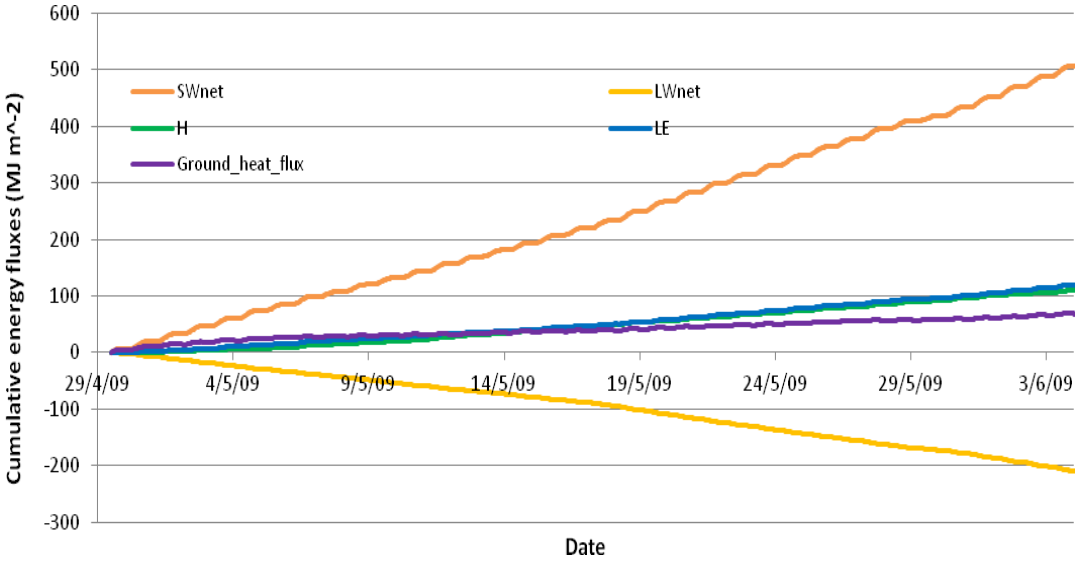

Figure 7.3 Cumulative energy fluxes in the study period (net shortwave and longwave radiation, ground heat, sensible and latent heat)

7.1.2 Ground Heat Flux and Soil Thaw

The ground heat flux, Q_g, is dissipated as three components, according to Equation 7.2:

$$Q_g = Q_s + Q_p + Q_i \quad [7.2]$$

where Q_s is the energy used to warm the active layer (W m^{-2}), Q_p is the energy used to warm the permafrost (W m^{-2}), and Q_i is the energy used to melt ice in the active layer (W m^{-2}). Among them, Q_p is consumed to rise the permafrost temperature with the soil below frost table remaining frozen. In the organic soil layer, the energy consumed in the active layer (Q_i + Q_s) covers the most ground heat flux (Quinton, 2005), and the quantity of the energy to thaw the soil ice, (Q_i) is much higher than the sensible heat of the soil (Q_s).

The upper surface of the frozen, saturated zone (i.e. frost table) begins to descend when the ground temperature exceeds the freezing point. The energy required to thaw the frozen soil is transferred from the ground surface to the frost table primarily by thermal conduction, although non-conductive processes such as infiltration may contribute appreciably in cases where open thermal contract cracks exist [Kane et al, 2001]. However, the cracks were not observed at the AOI. Further, according to Fourier's law, the ground surface temperature plays an important role in determining the thickness of the active layer.

Figure 7.4 indicates the daily average ground temperature variation and the cumulative ground temperature. On April 30, 2009 when the cell started to thaw, the ground temperature reached 8 ^oC. Similarly, as with the fluctuation of daily ground heat flux, the ground surface temperature varied from the lowest value of 3 ^oC on May 13 to the highest value of 22 ^oC on June 3. In the whole simulation from April 29 to June 4, the cumulative ground surface temperature totaled 340 ^oC. The average daily ground surface temperature was 9.5 ^oC during the soil thaw period.

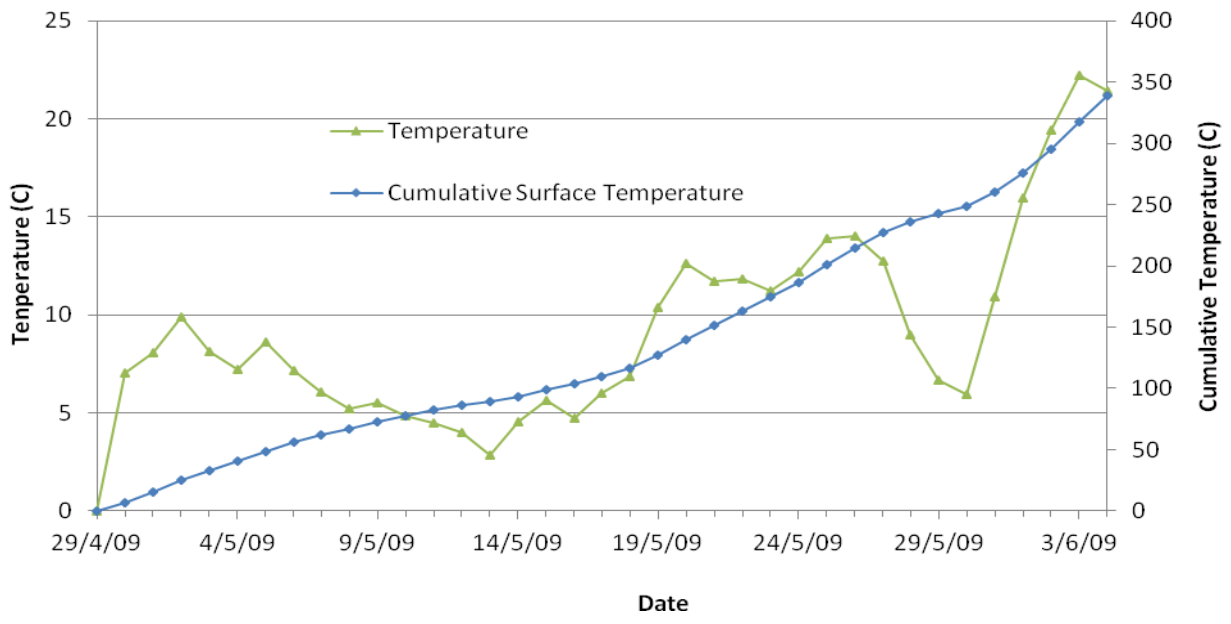

Figure 7.4 Average daily ground temperature and cumulative ground temperature

There appears to be no correlation between the simulated half hour surface temperature and the air temperature, but the daily ground surface temperature and air temperature are closely related (Figure 7.5). After calculation, the daily average ground surface temperature is 4.3 ^{o}C higher than the air temperature.

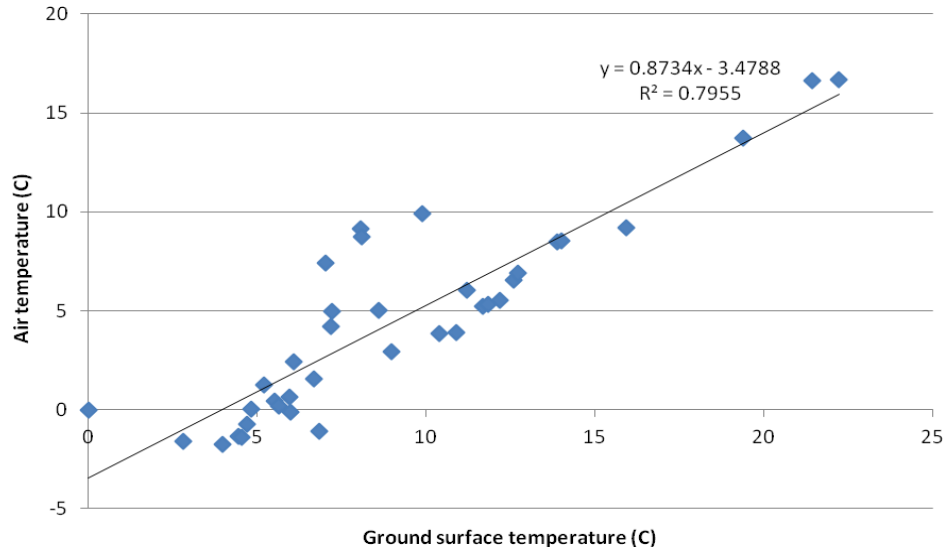

Figure 7.5 Relationship between air temperature and ground surface temperature

The temperature-index method derived from the Stefan equation [Hayashi, 2007] to estimate the thaw depth is commonly expressed in Equation 7.3:

$$z = \beta \cdot DDT^{1/2} \qquad [7.3]$$

where β is an empirical factor and DDT is the degree-day sum of temperature over the thawing period. Figure 7.6 shows the regression equations of frost table depth to cumulative air temperature and to ground surface temperature. The graph indicates that the power function works well on the correlation of frost table depth and cumulative temperature, as the regression coefficient of ground surface temperature is approximately 0.96, and 0.92 for air temperature.

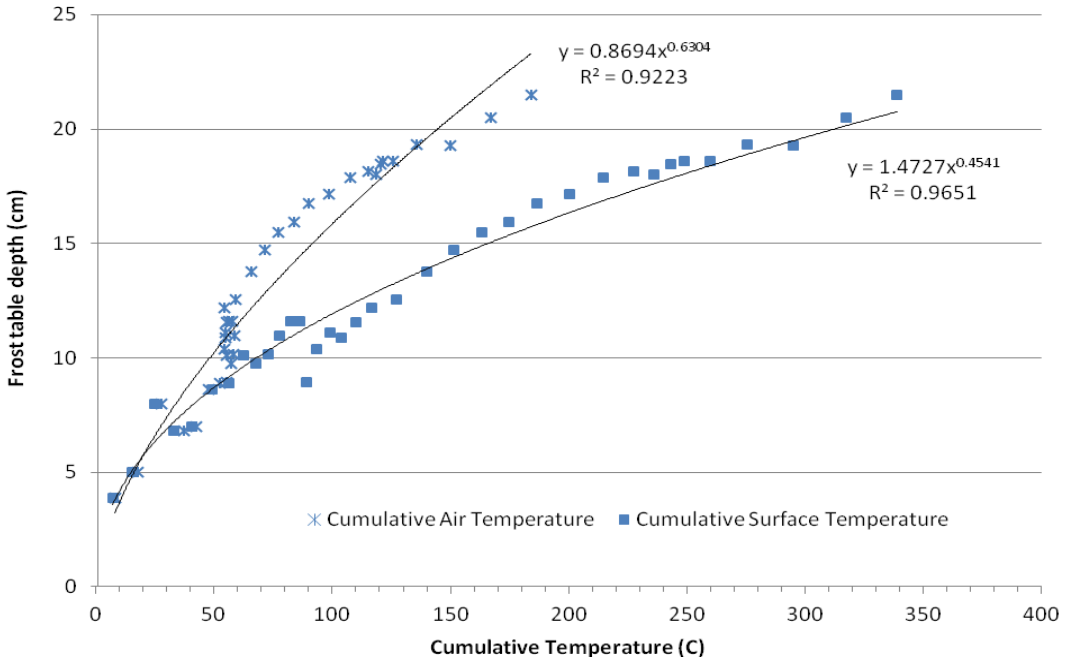

Figure 7.6 Relation of frost table depth and cumulative air and surface temperature

7.2 Soil Thaw and Moisture

7.2.1 Patterns of Soil Thaw and Moisture

Temporal variations in thaw depth were examined at 44 reference points within the AOI (Figure 3.3). As snowmelt progressed and the snow-free area expanded, transect points became snow-free and were added to the thaw depth measurement points. As the thaw season progressed (Figure 7.7), the additions of points are indicated by the shallowest frost depths. Compared to the variation of the shallowest frost table, the deepest frost table rose continuously to over 31 cm on the final thaw day (June 4, 2009).

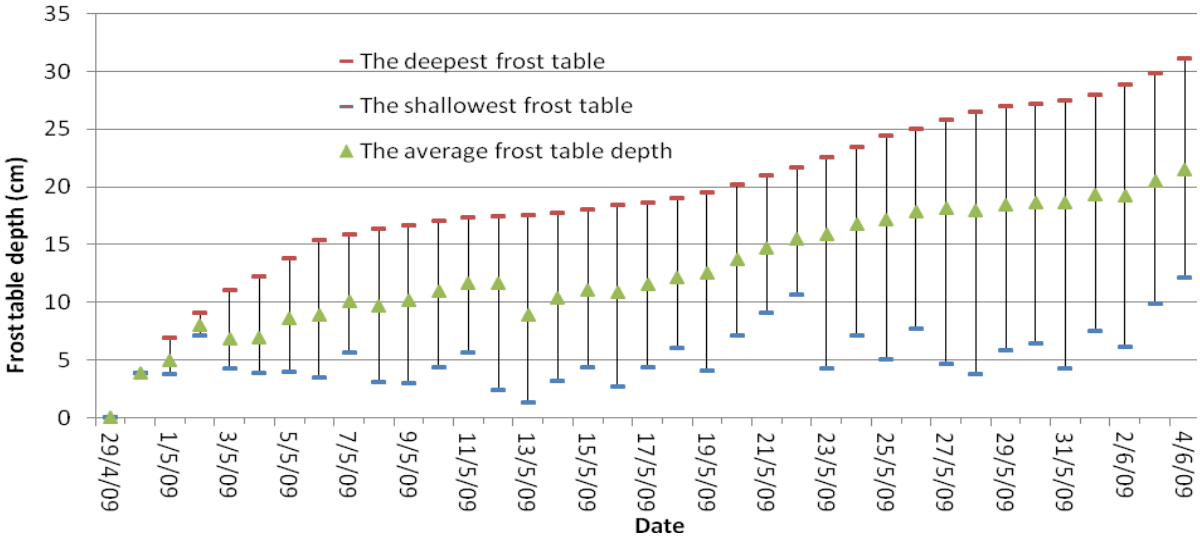

Figure 7.7 The deepest, shallowest and average frost table depth for the snow-free transect points over the study period

The average thaw depth of these reference points increased to 5 cm on May 1, 10 cm on May 7, 15 cm on May 21, and 20 cm on June 3, 2009. The rate of soil thaw decreased as the frost table deepened partly because, as soil thaw progresses, the distance between the ground surface and the zero-degree isotherm increases, which results in a decrease in the thermal gradient. When the frost table depth exceeded 10 cm, 15 days was needed for each additional 5 cm of thaw.

To investigate the importance of heat advection, the simulation is also done in the scenario that there is no lateral flow into the AOI from the upslope snowdrift. Compared to Figure 7.7, the difference of the average frost table depth is 3 cm on the final day of June 4 in Figure 7.8, respectively 22 cm and 25 cm with and without lateral flow. Remarkably, the rate of soil thaw is faster with the lateral flow than without lateral flow before May 13 when the average frost table depth is only 9.0 cm. It is indicated that the additional liquid water can facilitate soil thaw when the thaw depth is shallow. However, after May 20 when the frost table depth is over 15 cm, the lateral flow plays a role of decelerating the soil thaw.

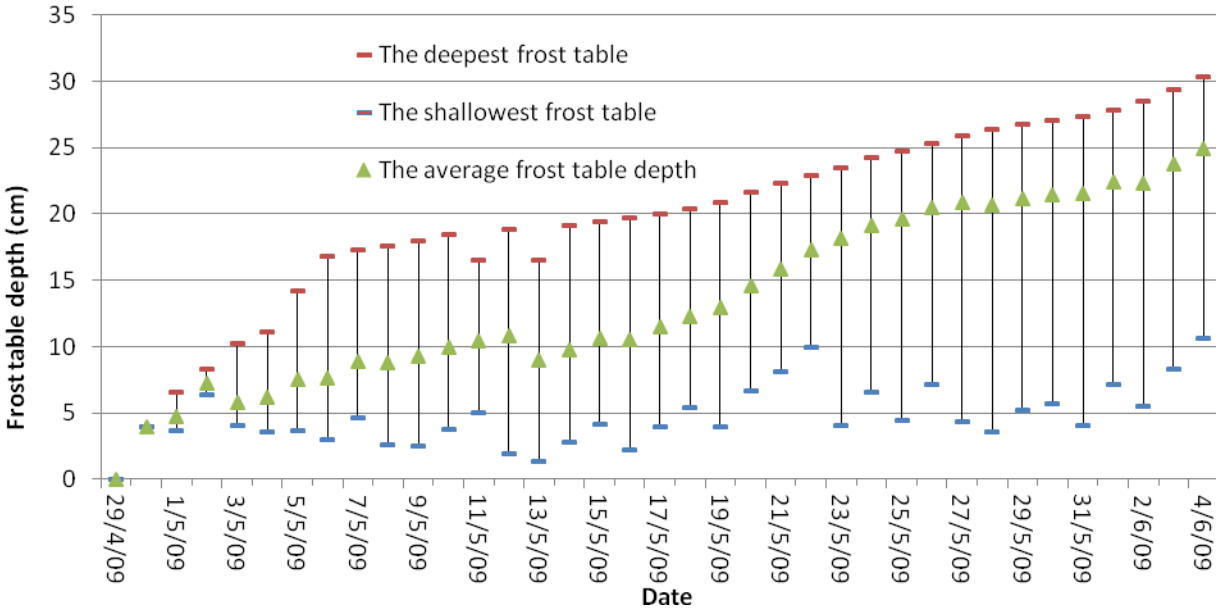

Figure 7.8 The deepest, shallowest and average frost table depth for the snow-free transect points without lateral flow over the study period

During the snowmelt season, the integrated liquid moisture of all soil layers from the ground surface to the frost table at the reference points varies from nearly saturation (93%) to the unfrozen liquid moisture content (20%). On April 29, 2009, the liquid moisture maintains 20% for all the points are frozen. Similar to the dramatic variation of shallowest frost table depth, the highest soil moisture is dynamic with a value of over 70% except for the first two days (Figure 7.8). After June 1, 2009, when all the points are

unfrozen, the lowest moisture is close to 40%. In the same period, the average moisture increases from 20% to 55%.

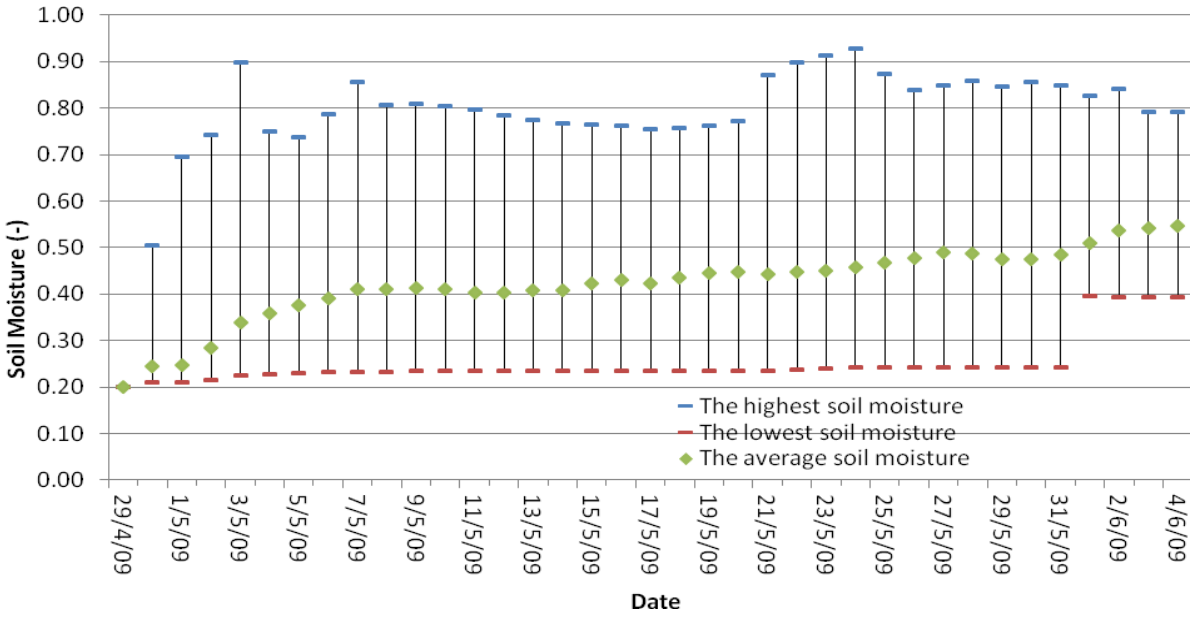

Figure 7.9 The simulated highest, lowest and average soil moisture perched by the frost table during soil thaw

7.2.2 Influence of Soil Moisture on Soil Thaw

During the process of soil thaw, the relative importance of the ground heat flux is influenced by the thermal diffusivity ($m^2\ s^{-1}$) of the soil, which is the ratio of thermal conductivity to heat capacity. In the frozen and saturated condition where the thermal diffusivity of soil is high, the ground heat flux moves rapidly through because the soil conducts heat quickly relative to its volumetric heat capacity. As ground ice is replaced by water and water is replaced by air though evaporation or drainage losses, the thermal diffusivity declines. For the top layer of the organic soil, the thermal diffusivity drops rapidly as the ice melts. However afterwards, its value stabilizes and does not respond readily to changes in soil moisture [Carey, 1998].

Below the freezing point, the liquid soil moisture content remains stable although it is dependent on the soil temperature as indicated in Equation 5.22. As soil thaw progresses, the liquid moisture content increases with the ice changing into the water. According to GEOtop Modelling, the integrated liquid moisture content above the frost table increases with thaw depth within the AOI. The average daily liquid moisture content of the reference points is positively correlated with the frost table depth for the study period between April 29 and June 3, 2009 (Figure 7.10). This relationship can be described by the logarithm function (R^2=0.91):

$$Moisture = 0.1643 \times \ln(FT) + 0.0165 \quad [7.4]$$

where Moisture is the liquid moisture content and FT is the frost table depth in cm.

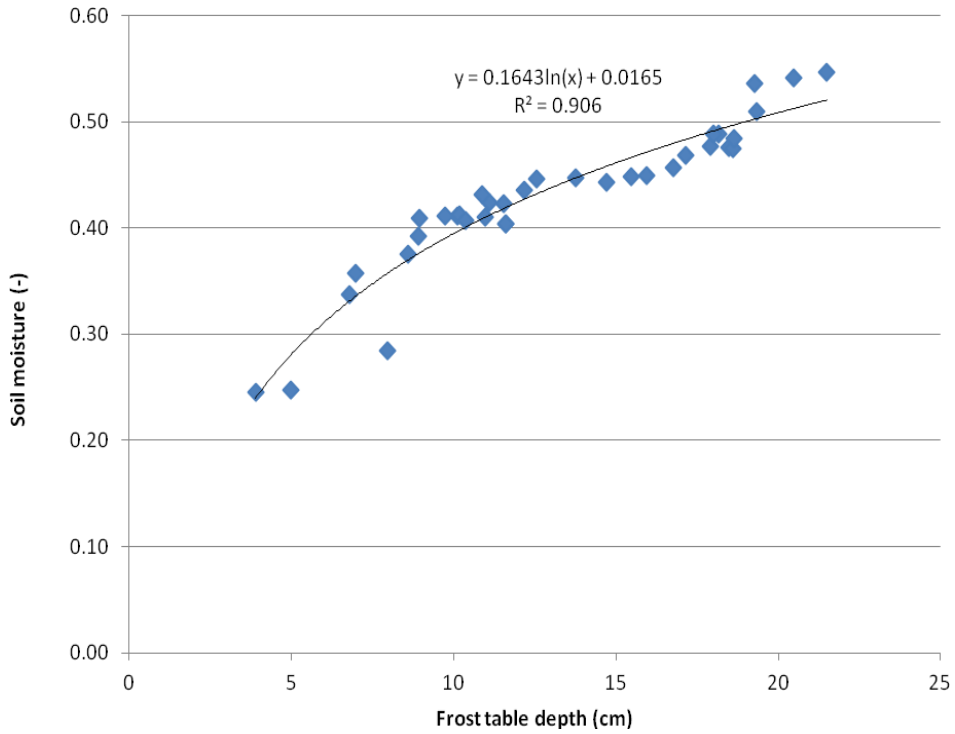

Figure 7.10 Relation of frost table depth and integrated liquid moisture of soil column

During the period of soil thaw, the increases of both frost table depth and liquid moisture content are caused by the ground heat flux. In the prospect of energy, the frost table depth only depends on ground heat flux, but the liquid moisture content is determined by both ground heat flux and latent heat transfer. Due to a decrease in both the thermal diffusivity and temperature gradient as soil thaw progressed during the 2009 spring, the magnitude of ground heat flux declined. Simultaneously, as the ice changes to water, the latent heat transfer intensifies with more water available for evapo-transpiration. Therefore, the evapo-transpiration plays an increasingly important role when the frozen soil becomes wet. Conclusively, Equation 7.4 represents the correlation of frost table depth and liquid moisture content in the period of soil thaw when the average frost table is less than 25cm.

May 6, 2009

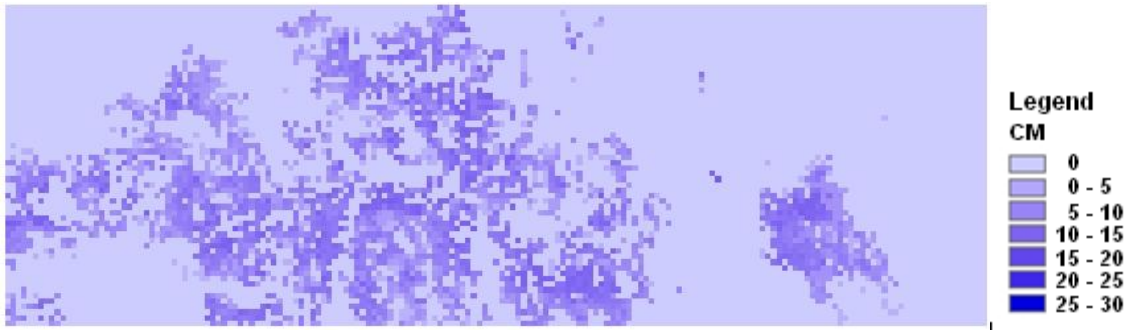

A

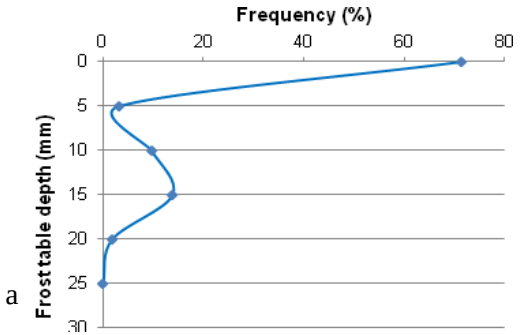

a

May 13, 2009

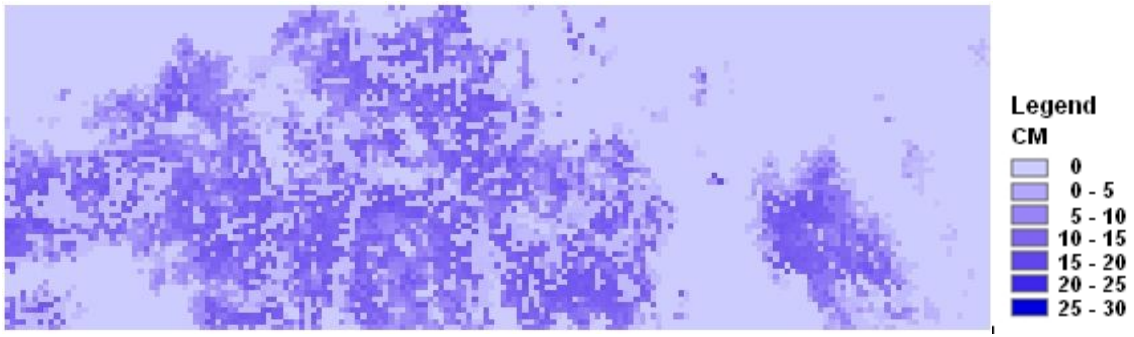

B

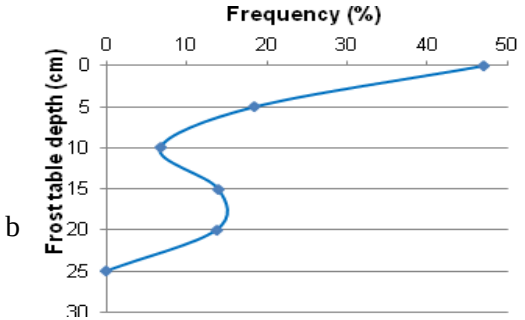

b

May 20, 2009

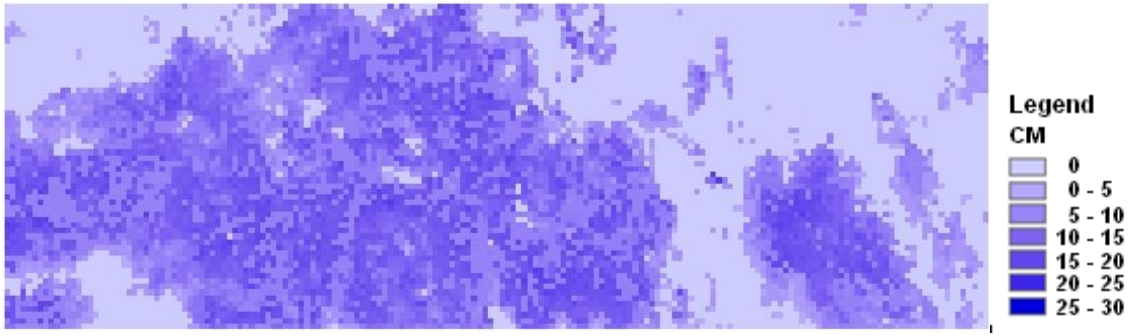

C

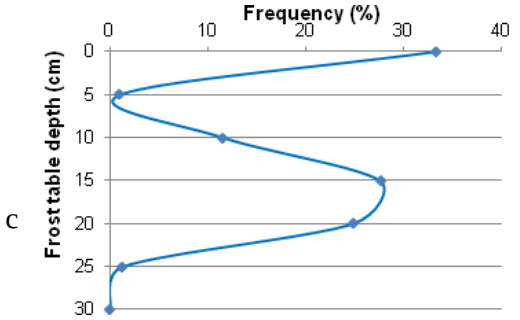

c

May 27, 2009

D

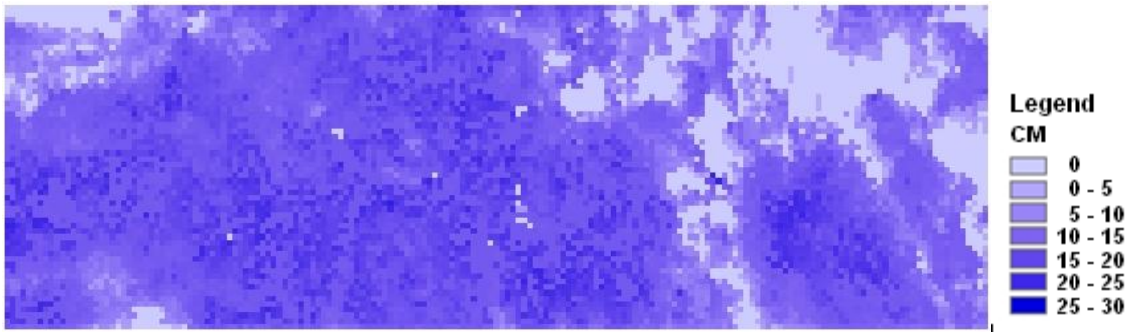

d

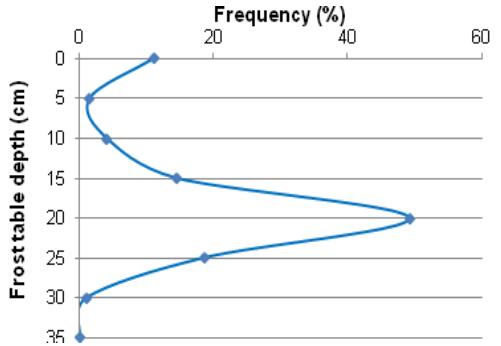

June 3, 2009

E

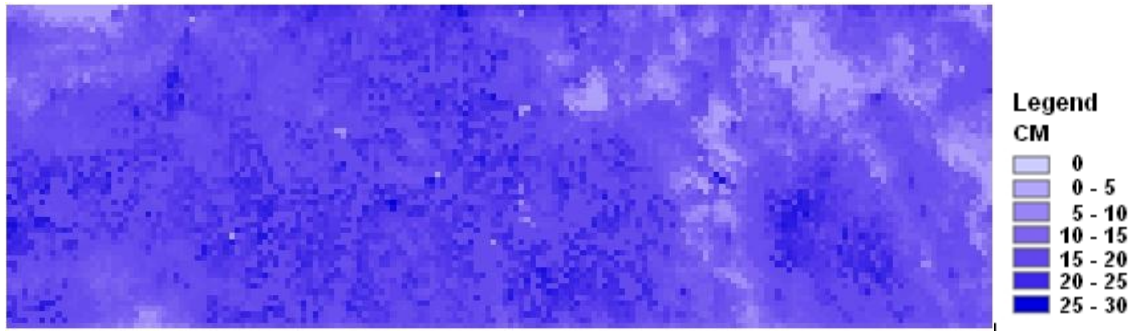

e

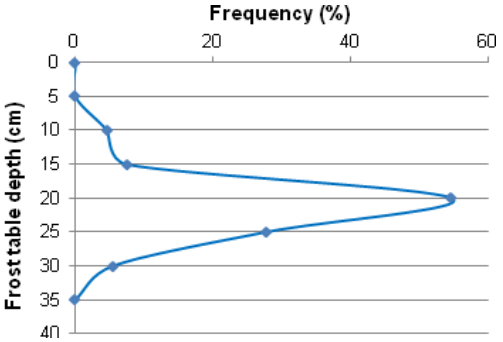

Figure 7.11 Frost table map A on May 6, B on May 13, C on May 20, D on May 27 and E on June 3,2009; frost table depth frequency distribution curve a on May 6, b on May 13, c on May 20, d on May 27 and e on June 3,2009

In addition to the characters of the frost table depth and the liquid moisture content at points within the AOI cell, the spatial patterns of the frost table and soil liquid moisture are also interesting. Figure 7.10 shows the spatial distribution of the frost table depth on five days (May 6, 13, 20, 27 and June 3, 2009) with 7 days interval. In the process of soil thaw, the central frequencies of the frost table depth shift from two peaks to one as the frozen soil area became progressively less. That is, two frost table depth peaks are 0 and 15 cm on May 6 and 0 and 15 - 20 cm on May 13 and 20. In contrast, on May 27 and June 3, only one peak occurs at a depth of 20 cm. The frequency of the central frost table depth increases stably with time and the frequency distribution approximates a normal distribution.

Compared to the frequency distribution of the frost table depth, the frequency of soil liquid moisture content was scattered in a wide range of moisture content between 20% and 50% when the frost table depth was between 5 cm and 20 cm on May 6, 2009 (Figure 7.10 a; Figure 7.11a). After May 27 when the 50^{th} percentile of the frost table depth fell to 20 cm, the central soil moisture content increases to 0.4 between May 27 and June 3. The frequencies of the soil liquid moisture content at 0.5, 0.6 and 0.7, increased to the highest value on June 3, which contribute to enlarge the water capacity of the AOI.

May 6, 2009

A

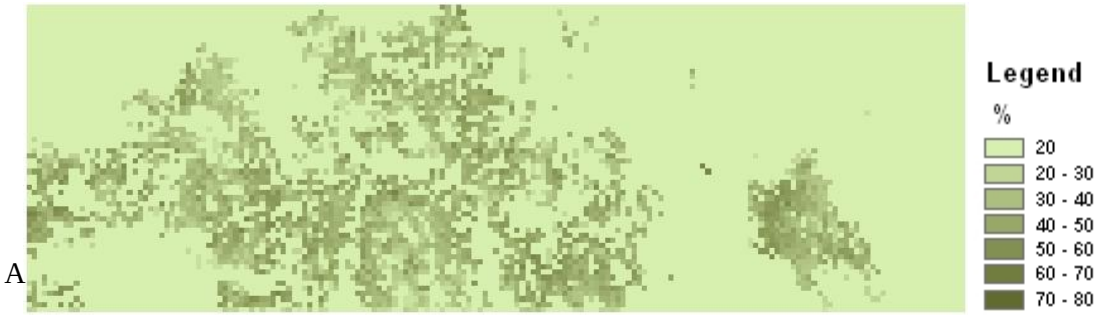

a

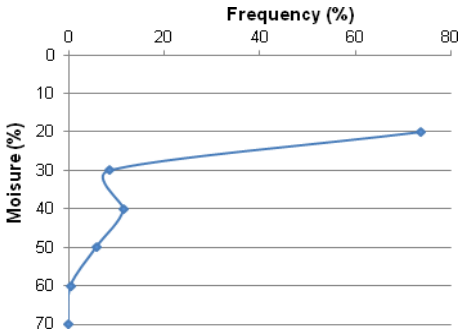

May 13, 2009

B

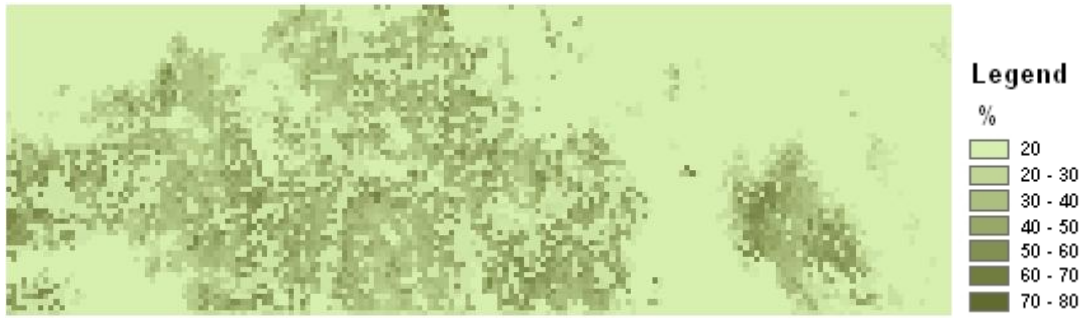

b

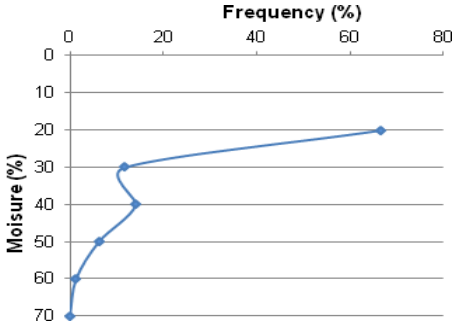

May 20, 2009

C

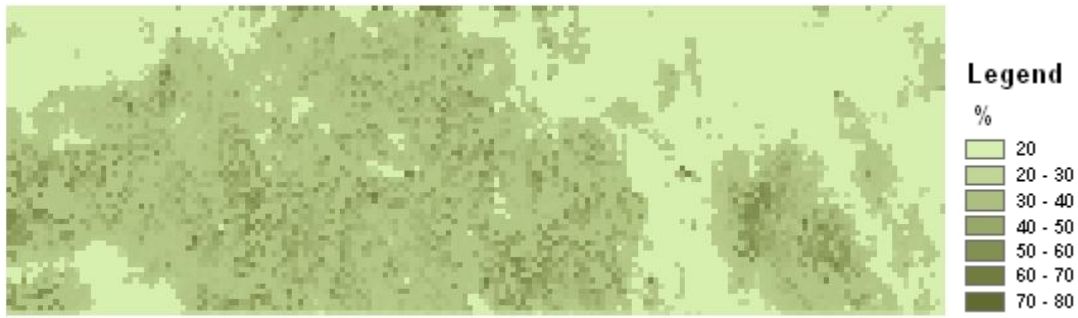

c

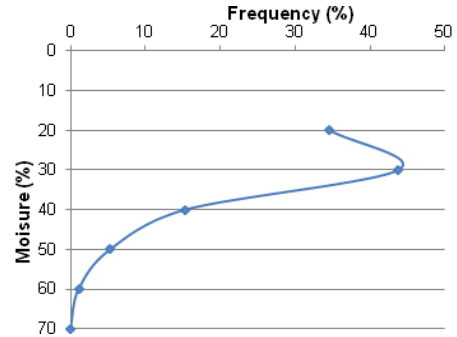

May 27, 2009

D

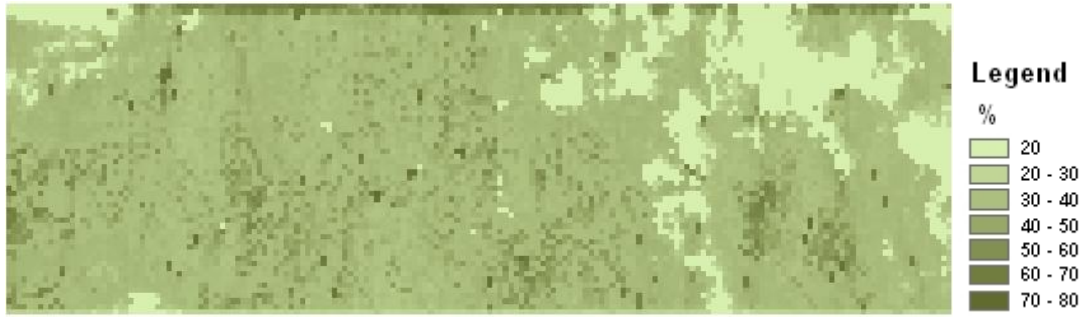

d

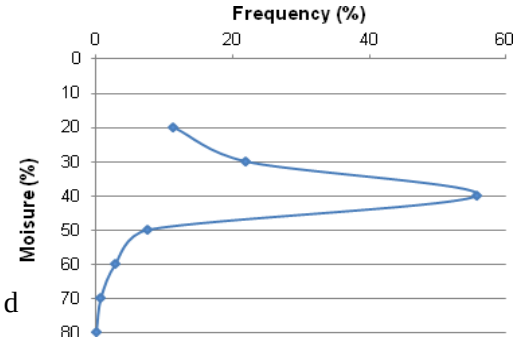

June 3, 2009

E

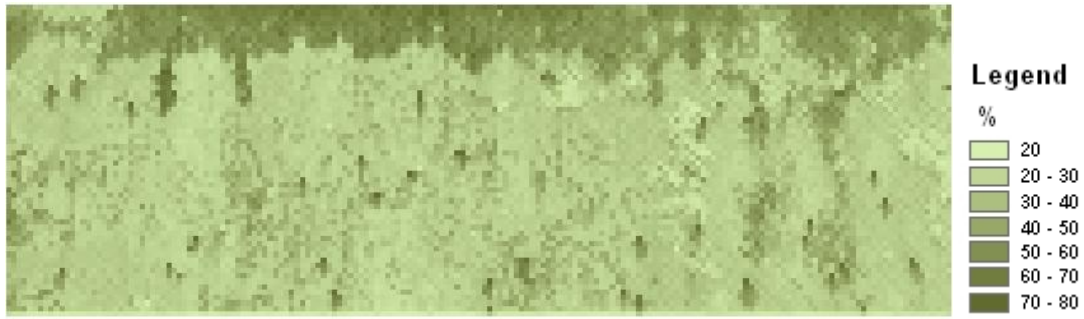

e

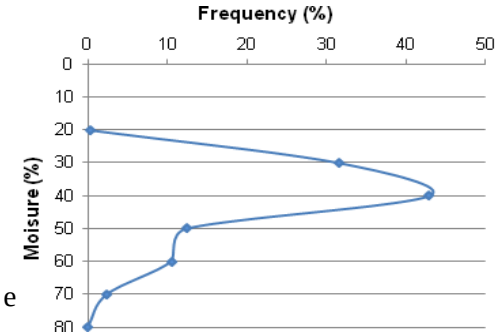

Figure 7.12 Soil liquid moisture content map A on May 6, B on May 13, C on May 20, D on May 27 and E on June 3,2009; soil liquid moisture frequency distribution curve a on May 6, b on May 13, c on May 20, d on May 27 and e on June 3,2009

7.3 Transit Time of the AOI

The spatial pattern of snow cover removal (Figure 3.3) reflects the pattern of soil thaw (Figure 7.10). On average, 85% of the AOI is snow covered between April 30 and May 6, which indicates that subsurface flow is present on only 15% of the AOI with the average soil thaw depth of 9 cm (Figure 7.12). At that time, the snow free patches were distributed widely throughout the AOI. As a result, the subsurface water conveyance to the valley bottom is ineffectual. For each of the following four weeks, the subsurface flow zone expanded to respectively 37%, 59%, 80% and 94% of the AOI with maximum soil thaw depth less than 35 cm. As the snow free patches expanded and coalesced, the subsurface flow gradually became more effective. To determine the subsurface flow, the important factors comprise of hydraulic conductivity of the soil and tortuosity of the snow free patches in the AOI.

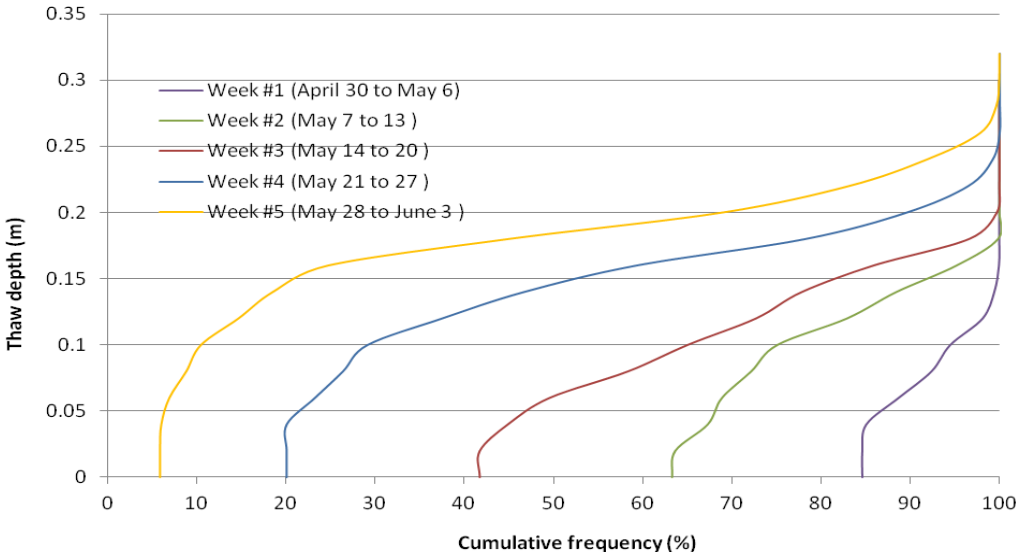

Figure 7.13 Cumulative frequency of weekly average thaw depth

7.3.1 Hydraulic Conductivity of the AOI

The saturated soil layer descends during soil thaw as the relatively impermeable frost table lowers through the active layer. Since the saturated flow is superior to the unsaturated flow in the magnitude, the water flow is mainly determined by the hydraulic conductivity at the frost table. With the expansion of snow free patches, the shallow thaw depth cells will have a higher hydraulic conductivity. Therefore, the hydraulic conductivity of the AOI varies spatially and temporally.

In the model for the 5-week period, the hydraulic conductivity frequencies are produced according to the soil thaw depth frequency curve for all snow free cells of the AOI (Figure 7.13). Similar to the thaw depth, the hydraulic conductivity curve contains two peaks in the three week period (the first week between April 30 and May 6; the second week between May 7 and 13; the third week between May 14 and 20). Gradually the hydraulic conductivity decreases a low value with the high frequency.

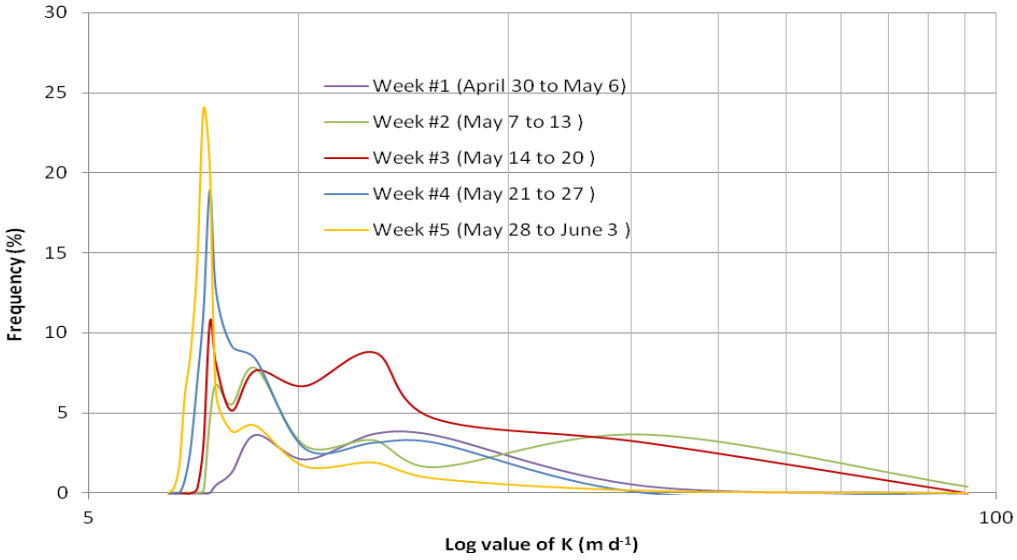

Figure 7.14 frequency distribution of log value of hydraulic conductivity

For the entire AOI, it is difficult and unnecessary to calculate precisely the hydraulic conductivity of each cell. Nevertheless, the daily average hydraulic conductivity can be estimated based on the snow

free area and frost table depth. This spatially representative hydraulic conductivity, k_f, is determined using Equation 7.5:

$$K_f = \sum f_i \cdot K_{FT}^i \qquad [7.5]$$

where f_i is the *i*-th fraction of the area of the thaw depth *i* to the area of the AOI, K_{FT}^i (m d^{-1}) is the hydraulic conductivity at the thaw depth *i*. After the calculation, the spatial representative hydraulic conductivity, K_f, is 17.1 m d^{-1} on April 30, and decreases gradually in the study period (Figure 7.15). A peak value of spatial representative hydraulic conductivity of 17.7 m d^{-1} occurs on May 13, 2009.

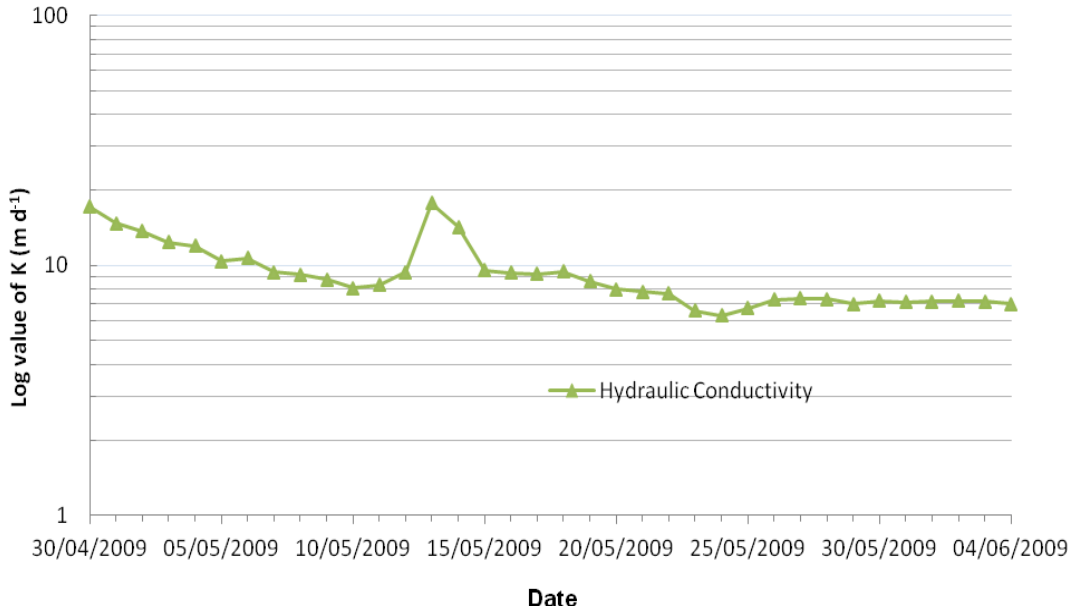

Figure 7.15 Spatial representative hydraulic conductivity

7.3.2 Transit Time of the AOI

Figure 7.15 illustrates the development of the spatially averaged tortuosity and transit time of the AOI during the study period. The tortuosity is calculated using Equation 3.1, and the transit time of the AOI, T_{AOI}, is calculated using Equation 7.6:

$$T_{AOI} = \frac{L_s \cdot T_x}{K_f \cdot \sin\alpha} \qquad [7.6]$$

where L_s is the straight-line distance between the upper and lower edges of the AOI (L_s = 60 m), T_x is the tortuosity, K_f is the spatially representative hydraulic conductivity (m d^{-1}), and sin (α) accounts for the slope (α = 18°) effect on the subsurface flow.

Since the aggregation of snow free patches increases connectivity in the subsurface flow zone, the average daily tortuosity exhibits a general decreasing trend during the thawing period. Hence, the high connectivity of the snow free cells and the high spatial representative K_f of the AOI, cause the minimum transit time of 11.8 days through the AOI on 13 May (Figure 7.16). Before May 13, the diagram of the transit time indicates that subsurface flow is restricted within the AOI with the maximum value of 33.5 days. After this time, the transit time fluctuates between 20 and 30 days.

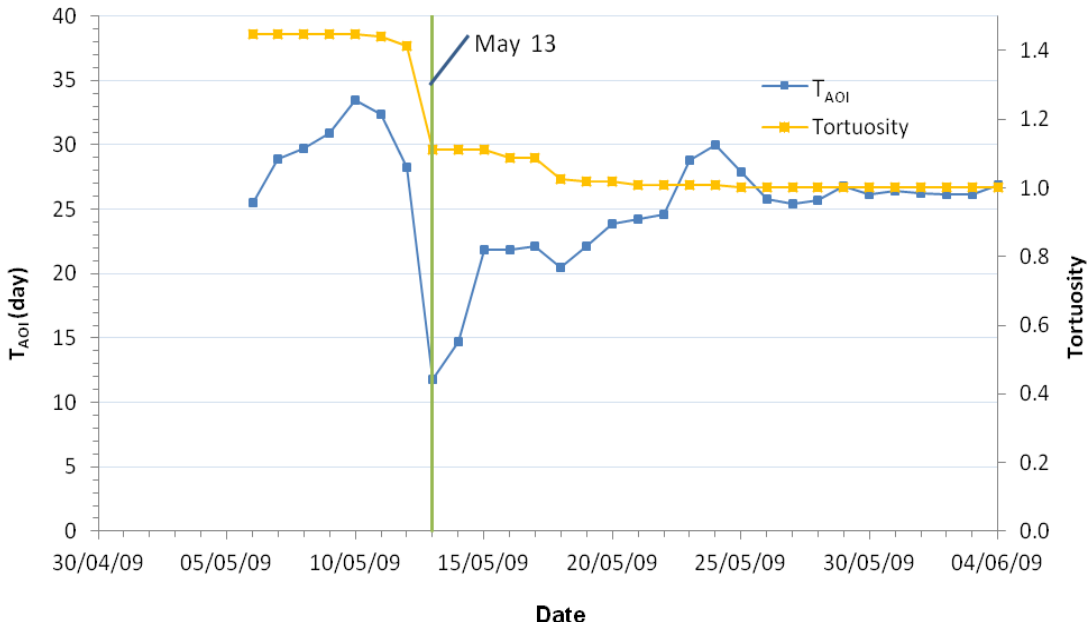

Figure 7.16 Tortuosity and transit time of AOI in the study period

7.4 Preferential Flow Path of the AOI

The runoff from the snowdrift upslope of the AOI reaches the stream at the base of the slope via various paths that affect both the timing and magnitude of the snowmelt runoff. Further, the pattern of hillslope drainage depends on the preferential flow paths and the total contributing area of the runoff. Both the preferential flow paths and the contributing area are influenced spatially and temporally by the frost table topography. The approach to delineating the preferential flow paths on the frost table topography is indicated in Figure 7.16, which contains the representative snow free and snow covered areas.

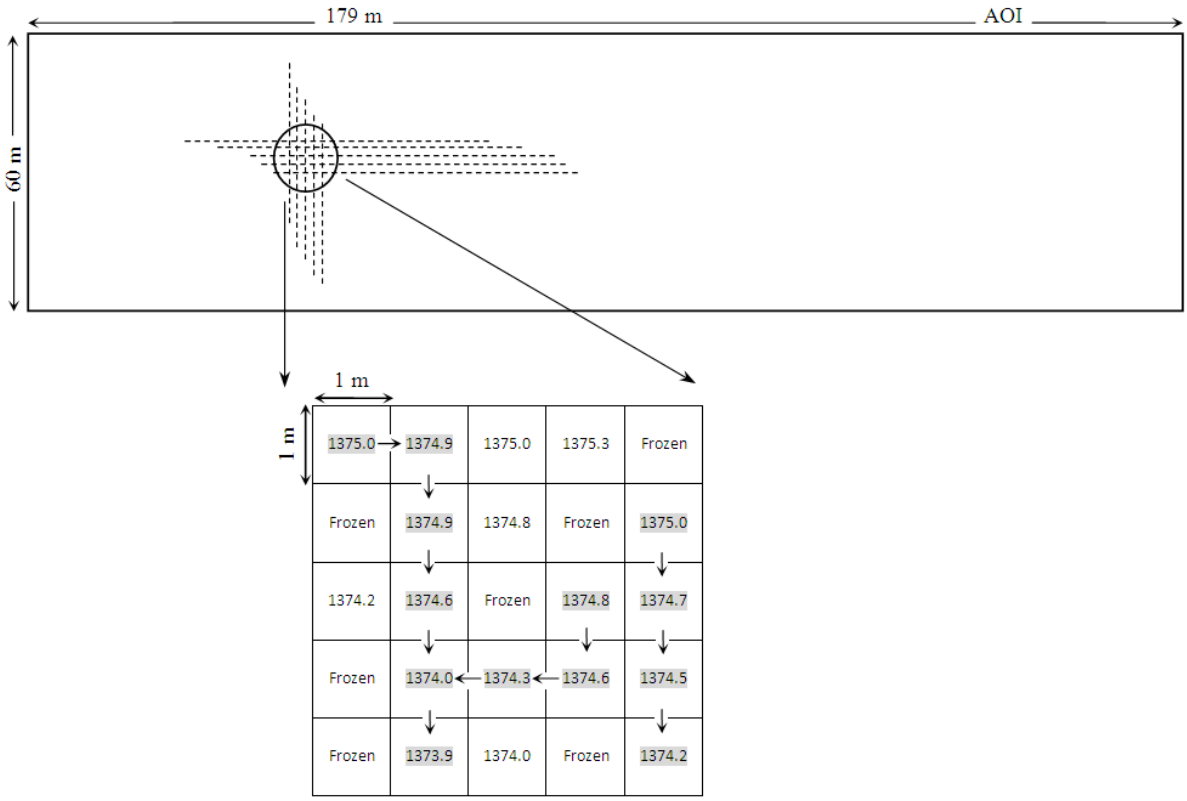

Figure 7.17 Schematic diagram of the flow paths on the frost table topography

The frost table topography is produced by subtracting ground surface elevation (i.e. DEM) from the frost table depth calculated in GEOtop, and the elevation values of the frozen cells are set null to represent impermeability. The preferential flow is assumed to follow the steepest slope involving the 8 adjacent cells on the frost table topography. As well, the water table surface is assumed to be parallel to the frost table slope. The model of preferential flow path is indicated in Figure 7.17, and the detailed formulas applied in the model are shown in Appendix B.

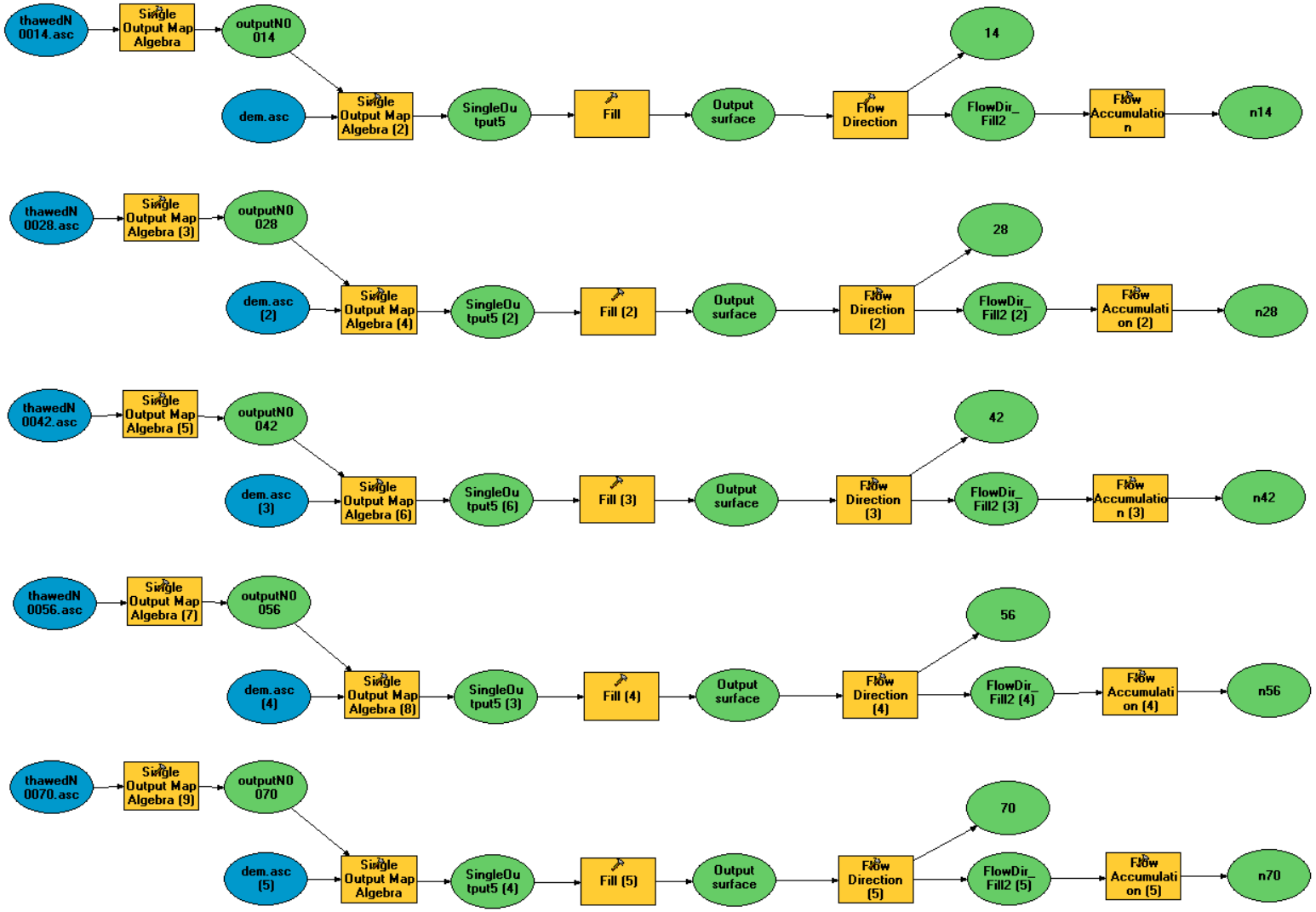

Figure 7.18 Model of preferential flow path on the frost table topography

The contributing area of the runoff refers to the total number of connected snow free cells that drain runoff from the AOI. The total contributing area consists of every single flow path within the AOI. After a snow free patch appears, the flow path is dynamic, but the total contributing area increases gradually as soil thaw promotes the connection of snow free cells.

Based on the frost table topography on May 6, 2009, there are some isolated snow free patches in the AOI, which indicates the impeded flow paths in the depressions (Figure 7.18). At this time, the drainage from the AOI by preferential flow was sparse because the flow paths in the snow free patches were disconnected. In the following time from May 13 to June 3, the quantity of flow paths increases with the enlarging snow free area. However, the superiority of the preferential flow is weakening as many flow paths emerge. When the snow cover is totally removed in the AOI on June 3, the flow paths delineated by the frost table topography are similar to that produced by the DEM.

May 6, 2009

A

May 13, 2009

B

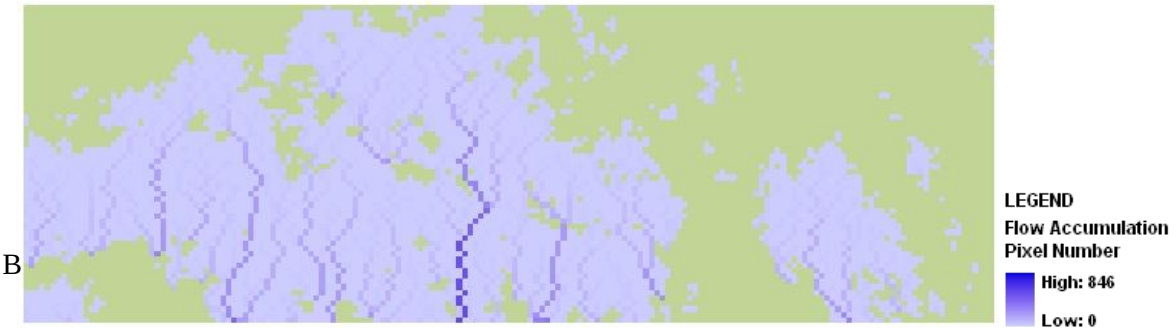

May 20, 2009

C

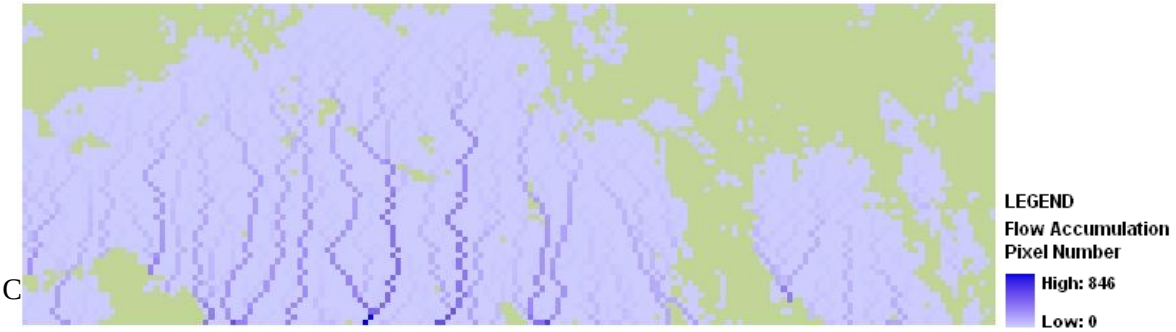

May 27, 2009

D

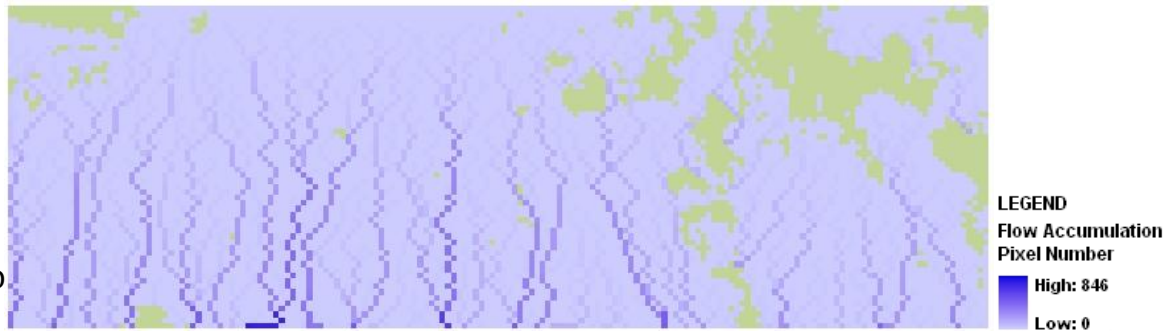

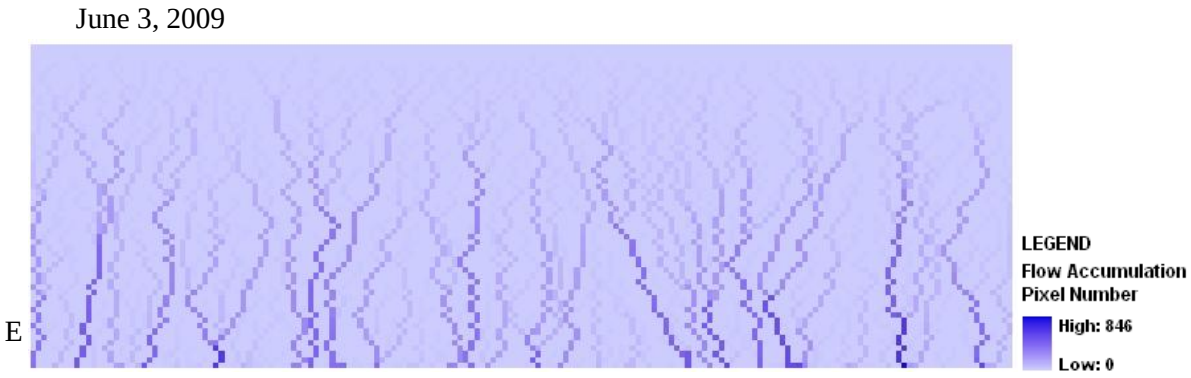

Figure 7.19 The flow paths of hillslope drainage based on the frost table topography

Table 7.1 shows the interrelation of the snow free area, total contributing area, and preferential flow path within the AOI. On May 6, 2009, the area of the largest preferential flow path was 96 m^2 (i.e. 96 cells) where 28 percent of the AOI was snow free. By May 20, 2009, the area of the largest preferential flow path increased to 832 m^2, and 69 percent of the snow free area was connected to discharge the runoff from the AOI. On June 3 when the snow free area reached 100%, the largest flow path conducted the water in an area of 650 m^2.

Table 7.1 The preferential flow path and contributing area on five days

date	Snow-free area (m^2)	Total Contributing area (m^2)	Five largest preferential flow path (m^2)					Percentage of five largest preferential flow path to total contributing area
			No. 1	No. 2	No. 3	No. 4	No. 5	
May 6	2909	611	96	82	72	46	34	54%
May 13	5404	2590	534	270	240	229	213	57%
May 20	6806	4689	832	514	353	319	288	49%
May 27	9117	7590	718	603	452	448	364	34%
June 3	10266	10266	650	632	540	477	474	27%

Similarly, as with the area of the single preferential flow path, the number of the preferential flow paths is also variable since the preferential flow in the AOI are influenced by the lowering of the frost

table. With increasing flow paths in the AOI, the importance of preferential flow on conducting the discharge gradually decreases. On May 6 and 13, the cumulative area of the five largest preferential flow paths comprises over half of the total contributing area. By contrast, on June 3, it makes up only 27% of the total area, which is indicated in Table 7.1.

Although the total contributing area and the number of flow paths increase during the soil thaw, the majority of the runoff drains from the AOI through only a small proportion of the flow paths (Figure 7.19). Between May 6 and June 3, some specific cells on the bottom of the AOI aggregate much more contributing area than the other cells. As indicated in the figure, One May 6, 2009, 15 percent of the hillslope width drains approximately three-fourths of the total contributing area. The mean contributing area, which assembles the half total converging area, are 70 m^2, 210 m^2, 360 m^2, 360 m^2 and 420 m^2 on May 6, 13, 20, 27 and June 3, respectively.

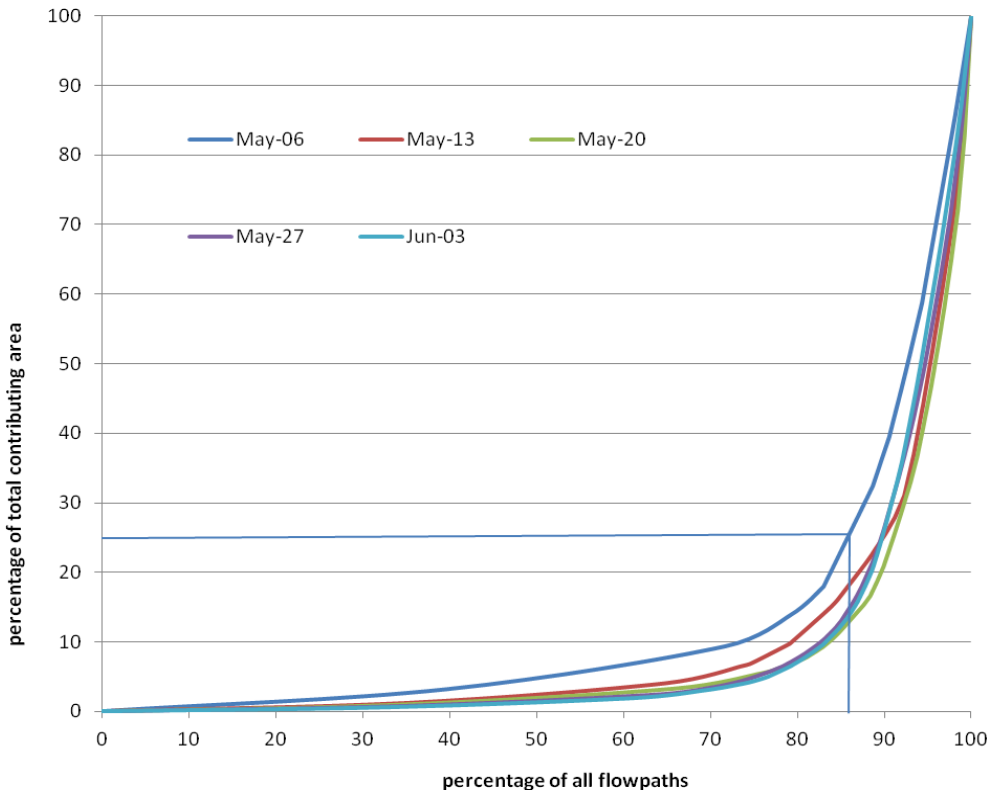

Figure 7.20 Relation of flow paths and contributing area on May 6, 13, 20, 27 and June 3, 2009

7.5 Discharge

The runoff represented in the GEOtop model results exclusively from the snowdrift upslope of the AOI and the content of water released in the active layer. Similar to the snowmelt percolation measured by lysimeter, the characteristics of the hillslope runoff hydrograph are dominated mainly by the energy processes (such as air temperature), not by precipitation. The runoff indicates an apparent diurnal trend in a daily cycle. According to the model, the shape of the snowmelt percolation and hillslope runoff hydrographs is close to the air temperature curve (Figure 7.20A). When the temperature is below zero, the runoff is nearly restrained between May 10 and 19.

In Figure 7.20 B and C, the comparison of the half-hourly hydrographs shows that the snow melt peak precedes the slope runoff by 8-10 hours before May 10. If the peak of snow melt is higher, the time lag between snow melt and slope runoff is shorter. For instance, on May 2, 2009, the peaks of snow melt and slope runoff are present at 16:00 and 24:00 hours, respectively. By contrast, between May 20 and 30, the time lag is only 5 hours or less and the appearances of snow melt and slope runoff peaks are between 13:00 to 16:00 hours, and between 14:00 to 20:30 hours, respectively. For instant, the peak of snow melt is at 13:30 hours and the peak of slope runoff is at 16:00 hours on May 26.

After May 30, the time lag between the snow melt percolation and slope runoff hydrographs is not apparent. Compared to snowmelt percolation, the shape of the slope runoff hydrograph has great difference. It can be seen in Figure 7.20 B and C that the rise and fall sections of the snow melt hydrograph are much steeper than the slope runoff, and the magnitude of the slope runoff peak collapses dramatically. The change may be influenced by the increasing thaw depth which entails an increasing water retention capacity of the soil.

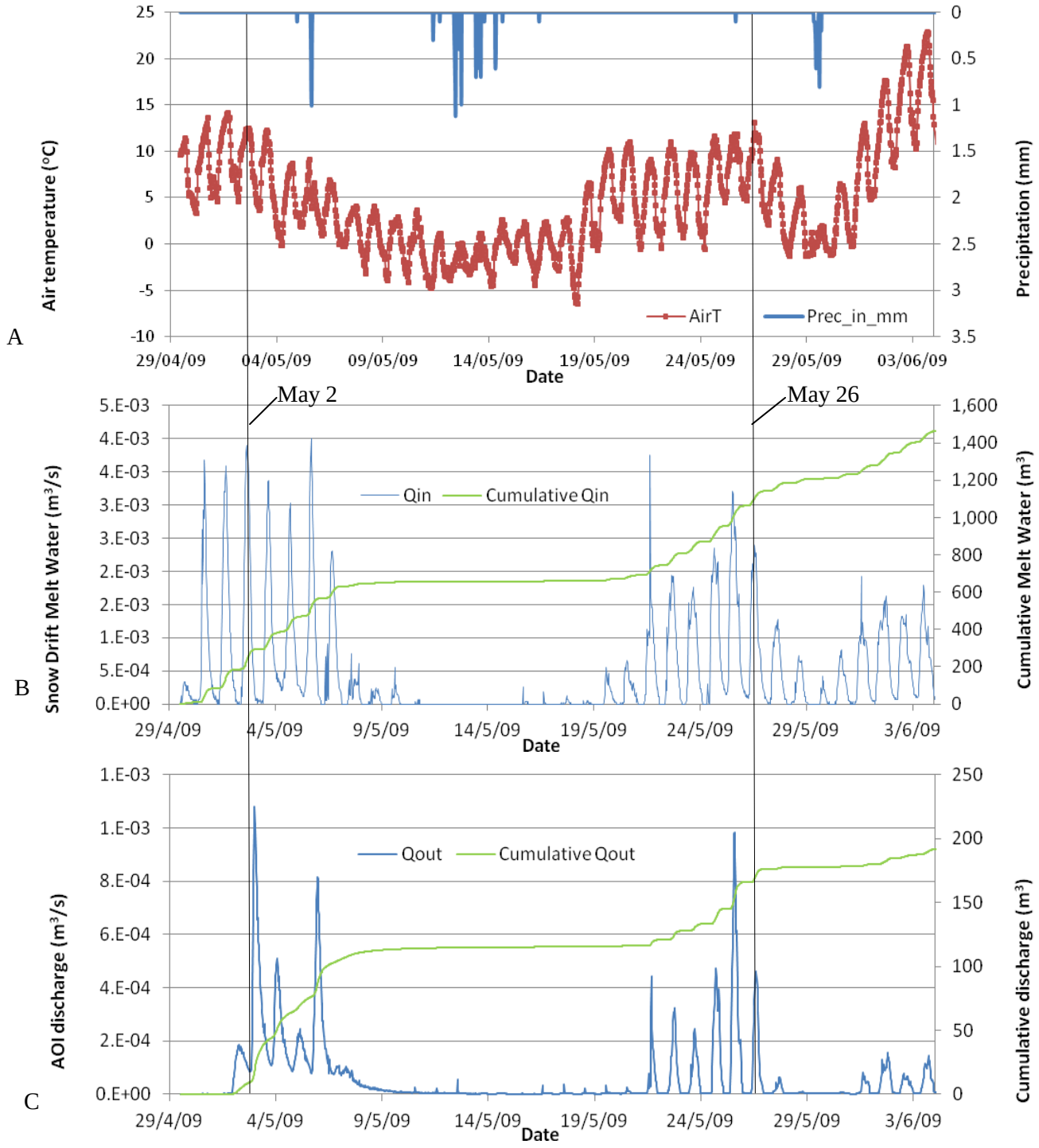
A
Air temperature (°C)
Precipitation (mm)
AirT
Prec_in_mm
Date
May 2
May 26
B
Snow Drift Melt Water (m³/s)
Cumulative Melt Water (m³)
Qin
Cumulative Qin
Date
C
AOI discharge (m³/s)
Cumulative discharge (m³)
Qout
Cumulative Qout
Date

D

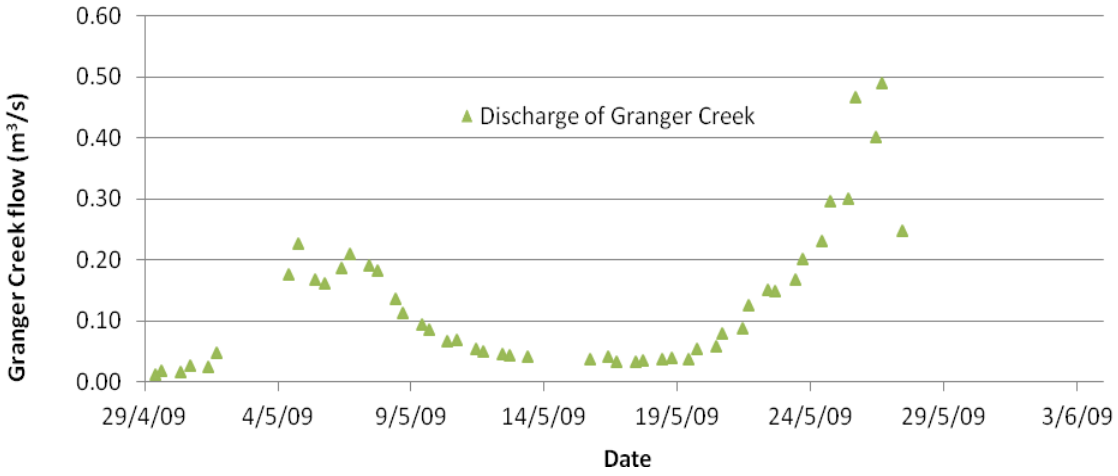

Figure 7.21 A: air temperature and precipitation; hydrographs of snow melt (B), AOI discharge (C), and stream flow of Granger Creek (D) from April 29 to June 4, 2009

Based on the simulation of snow melt percolation and discharge of the AOI, the ratio of the energy-based runoff is only 0.13. Cumulatively between April 28 and June 4, 1480 m^3 of snow melt water is changed to 190 m^3 of slope runoff. Especially, between May 18 and June 4, the cumulative snow melt water is approximately 800 m^3, which only produces 70 m^3 of runoff.

Hill slope runoff is assumed to be generated through two distinct flow systems: quick flow and slow flow. Quick flow is rapid runoff delivered downslope by the preferential flow in the highly porous organic material, and slow flow is laminar flow in the saturated matrices of soils that involve a low hydraulic conductivity. The shape of quick flow dominant hydrograph is characterized by a fast response and a short recession. As thaw depth increases on the slope, the water storage addition at the expense of runoff will promote the slow flow regime. As shown in the days between June 1 and 4, 2009, the characteristics of slow flow are apparent with the symptoms of a flat peak and extended recession. Compared to the slope runoff, the diurnal fluctuation of stream flow does not respond as strongly to the daily rhythm of melt. When the slope runoff is restrained at night, the stream flow keeps the baseflow of approximately 0.02 - 0.04 m^3/s.

Chapter 8

Conclusions

The variation of ground energy fluxes are investigated using a micro-scale hydrological model (1m × 1m in GEOtop). The cumulative ground surface temperature is a good indicator of the observed thaw depth. Depth-integrated soil moisture and the horizontal hydraulic conductivity of the saturated flow zone are examined in relation to the extent of ground thaw as indicated by the position of the impermeable frost table. When the impermeable frost table topography descends, the preferential flow paths and total runoff contributing area are defined with implications to hillslope drainage. The major findings of this study are as follows:

1. The diurnal features of vertical snowmelt percolation and horizontal slope drainage in the AOI are apparent, which are caused by energy fluxes. The time lag between the arrival at the base of the snowpack of meltwater percolate and its delivery to the base of the hillslope is 8 to 10 hours when the average frost table depth is between 0 and 10 cm. After the snow-free area expands to over 50% of the AOI, the delay time reduces to 5 hours or less when the average frost table is between 10 and 20 cm. At last, the peak of slope drainage hydrograph is dramatically cut down when the average frost table is over 20 cm.
2. The end-of-winter snow distribution dominates the spatial pattern of soil thaw. Heat conduction dominates the energy supply for soil thaw. By the final day of study (4 June) the average simulated thaw depths with and without snowpack meltwater are 22 cm and 25 cm, which indicates that the meltwater input decreases the thaw rate by ~13%. The average measured thaw depth by this date of the 44 measurement points is 22 cm. An indication that the conduction is the dominant heat transfer mechanism is strong correlation between cumulative daily air and surface temperature in Figure 7.6.

3. The average simulated soil moisture for the 44 transect points increases as snow melt and soil thaw progresses. In the melt season, the soil thaw and soil moisture is well correlated with the logarithmic function (see Equation 7.4) during the simulation period between April 29 and June 3, 2009.
4. Due to the increasing frost table depth and the decreasing hydraulic conductivity, the areally-weighted average hydraulic conductivity of snow-free cells in the AOI varies from 17.7 m d^{-1} to 6.3 m d^{-1} over the entire study period. Consequently, the transit time of the AOI is between 33.5 days and 11.7 days during the same time.
5. The preferential flow is important to the total contributing area before May 13 when the average frost table depth is approximately 10 cm. As the snow-free area is constantly increasing, the largest preferential path delineated by the frost table topography increases to the highest value of 832 m^2, and then descends to 650 m^2. When the snow-free area is approximately 50% of the AOI, the five largest preferential paths cover 57% of the total contributing area.

In this study, the energy-based runoff concept is evaluated within the AOI for single snowmelt-runoff season. The hydraulic properties of the soil, the flow paths (variable contributing areas) are examined based on the rate and patterns of the ground heat flux. The analysis of the frost table topography obtained by the micro-scale hydrological model is helpful to combine the effect of soil thaw in meso-scale or large scale hydrological models.

Appendix A

TDR and TB4 Program of CR 1000 Series Datalogger

```
'CR1000 Series Datalogger
'lysimeter of TB4 and snow moisture of TDR100 with 6 probes in 15 minute interval for Wolf Creek 2009
'program author: Qian Che

'Declare Public & Dim Variables -----------------------------------
Public batt_volt
Public Panel_temp
'For TDR100
Public LaL(6)
Public LaL2(6)
Public LedieuVWC(6)
Public ToppVWC(6)
Public Flag(2)
Public WavePT(260)
Public MuxChan
Dim I
'For Lysimeter
Public Lysimeter_mm
Units Lysimeter_mm=mm

'Declare Constants -------------------------------------------------
'Topp Equation Dielectric Constants
Const a0= -0.053
Const a1= 0.0292
Const a2= -0.00055
Const a3= 0.0000043
Const high = true
Const low = false

'Define Data Tables ------------------------------------------------
DataTable (Data_TDR,1,-1) '15-minute Data Table (i.e. TDR100 VWC Measurements)
    DataInterval (0,15,Min,10)
    Minimum (1,batt_volt,IEEE4,0,False)
    Average (1,Panel_temp,IEEE4,0)
    CardOut(0,-1000)
    Sample (6,LaL(),IEEE4)
    Sample (6,LedieuVWC(),FP2)
```

```
    Sample (6,ToppVWC(),FP2)
EndTable
DataTable (TDR_Wave,1,240) 'Data Table (i.e. Capture TDR Probe Waveforms)
    Sample (1,MuxChan,IEEE4)
    Sample (260,WavePT(),FP2)
EndTable
DataTable(Lysimeter_mm,True,-1)
    DataInterval(0,15,Min,0)
    CardOut(0,-1000)
    Totalize(1,Lysimeter_mm,IEEE4,0)
EndTable

'Main Program ------------------------------------------------
BeginProg
    SDMSpeed (50) 'Fix TDR100 to CR1K communication timing
    Scan (1,Sec,0,0) 'scan instructions every 1 sec
        Battery (Batt_volt)
        PanelTemp (Panel_temp,250)
'Set flag 1 High every 15 minutes (Note: User can manually set flag 1 high/low)
        If TimeIntoInterval(0,15,min) Then Flag(1)=High
'Set flag 2 High once per 2 hours (Note: User can manually set flag 2 high/low)
        If TimeIntoInterval(0,2,Hr) Then flag(2)=high '
        If Flag(1)=High Then  '************************************
            SW12 (1) 'Turn on 12V Power to TDR100 & SDMX50
'Note: Wire TDR100 & SDMX50 12V power leads to CR1000 SW12 Terminal
            Delay (1,2,Sec)   'pause 2 sec to allow power supply voltage to settle
'Measure La/L on SDMX50 channel #1 thru channel#8 & convert to VWC using Topp Eq.
            TDR100 (LaL(1),0,0,1001,4,1.0,251,16,5.0,0.3,0.085,1,0)
            TDR100 (LaL(2),0,0,2001,4,1.0,251,16,5.0,0.3,0.085,1,0)
            TDR100 (LaL(3),0,0,3001,4,1.0,251,16,5.0,0.3,0.085,1,0)
            TDR100 (LaL(4),0,0,4001,4,1.0,251,16,5.0,0.3,0.085,1,0)
            TDR100 (LaL(5),0,0,5001,4,1.0,251,16,5.0,0.3,0.085,1,0)
            TDR100 (LaL(6),0,0,6001,4,1.0,251,16,5.0,0.3,0.085,1,0)
            For I=1 To 6
                LaL2(I) = LaL(I)^2    'Apparent Dielectric Constant K = (La/L)^2
            Next I
'Topp Conversion from Dielectric Constant to Volumetric Water Content (VWC)
            For I=1 To 6
                ToppVWC(I)=a0 + a1*LaL2(I) + a2*LaL2(I)^2 + a3*LaL2(I)^3
            Next I
'Measure La/L on SDMX50 channel #1 thru channel#8 & convert to VWC using Ledieu Eq.
'Note: Reps (i.e. "1002") assume all cables are the same length!!!
            TDR100 (LedieuVWC(),0,0,1006,4,1.0,251,9.5,5.0,0.3,0.085,.1138,-0.1758)
```

```
            CallTable Data_TDR
            Flag(1)=0 'reset state of Flag 1
            SW12 (0 ) 'Switched 12V Low
        EndIf  'EndIf for Flag 1 **********************
        If Flag(2)=High Then  '************************************
            SW12 (1)    'Turn on 12V Power to TDR100 & SDMX50
            Delay (0,2,Sec)   'pause 2 sec to allow power supply voltage to settle out
            MuxChan=1001       'store the SDMX50 channel in variable "MuxChan"
            TDR100 (WavePT(),0,1,1001,4,1.0,251,9.5,5.0,0.3,0.085,1,0)
            CallTable TDR_Wave()
            MuxChan=2001 'store the SDMX50 channel in variable "MuxChan"
            TDR100 (WavePT(),0,1,2001,4,1.0,251,9.5,5.0,0.3,0.085,1,0)
            CallTable TDR_Wave()
            MuxChan=3001
            TDR100 (WavePT(),0,1,3001,4,1.0,251,9.5,5.0,0.3,0.085,1,0)
            CallTable TDR_Wave()
            MuxChan=4001
            TDR100 (WavePT(),0,1,4001,4,1.0,251,9.5,5.0,0.3,0.085,1,0)
            CallTable TDR_Wave()
            MuxChan=5001
            TDR100 (WavePT(),0,1,5001,4,1.0,251,9.5,5.0,0.3,0.085,1,0)
            CallTable TDR_Wave()
            MuxChan=6001
            TDR100 (WavePT(),0,1,6001,4,1.0,251,9.5,5.0,0.3,0.085,1,0)
            CallTable TDR_Wave()
            Flag(2)=0 'reset state of Flag 2
            SW12 (0 ) 'Switched 12V Low
        EndIf  'EndIf *******************************
        PortsConfig (&B00000111,&B00000000) 'configure SDM ports C1,C2,C3 as inputs
'TB4 Rain Gauge measurement Rain_mm:
        PulseCount(Lysimeter_mm,1,1,2,0,0.1,0)
'Call Data Tables and Store Data
        CallTable(Lysimeter_mm)
    NextScan
EndProg
```

Appendix B

VBScript of preferential flow on the frost table topography

```
' ---------------------------------------------------------------------------
' 12.vbs
' Created on: Mon Jul 23 2012 11:21:43 AM
'(generated by ArcGIS/ModelBuilder)
' ---------------------------------------------------------------------------

' Create the Geoprocessor object
set gp = WScript.CreateObject("esriGeoprocessing.GPDispatch.1")

' Check out any necessary licenses
gp.CheckOutExtension "spatial"

' Load required toolboxes...
gp.AddToolbox "C:/Program Files/ArcGIS/ArcToolbox/Toolboxes/Spatial Analyst Tools.tbx"

' Local variables...
outputN0014 = "C:\Documents and Settings\Bill Quinton\Local Settings\Temp\outputN0014"
thawedN0014_asc__2_ = "C:\GEOtop_new\validation\With lateral flow\table\thawedN0014.asc"
Output_surface_raster = "C:\Documents and Settings\Bill Quinton\Local Settings\Temp\Fill_SingleO1"
n14 = "C:\GEOtop_new\validation\With lateral flow\New Folder\n14"
dem_asc = "dem.asc"
SingleOutput5 = "C:\Documents and Settings\Bill Quinton\Local Settings\Temp\SingleOutput5"
FlowDir_Fill2 = "C:\Documents and Settings\Bill Quinton\Local Settings\Temp\FlowDir_Fill2"
v14 = "C:\GEOtop_new\validation\With lateral flow\New Folder\14"

outputN0028 = "C:\Documents and Settings\Bill Quinton\Local Settings\Temp\outputN0028"
```

```
thawedN0028_asc = "C:\GEOtop_new\validation\With lateral flow\table\thawedN0028.asc"
Output_surface_raster__2_ = "C:\Documents and Settings\Bill Quinton\Local Settings\Temp\Fill_SingleO1"
n28 = "C:\GEOtop_new\validation\With lateral flow\New Folder\n28"
dem_asc__2_ = "dem.asc"
SingleOutput5__2_ = "C:\Documents and Settings\Bill Quinton\Local Settings\Temp\SingleOutput5"
FlowDir_Fill2__2_ = "C:\Documents and Settings\Bill Quinton\Local Settings\Temp\FlowDir_Fill2"
v28 = "C:\GEOtop_new\validation\With lateral flow\New Folder\28"

outputN0042 = "C:\Documents and Settings\Bill Quinton\Local Settings\Temp\outputN0042"
thawedN0042_asc = "C:\GEOtop_new\validation\With lateral flow\table\thawedN0042.asc"
Output_surface_raster__3_ = "C:\Documents and Settings\Bill Quinton\Local Settings\Temp\Fill_SingleO1"
n42 = "C:\GEOtop_new\validation\With lateral flow\New Folder\n42"
dem_asc__3_ = "dem.asc"
SingleOutput5__6_ = "C:\Documents and Settings\Bill Quinton\Local Settings\Temp\SingleOutput5"
FlowDir_Fill2__3_ = "C:\Documents and Settings\Bill Quinton\Local Settings\Temp\FlowDir_Fill2"
v42 = "C:\GEOtop_new\validation\With lateral flow\New Folder\42"

outputN0056 = "C:\Documents and Settings\Bill Quinton\Local Settings\Temp\outputN0056"
thawedN0056_asc = "C:\GEOtop_new\validation\With lateral flow\table\thawedN0056.asc"
Output_surface_raster__4_ = "C:\Documents and Settings\Bill Quinton\Local Settings\Temp\Fill_SingleO1"
n56 = "C:\GEOtop_new\validation\With lateral flow\New Folder\n56"
dem_asc__4_ = "dem.asc"
SingleOutput5__3_ = "C:\Documents and Settings\Bill Quinton\Local Settings\Temp\SingleOutput5"
FlowDir_Fill2__4_ = "C:\Documents and Settings\Bill Quinton\Local Settings\Temp\FlowDir_Fill2"
v56 = "C:\GEOtop_new\validation\With lateral flow\New Folder\56"

outputN0070 = "C:\Documents and Settings\Bill Quinton\Local Settings\Temp\outputN0070"
thawedN0070_asc = "C:\GEOtop_new\validation\With lateral flow\table\thawedN0070.asc"
Output_surface_raster__5_ = "C:\Documents and Settings\Bill Quinton\Local Settings\Temp\Fill_SingleO1"
n70 = "C:\GEOtop_new\validation\With lateral flow\New Folder\n70"
dem_asc__5_ = "dem.asc"
```

```
SingleOutput5__4_ = "C:\Documents and Settings\Bill Quinton\Local Settings\Temp\SingleOutput5"

FlowDir_Fill2__5_ = "C:\Documents and Settings\Bill Quinton\Local Settings\Temp\FlowDir_Fill2"

v70 = "C:\GEOtop_new\validation\With lateral flow\New Folder\70"


' Process: Single Output Map Algebra...

gp.SingleOutputMapAlgebra_sa "setnull (thawedN0014.asc==0,thawedN0014.asc)", outputN0014, "'C:\GEOtop_new\validation\With lateral
flow\table\thawedN0014.asc'"


' Process: Single Output Map Algebra (2)...

gp.SingleOutputMapAlgebra_sa "dem.asc - (outputN0014 / 1000)", SingleOutput5, "dem.asc;'C:\Documents and Settings\Bill Quinton\Local
Settings\Temp\outputN0014'"


' Process: Fill...

gp.Fill_sa SingleOutput5, Output_surface_raster, ""


' Process: Flow Direction...

gp.FlowDirection_sa Output_surface_raster, FlowDir_Fill2, "NORMAL", v14


' Process: Flow Accumulation...

gp.FlowAccumulation_sa FlowDir_Fill2, n14, "", "FLOAT"


' Process: Single Output Map Algebra (3)...

gp.SingleOutputMapAlgebra_sa "setnull (thawedN0028.asc==0,thawedN0028.asc)", outputN0028, "'C:\GEOtop_new\validation\With lateral
flow\table\thawedN0028.asc'"


' Process: Single Output Map Algebra (4)...

gp.SingleOutputMapAlgebra_sa "dem.asc - (outputN0028 / 1000)", SingleOutput5__2_, "dem.asc;'C:\Documents and Settings\Bill
Quinton\Local Settings\Temp\outputN0028'"


' Process: Fill (2)...

gp.Fill_sa SingleOutput5__2_, Output_surface_raster__2_, ""
```

```
' Process: Flow Direction (2)...

gp.FlowDirection_sa Output_surface_raster__2_, FlowDir_Fill2__2_, "NORMAL", v28


' Process: Flow Accumulation (2)...

gp.FlowAccumulation_sa FlowDir_Fill2__2_, n28, "", "FLOAT"


' Process: Single Output Map Algebra (5)...

gp.SingleOutputMapAlgebra_sa "setnull (thawedN0042.asc==0,thawedN0042.asc)", outputN0042, "'C:\GEOtop_new\validation\With lateral
flow\table\thawedN0042.asc'"


' Process: Single Output Map Algebra (6)...

gp.SingleOutputMapAlgebra_sa "dem.asc - (outputN0042 / 1000)", SingleOutput5__6_, "dem.asc;'C:\Documents and Settings\Bill
Quinton\Local Settings\Temp\outputN0042'"


' Process: Fill (3)...

gp.Fill_sa SingleOutput5__6_, Output_surface_raster__3_, ""


' Process: Flow Direction (3)...

gp.FlowDirection_sa Output_surface_raster__3_, FlowDir_Fill2__3_, "NORMAL", v42


' Process: Flow Accumulation (3)...

gp.FlowAccumulation_sa FlowDir_Fill2__3_, n42, "", "FLOAT"


' Process: Single Output Map Algebra (7)...

gp.SingleOutputMapAlgebra_sa "setnull (thawedN0056.asc==0,thawedN0056.asc)", outputN0056, "'C:\GEOtop_new\validation\With lateral
flow\table\thawedN0056.asc'"


' Process: Single Output Map Algebra (8)...

gp.SingleOutputMapAlgebra_sa "dem.asc - (outputN0056 / 1000)", SingleOutput5__3_, "dem.asc;'C:\Documents and Settings\Bill
Quinton\Local Settings\Temp\outputN0056'"


' Process: Fill (4)...
```

```
gp.Fill_sa SingleOutput5__3_, Output_surface_raster__4_, ""


' Process: Flow Direction (4)...

gp.FlowDirection_sa Output_surface_raster__4_, FlowDir_Fill2__4_, "NORMAL", v56


' Process: Flow Accumulation (4)...

gp.FlowAccumulation_sa FlowDir_Fill2__4_, n56, "", "FLOAT"


' Process: Single Output Map Algebra (9)...

gp.SingleOutputMapAlgebra_sa "setnull (thawedN0070.asc==0,thawedN0070.asc)", outputN0070, "'C:\GEOtop_new\validation\With lateral
flow\table\thawedN0070.asc'"


' Process: Single Output Map Algebra (10)...

gp.SingleOutputMapAlgebra_sa "dem.asc - (outputN0070 / 1000)", SingleOutput5__4_, "dem.asc;'C:\Documents and Settings\Bill
Quinton\Local Settings\Temp\outputN0070'"


' Process: Fill (5)...

gp.Fill_sa SingleOutput5__4_, Output_surface_raster__5_, ""


' Process: Flow Direction (5)...

gp.FlowDirection_sa Output_surface_raster__5_, FlowDir_Fill2__5_, "NORMAL", v70


' Process: Flow Accumulation (5)...

gp.FlowAccumulation_sa FlowDir_Fill2__5_, n70, "", "FLOAT"
```

Bibliography

M.B. Abbott, J.C. Bathurst, etc. An Introduction to the European Hydrological System- Systeme Hydrologique Europeen, "SHE", 2: Structure of a physically-based, distributed Modelling system. Journal of Hydrology, 87 (1986) 61-77 61

Matteo Dall'Amico, 2010. Coupled water and heat transfer in permafrost Modelling, Doctoral Thesis in Environmental Engineering at the Faculty of Engineering of the University of Trento, Italy.

Dall'Amico, M, Endrizzi, S, Gruber, S, Rigon, R, 2011. A robust and energy-conserving model of freezing variably-saturated soil. Crysphere Volume: 5 Issue: 2 Pages: 469-484 DOI: 10.5194/tc-5-469-2011

Daniel Bayard, Manfred Stahli, etc, 2005. The influence of seasonally frozen soil on the snowmelt runoff at two alpine sites in southern Switzerland, Journal of Hydrology

Beven, K., 1979. A physically based, variable contributing area model of basin hydrology. Hydrological Sciences-Bulletin-des Sciences Hydrologiques, 24,1, 3/1979

Beven, K., 1997. Distributed Hydrological Modelling: Application of the TOPMODEL Concept. John Wiley, Chichester.

Beven, K., 2001. Rainfall-runoff model: the primer. John Wiley, Chichester.

Burgess MM, Smith SL, 2000. Shallow ground temperatures. Geol. Surv. Can. Bull. 547: 89-103.

Bishop KH, 1991. Episodic increases in stream acidity, catchment flow paths and hydrograph separation. PhD thesis, Cambridge University, Cambridge, 241.

Camill P, Clark JS, 1998. Climate change disequilibrium of boreal permafrost peatlands caused by local processes, Am. Nat., 151: 207-222.

Camill P, 2005. Permafrost thaw accelerates in boreal peatlands during late-20th century climate warming. Climatic Change 68: 135-152.

Sean K. Carey, Ming-ko Woo, A case study of active layer thaw and its controlling factors. Permafrost- seventh international conference, Yellowknife, collection nordicana No 55, 1998

Carey SK, Woo M-K., 2001. Slope runoff processes and flow generation in a subarctic, subalpine environment. J. of Hydrol. 253: 110–129.

Carey S.K., Quinton W.L., 2005. Evaluating runoff generation during summer using hydrometric, stable isotope and hydrochemical methods in a discontinuous permafrost alpine catchment. Hydrological Processes, 19: 95-114.

Carey S.K. and Quinton, W.L., 2004. Evaluating snowmelt runoff generation in a discontinuous permafrost catchment using stable isotope, hydrochemical and hydrometric data. Nordic Hydrology, 35: 309-324.

Carey SK, Quinton WL, Goeller NT. 2007. Field and laboratory estimates of pore size properties and hydraulic characteristics for subarctic organic soils. Hydrological Processes: 21, 2560-2571.

Chasmer, L., P. Whittington, W.L. Quinton, C. Hopkinson and R. Petrone, 2011. Vegetation Canopy and Radiation Controls on Permafrost Plateau Evolution within the Discontinuous Permafrost Zone, Northwest Territories, Canada. Permafrost and Periglacial Processes.

Cherkauer, K. A., Lettenmaier, D. P., 2003. Simulation of spatial variability in snow and frozen soil. Journal of Geophysical Research

Chris Hopkinson, Masaki Hayashi and Derek Peddle. 2009. Comparing alpine watershed attributes from LiDAR, Photogrammetric, and Contour-based Digital Elevation Models. Hydrol. Process. 23, 451–463

Church M. 1974. Hydrology and permafrost with reference to Northern North America. Permafrost Hydrology, Proc. of the workshop seminar 1974. Canadian National Committee for the International Hydrological Decade: Ottawa; 7–20.

Craig, J. R., Liu, G., Soulis, E. D. 2010. Runoff-infiltration partitioning using an upscaled Green-Ampt solution. Hydrological Process. Volume: 24 Issue: 16 DOI: 10.1002/hyp.7601

Delisle G, 2007. Near-surface permafrost degradation: How severe during the 21st century? Geophys Res. Lett. 34: L09503.

Dingman, S.L, 2002. Physical Hydrology, Prentice-Hall, Inc., Upper Saddle River, New Jersey 07458.

Dornes P.F., Pomeroy J.W., Pietroniro A., Carey S.K., Quinton WL, 2006. The Use of Inductive and Deductive Reasoning to Model Snowmelt from Arctic Mountain Catchments. International Environmental Modelling and Software Society (iEMSs), Burlington, Vermont, USA, 7 p.

Dornes, Pablo F., John W. Pomeroy, Alain Pietroniro, Sean K. Carey, & William L. Quinton, 2008. Influence of Landscape Aggregation in Modelling Snow-Cover Ablation and Snowmelt Runoff in Arctic Mountainous Environments. Hydrological Sciences–Journal–des Sciences Hydrologiques, 53(4).

Eagleson P.S. 1970, Dynamic Hydrology. McGraw-Hill, New York

Hugh M. French, 2007, the third edition. The periglacial environment. Wiley, Chichester, England

Raoul J. Granger, Partitioning of energy during the snow-free season at the Wolf Creek Research Basin, Wolf Creek Research basin, editors J. W. Pomeroy and R. J. Granger, 1999

Granger RJ, Pomeroy, J. W., J. Parviainen. 2002. Boundary-layer intergration approach to advection of sensible heat to a patchy snow cover. Hydrological Processes, 16, 3559– 3569.

Klas Hansson, Jirka Simunek, Masaru Mizoguchi, etc. 2004. Water Flow and Heat Transport in Frozen Soil: Numerical Solution and Freeze–Thaw Applications. Vadose Zone Journal 3:693–704.

Hayashi, M., N. Goeller, W.L. Quinton, and N. Wright, 2007. A simple heat-conduction method for simulating frost table depth in hydrological models. Hydrological Processes: 21, 2610–2622.

Hewlett JD, Hibbert AR. 1967. Factors affecting the response of small watersheds to precipitation in humid regions. In Forest Hydrology, Sopper WE, Lull HW (eds). Permagon: Oxford; 275–290.

Hinzman LD, et al., 1993. Hillslope hydrology in an Arctic setting. Proc., Permafrost, 6th International Conference, Beijing, Vol. 1, 5–9 July.

St. Jacques, JM, Sauchyn DJ, 2009. Increasing winter baseflow and mean annual streamflow from possible permafrost thawing in the Northwest Territories, Canada. Geophys. Res. Lett. 36: L01401.

Jenks, George F, 1967. The Data Model Concept in Statistical Mapping, International Yearbook of Cartography 7: 186–190.

O. Johansen, 1977. Thermal Conductivity of Soils, Cold Regions Research and Engineering Engineering Laboratory, Hanover, New Hampshire.

Johannessen OM, et al., 2004. Arctic climate change: Observed and modelled temperature and sea-ice variability. Tellus Series A: Dynamic Meteorol. Oceanogr. 56: 328-341.

Jorgenson MT, et al., 2001. Permafrost degradation and ecological changes associated with a warming climate in central Alaska, Climatic Change 48: 551-579.

Kneisel C, 2006. Assessment of subsurface lithology in mountain environments using 2D resistivity imaging. Geomorphology 80: 32-44.

Lawrence,D. M., Slater,A. G., 2005. A projection of severe near-surface permafrost degradation during the 21st centry. Geophysical Research Letter, 32, L24401, doi:10.1029/205GL025080

Lehmann, E. L., 1975. Nonparametrics: Statistical Methods Based on Ranks. Springer, New York.

Liu, GX, Craig, JR, Soulis, ED. 2011. Applicability of the Green-Ampt Infiltration Model with Shallow Boundary Conditions. Journal of Hydrologic Engineering, Volume: 16 Issue: 3 Pages: 266-273 DOI: 10.1061/(ASCE)HE.1943-5584.0000308

Marsh, P., J. Pomeroy, S. Pohl, W. Quinton, C. Onclin, M. Russell, N. Neumann, A. Pietroniro, B. Davison, and S. McCartney, 2007. Snow melt processes and runoff at the Arctic treeline: 10 years of MAGS Research. Vol-2: Hydrological Processes, M-K Woo (ed.). Springer, pp 97-123.

Giuseppe Mendicino, Alfonso Senatore, Giandomenico Spezzano.etc. Three-dimensional unsaturated flow Modelling using cellular automata. Water Resour. Res., VOL. 42, 2006

Osterkamp TE et al., 2000. Observations of thermokarst and its impact on boreal forests in Alaska, USA. Arc. Antarc. Alp. Res. 32: 303-315.

Paniconi, C., and M. Putti, 1994: A comparison of Picard and Newton iteration in the numerical simulation of multidimensional variably saturated flow problems. Water Resour. Res., 30, 3357–3374.

Paniconi, C., P. A. Troch, E. van Loon, and A. G. J. Hilberts, 2003b: Hillslope-storage Boussinesq model for subsurface flow and variable source areas along complex hillslopes: 2. Intercomparison with a three-dimensional Richards equation model. Water Resour. Res., 39, 1317, doi:10.1029/2002WR001728.

Pinder G. F. and Gray W. G. 1977. Finite element simulation in surface and subsurface hydrology. Academic press, New York

Pomeroy, J. W., B. Toth, R. J. Granger, N. R. Hedstrom, and R. L. H. Essery, 2003: Variation in surface energetics during snowmelt in a subarctic mountain catchment. J. Hydrometeor.,4, 702–719.

Pomeroy, J.W., D.M. Gray, T. Brown, N.R. Hedstrom, W.L. Quinton, R.J. Granger, S. Carey, 2007. The Cold Regions Hydrological Model, a Platform for Basing Process Representation and Model Structure on Physical Evidence. Hydrological Processes: 21, 2650–2667.

Pomeroy J., W.L. Quinton and A. Pietroniro. Theoretical and Practical Approaches of Hydrological Parameterisation and Prediction in Cold Regions. Hydrological Processes (Invited), in review.

Zhihao Qin, Pedro Berliner, Arnon Karnieli. Numerical solution of a complete surface energy balance model for simulation of heat fluxes and surface temperature under bare soil environment. Applied Mathematics and Computation 130 (2002) 171–200.

Quinton, W., M. Hayashi, K. Blais, N.Wright and A. Pietroniro, 2004. The Water Balance Of Wetland Dominated Permafrost Basins. International Association of Hydrological Sciences (IAHS) Red Book Series Special Issue for the U.S. National Science Foundation / Northern Research Basins, Workshop on Circumpolar Water Balance, Victoria, B.C., Canada, 15 19 March, 2004, pp. 186-194.

Quinton W.L., Carey S.K. and Goeller N.T., 2004. Snowmelt runoff from northern alpine tundra hillslopes: major processes and methods of simulation. Hydrology and Earth System Sciences, 8: 877-890.

Quinton, W.L., T. Shirazi, S. K. Carey and J. W. Pomeroy, 2005. Soil Water Storage and Active-layer Development in a Sub-alpine Tundra Hillslope, Southern Yukon Territory, Canada. Permafrost and Periglac. Process. 16: 369–382.

Quinton, W.L. and J.W. Pomeroy, 2006. Transformations of Runoff Chemistry in The Arctic Tundra, Northwest Territories, Canada. Hydrological Processes, 20, 2901-2919.

Quinton, W.L. and M. Hayashi, 2007. Recent Advances Toward Physically-based Runoff Modelling of the Wetland-dominated, Central Mackenzie River Basin. Cold Region Atmospheric and Hydrologic Studies. The Mackenzie GEWEX Experience,Vol-2: Hydrological Processes, M-K Woo (ed.). Springer, pp 257-279.

Quinton, W.L. and S. K. Carey, 2008. Towards an Energy-based Runoff Generation Theory for Tundra Landscapes. Hydrological Processes (Invited), 22, 4649–4653.

Quinton, W.L., M. Hayashi and S.K. Carey, 2008. Peat Hydraulic Conductivity in Cold Regions and its Relation to Pore Size and Geometry, Hydrological Processes, 22, 2829–2837.

Quinton, W.L., R. Bemrose, S.K. Carey and Yinsuo Zhang, 2009. The influence of spatial variability in snowmelt and active layer thaw on hillslope drainage for an Alpine tundra hillslope. Hydrological Processes, DOI: 10.1002/hyp.7327.

Quinton, W.L., M. Hayashi and L. Chasmer, 2009. Peatland Hydrology of Discontinuous Permafrost in the Northwest Territories: Overview and Synthesis. Canadian Water Resources Journal, 34, 4.

Quinton, W.L., T. Elliot, J.S. Price, F. Rezanezhad and R. Heck, 2009. Measuring Physical and Hydraulic Properties of Peat from X-ray Tomography. Geoderma: 153, 269–277, doi:10.1016/ j.geoderma.2009.08.010.

Rezanezhad, F, W. L. Quinton, J. Price, D. Elrick, 2009. Examining the effect of pore size distribution and shape on flow through unsaturated peat using computed tomography. Hydrology and Earth System Science.

Richard Ibbitt, Ross Woods. 2004. Re-scaling the topographic index to improve the representation of physical processes in catchment models. Journal of Hydrology 293 (2004) 205–218

Rigon R., et al., 2006. A Distributed Hydrological Model with Coupled Water and Energy Budgets. J. of Hydromet. 7: 371-388.

Robinson SD, Moore TR, 2000. The influence of permafrost and fire upon carbon accumulation in High Boreal peatlands, Northwest Territories, Canada. Arc. Antarc. Alp. Res. 32: 155-166.

Maurice-K. Seguin, et al., 1998. Hydrogeophysical Investigation of the Wolf Creek Watershed, Yukon Territory, Canada. Proceedings from the Wolf Creek Research Basin: Hydrology, Ecology, Environment workshop, Whitehorse, Yukon, March 1998, 55-78.

Serreze MC, et al., 2000. Observational evidence of recent change in the northern high-latitude environment. Climatic Change 46: 159-207.

Shirazi, T., D.M. Allen, W.L. Quinton, J.W. Pomeroy, 2008. Estimating Soil Thaw Energy in Sub-Alpine Tundra at the Hillslope Scale, Wolf Creek, Yukon Territory, Canada. Hydrology Research, 40:1, doi: 10.2166/nh.2009.043.

Singh, P. R., T. Y. Gan,A. K. Gobena. Evaluating a hierarchy of snowmelt models at a watershed in the Canadian Prairies. Journal of Geophysical Research, vol. 114, D04109, doi:10.1029/2008JD010597

Slaughter CW, Kane DL. 1979. Hydrologic role of shallow organic soils in cold climates. Proc., Canadian Hydrology Symp. Cold Climate Hydrology. National Research Council, Ottawa; 380-389.

Smirnova TG, Brown JM, Benjamin SG. 1997. Performance of Different Soil Model Configurations in Simulating Ground Surface Temperature and Surface Fluxes. Monthly Weather Review, Volume 125: 1870-1884.

Smith MW, Riseborough DW, 2002. Climate and the limits of permafrost: A zonal analysis. Permafrost Periglacial Proc. 13: 1-15.

Smith SL, et al., 2008. Ground temperature and thaw settlement in frozen peatlands along the Normal Wells Pipeline corridor, NWT Canada: 22 years of monitoring, 9th International Conference on Permafrost, Fairbanks, Alaska, pp. 1665-1670.

Soulis, E. D., Snelgrove KR, Kouwen N, and Seglenieks F, 2000, Towards closing the vertical water balance in Canadian atmospheric models: coupling of the land surface scheme CLASS with the distributed hydrological model WATFLOOD, Atmosphere Ocean, 38(1): 251-269

Spence C, Woo M-K. 2002. Hydrology of subarctic Canadian Shield: bedrock upland. J. of Hydrol. 262: 111–127.

Tomasz Kozlowski. A semi-empirical model for phase composition of water in clay–water systems. Cold Regions Science and Technology 49 (2007) 226–236

Tromp-van Meerveld HJ, McDonnell JJ. 2006. Threshold relations in subsurface stormflow 2. The fill and spill hypothesis. Water Resour. Res. 42: W02411.

Tyson E. Ochsner, John M. BakerIn. Situ Monitoring of Soil Thermal Properties and Heat Flux during Freezing and Thawing. SSSAJ: Volume 72: Number 4 • July–August 2008

Weiler M, McDonnell J. 2004. Virtual experiments: a new approach for improving process conceptualization in hillslope hydrology. J of Hydrol. 285: 3–18.

Peter Williams, 1989. The frozen earth: fundamentals of geocryology. Cambridge university press, Cambridge, England

Waddington, J.M., W. Quinton, J.S. Price, P. Lafleur, 2008. Advances in Canadian Wetland Hydrology, 2003-2007. Canadian Water Resources Journal: 34, 139-148.

David M. Wolock. Gregory J. McCabe Jr. 1995. Comparison of single and multiple flow direction algorithms for computing topographic parameters in TOPMODEL. Water Resources Research. 31, 5, 1315-1324.

Woo M-K. 1986. Permafrost hydrology in North America. Atmosphere-Ocean 24(3): 201–234.

Woo, M. K., and P. Marsh 2005: Snow, frozen soils and permafrost hydrology in Canada, 1999-2002. Hydrological Processes, 19, 215– 229.

Wright, N., W.L. Quinton and M. Hayashi, 2008. Hillslope runoff from ice-cored peat plateaus in a discontinuous permafrost basin, Northwest Territories, Canada. Hydrological processes, 22, 2816–2828.

Wright, N., M. Hayashi, and W. L. Quinton, 2009. Spatial and temporal variations in active layer thawing and their implication on runoff generation in peat-covered permafrost terrain, Water Resources Res., 45, W05414, doi:10.1029/2008WR006880.

ED Yershov, interpreted by Peter J. Williams, 1998. General geocryology, Cambridge university press, Cambridge, England

Zhang Y, et al., 2003. A process-based model for quantifying the impact of climate change on permafrost thermal regimes, J. Geophys. Res. 108, 4695.

Zhang Y, et al., 2008. Disequilibrium response of permafrost thaw to climate warming in Canada over 1850-2100. Geophys. Res. Lett. 35: L02502.

Zhang, Yinsuo, Sean K. Carey and William L. Quinton, 2008. Evaluation of the simulation algorithms and parameterization methods for ground thawing and freezing in permafrost regions. Journal of Geophysical Research, 113, D17116, doi: 10.1029/2007JD009343.

Zhang Yinsuo, S.K. Carey, W. L. Quinton, J. R. Janowicz and G. N. Flerchinger, 2010. Comparison of algorithms and parameterisations for infiltration into organic-covered permafrost soils. Hydrology and Earth System Sciences.